Dissertation
submitted to the
Combined Faculties for the Natural Sciences and for Mathematics
of the Ruperto-Carola University of Heidelberg, Germany
for the degree of
Doctor of Natural Sciences

Put forward by

Diplom-Physiker Martin Anthony Niklas

Born in: Amberg, Germany

Oral examination: February 6$^{\text{th}}$, 2014

Cell-fluorescent ion track hybrid detector: A novel hybrid technology for direct correlation of single ion tracks and subcellular damage sites in clinical ion beam

Referees: Prof. Dr. Wolfgang Schlegel

Prof. Dr. Oliver Jäkel

Erklärung

Ich erkläre hiermit, dass ich die vorgelegte Dissertation selbst verfasst und mich dabei keiner anderen, als der von mir ausdrücklich bezeichneten Quellen und Hilfen bedient habe.

Heidelberg, den 07.01.2014

Martin Anthony Niklas

Zusammenfassung

Teilchentherapie erzielt klinische Erfolge. Ihre grundlegenden biologischen Wirkmechanismen sind aber nicht vollständig bekannt. Dies liegt vor allem an der Schwierigkeit, physikalische Strahlungsparameter und biologische Mechanismen auf subzellulärer Ebene zu verknüpfen. Ziel dieses Projektes war daher die Entwicklung einer Hybrid-Detektortechnologie (Cell-Fit-HD), welche genau diese Korrelation ermöglicht. Cell-Fit-HD basiert auf einem fluoreszierenden Kernspurdetektor (FNTD). Dieser wird mittels herkömmlicher Konfokalmikroskopie (CLSM) ausgelesen. Um den Hybrid zu erstellen, wurde der FNTD mit Zellen beschichtet. Es wurden verschiedene fluoreszierende Biomarker in der Zellschicht getestet. So wurde ein Verfahren entwickelt um beide Komponenten des Hybrid-Detektors in einem Schritt mittels CLSM auszulesen. Individuelle von Cell-Fit-HD detektiere Ionendurchgänge wurden in der Zellschicht rekonstruiert. Diese wurden sowohl mit DNA Doppelstrangbruchsequenzen in den Zellkernen als auch mit dem Zellüberleben örtlich korreliert. Die Hybrid-Detektortechnologie erlaubt erstmals eine örtliche und hochaufgelöste Korrelation zwischen Ionentreffer und Zellreaktion auf subzellulärer Ebene sowie des Zellüberlebens unter therapeutischen Bedingungen. Ionenspezifische mikroskopische Parameter können extrahiert und mit der Antwort jeder einzelnen Zelle verknüpft werden. Die einzigartige örtliche Auflösung von Cell-Fit-HD könnte es ermöglichen, für die grundlegenden biologischen Wirkmechanismen ionisierender Strahlung Antworten zu finden.

Abstract

Despite a rapid development in ion beam cancer therapy there is still a great lack in understanding the fundamental mechanisms linking physical energy deposition and biological response on the subcellular scale. A cell-fluorescent ion track hybrid detector (Cell-Fit-HD) was thus developed for direct correlation of single ion tracks and subcellular damage sites in clinical ion beams. It is based on the fluorescent nuclear track detector (FNTD) read out by confocal laser scanning microscope (CLSM). The FNTD was coated with various cell lines to create the actual hybrid composite. Different cell compartment specific fluorescent stains were tested on the Cell-Fit-HD. A protocol was developed to read out the hybrid in-situ by a single CLSM. Single ion tracks detected were reconstructed in the biological compartment and correlated to radiation-induced DNA double strand break sequences as well as to cell survival kinetics. Cell-Fit-HD enables the investigation of radiation-related cellular events along single ion tracks on the subcellular scale. Microscopic physical parameters of each incident ion can be extracted and correlated to the cellular damage response pattern. The unique spatial resolution of Cell-Fit-HD could help to gain a deeper understanding between particle hits and resulting biological effects beyond the statistical relations we know today.

Contents

1 Introduction

Worldwide the number of ion beam cancer therapy (IBCT) centers is increasing. By the end of 2012, 88,448 patients have been treated in seven carbon ion and 37 operating proton beam therapy facilities [1]. Additional 37 therapy centers are planned to start operation within the next five years [2]. Heidelberg Ion Beam Therapy Center (HIT) alone has a planned treatment capacity of over 1300 patients yearly [3]. Despite this rapid clinical development, there is still a great lack in understanding the fundamental mechanisms linking physical energy deposition to the biological response on the microscopic scale (Figure 1.0.1A).

The BIOSTACK experiment undertaken during the Apollo lunar missions was one of the first approaches to treat biological response to radiation on a multi-scale approach [4, 5]. It comprised a hybrid detector (i.e. combination of a biological sample and physical detector unit) visualizing single tracks of cosmic radiation and their correlated effects on biological matter (e.g. seeds). Despite high accuracy in localizing the ion penetration point in the biological sample, space-flight conditions imposed experimental constraints.

In this thesis the idea of the BIOSTACK experiment is followed again to develop a novel generation of hybrid detectors. The central compartment is the recently introduced fluorescent nuclear track detector (FNTD) [6]. The passive detector is read out non-destructively by a confocal laser scanning microscope (CLSM). It provides almost 100% detection efficiency of tracks by incident ions of a great spectrum of particle types and energies [7].

Here, the FNTD is coated with a cell layer to develop the *cell-fluorescent ion track hybrid detector* (Cell-Fit-HD). In this hybrid the FNTD (the physical compartment) and the cell layer (the biological compartment) are read-out in situ by the very same CLSM. The combination of single ion track visualization in the physical and radiation damage imaging in the biological compartment promises direct visualization and spatial correlation of physical energy deposition and subcellular response in clinical ion beams (Fig. 1.0.1B).

In this thesis, protocols were developed to engineer the hybrid and to enable a sequential read-out of the physical and biological compartment (section 4.1). Ion track reconstruction in 3D was performed using the depth information gained by the sole FNTD read-out (section 4.2). The ability of 3D spatial correlation between physical

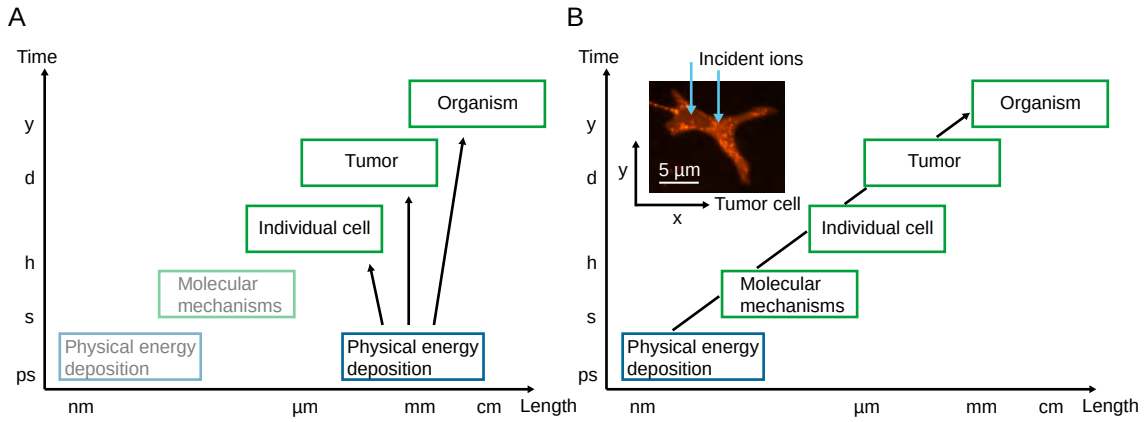

Figure 1.0.1: Biological response to ion irradiation on a multi-scale (schematic scales). (A) Current status: standard in vitro cell colony experiments can measure cell survival after dose deposition. The corresponding ion beam (physical energy deposition) can be visualized on macroscopic length scales. Animal experiments allow to correlate the energy deposition to the whole tumor entity. A measure of the 5-year survival investigates the success of ion beam cancer therapy (IBCT) to the whole organism. (B) Objective of the hybrid detector Cell-Fit-HD: A read-out with a resolution principally limited by optical microscopy allows to resolve the physical energy deposition by single ions on the sub-μm scale. Co-detection and correlation to its cellular damage site (Insert) opens the possibility to link the microscopic ion beam parameters not only to the molecular mechanisms (on the microscopic scale) but also to the fate of the tumor (and organism, macroscopic scale).

energy deposition and subcelluar damage by the Cell-Fit-HD was proven (section 4.3). It was investigated in parallel whether it is principally possible to resolve the particle spectrum using the FNTD as a radiation monitoring device (section 4.4). Single cell fate after therapeutic carbon ion irradiation was correlated to microscopic beam parameters utilizing the Cell-Fit-HD (section 4.5).
Most of the results have already been published [8, 9, 10, 11]. Reference to the corresponding publications enclosed in the appendix (B-E) is made.

2 Fundamentals

2.1 Rationale behind IBCT

The possibility of concentrating the physical radiation dose, i.e. deposited energy (Eq. 2.3) in a well-defined target volume while sparing surrounding healthy tissue makes IBCT a promising treatment modality for deep-seated tumors and tumors near organs at risk [12]. The reason behind is a sharp increase of energy deposition, the so-called Bragg peak, by slowed down particles with increasing penetration depth and a rapid dose fall-off beyond (Fig. 2.1.1). The ability for this improved (compared to conventional photon therapy) dose conformation and a high ratio of the Bragg peak dose versus the dose in the entrance channel allows for high-precision radiotherapy [3]. The ability to increase the delivered dose in the tumor rises the probability to control the tumor growth and hence potentially increases the survival of the patient [12]. Simultaneously, the irradiation volume of surrounding healthy tissue is decreased leading to a higher radiation tolerance. The probability of severe side effects is thus lowered.
The precise energy deposition in the target volume is technically realized by means of modern beam delivery systems like active beam scanning [13]. There, the 3D irradiation volume is dissected into a raster of voxels (small volume elements) prior to irradiation. A fine particle beam (so-called pencil beam) is used to deliver the desired dose to the corresponding voxel.
The potential benefit of ions heavier than protons compared to photon irradiation is expressed by a single parameter, the relative biological effectiveness (RBE) [13]. It is defined as the quotient of a particle dose (D_{ion}) and a reference photon dose (D_{ref}, typically x rays or γ rays) of equivalent biological effect:

$$\mathrm{RBE} = \frac{D_{\mathrm{ref}}}{D_{\mathrm{ion}}}\Big|_{\mathrm{isoeffect}} \tag{2.1}$$

Despite being a single parameter, the RBE is a complex quantity, depending on physical and biological parameters such as particle type and energy, radiation dose as well as type of tissue and the biological end point to be considered (Fig. 2.1.2) [13]. The RBE can therefore vary drastically within the irradiated volume. Protons have a similar biological effect as photons with RBE= 1.1 [14]. The product of the RBE with D_{ion} (Eq. 2.1) is called biological effective (short biological) dose.

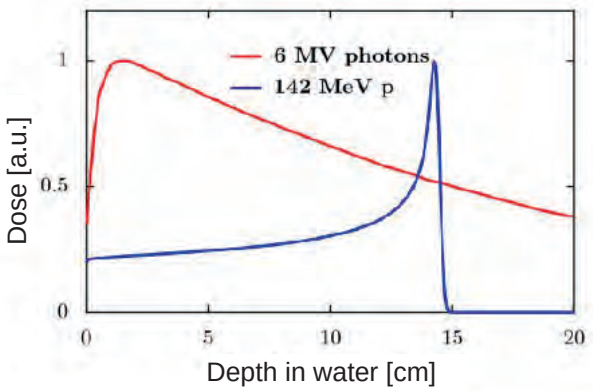

Figure 2.1.1: Inverse depth-dose profile of ions. Compared to megavolt photons, ions are able to precisely deposit most of their energy in a small volume (Bragg peak). By adjusting the kinetic energy of the particles the position of this peak in depth can be changed precisely. For therapeutic treatment a spread-out Bragg peak (SOBP), a superposition of a set of beams with decreasing energies, is used to cover the distal tumor extension. Taken from [15].

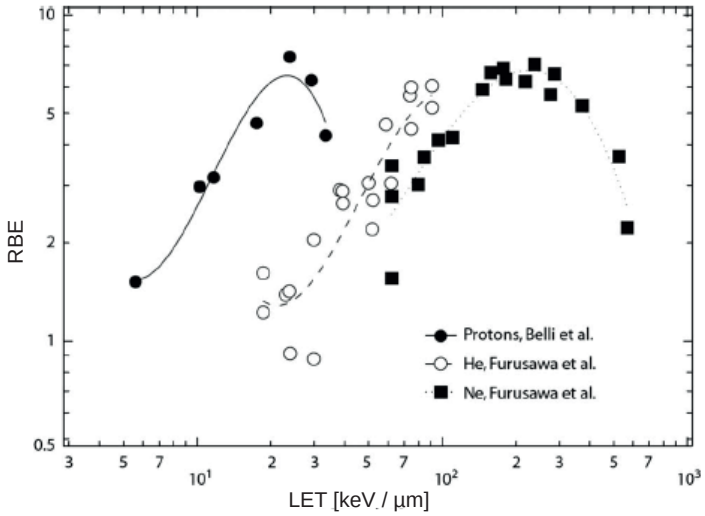

Figure 2.1.2: RBE dependency on the linear energy transfer (LET) for several ion types. The LET is closely related to the energy of the ion (Eq. 2.6). The RBE is increasing with increasing LET and hence decreasing kinetic energy of the incident ion of a certain ion type. After an ion type-specific maximum the RBE decreases. The RBE values were gained from cell survival experiments with V79 hamster cells [16, 17]. Taken from [18].

2.2 Interactions of ions with matter

Multiple inelastic collisions of the incident particles with the target electrons (Coulomb interaction) causing excitation and ionization of the target atoms dominate the energy loss [13, 19]. Despite a much smaller probability, projectile and target fragmentation by nuclear interactions is significantly contributing to the particle spectrum with increasing penetration depth [13]. Projectile fragmentation processes leading to a buildup of lower-Z fragments (for carbon ions: proton, helium, lithium, beryllium, boron) causes attenuation of the original number of primary particles. Unlike target fragments produced by recoil, having a relatively low energy and therefore a short range, projectile fragments largely contribute to the particle spectrum impinging the tumor. The fragments exhibit a much broader angular distribution (mainly determined by reaction kinematics) than the lateral spread of the primary particles caused by multiple Coulomb scattering.
Energy loss by elastic scattering with the target nuclei is very small compared to ionization. Yet it dominates the stopping process at the very end of the particle path, but plays a negligible role in IBCT [20]. Energy loss by emission of bremsstrahlung, being proportional to the inverse square of the projectile mass, is also negligible for proton and heavier ions.
The energy loss of the particle is of stochastic nature and causes it to continuously slow down. The mean energy loss $\mathrm{d}E$ per unit path length $\mathrm{d}l$ by inelastic collisions with the target electrons is called (electronic) stopping power S. It is described by the Bethe-Bloch formula in first order:

$$S = -\frac{\mathrm{d}E}{\mathrm{d}l} \propto \rho \frac{Z}{A} \frac{z^2}{\beta^2} \left[\ln \frac{2 m_e c^2 \beta^2}{I(1-\beta^2)} - \beta^2 \right] \tag{2.2}$$

with $[S] = \mathrm{keV}\,\mu\mathrm{m}^{-1}$ [21, 22]. It depends on the projectile (charge z, ratio $\beta = v/c$ with v being the velocity) and on the target material (mass density ρ, atomic number Z, atomic weight A, mean excitation potential of the target atom I). The mean excitation potential I can be calculated by $I = 12\,\mathrm{eV} \cdot Z + 7\,\mathrm{eV}$ for $Z < 13$ [19]. The quantity $m_e c^2$ is the electron rest energy.

2.3 Important physical quantities

The absorbed dose D is the quotient of the mean energy $\mathrm{d}\bar{\epsilon}$ imparted by ionizing radiation to the matter in a volume element of mass $\mathrm{d}m$:

$$D = \mathrm{d}\bar{\epsilon}/\mathrm{d}m \tag{2.3}$$

with $[D] = \mathrm{J\,kg^{-1}} = \mathrm{Gy}$ [23]. For a parallel particle beam of particle fluence Φ and stopping power S, D can also be calculated in a material of mass density ρ by [13]:

$$D\,[\,\mathrm{Gy}] = 1.6 \cdot 10^{-9} \cdot S\left[\mathrm{keV\,\mu m^{-1}}\right] \cdot \Phi\left[\,\mathrm{cm^{-2}}\right] \cdot \rho^{-1}\left[\mathrm{cm^3\,g^{-1}}\right]. \tag{2.4}$$

The fluence Φ is defined as the quotient of the number of particles $\mathrm{d}N$ incident on a sphere of cross-sectional area $\mathrm{d}a$:

$$\Phi = \mathrm{d}N/\mathrm{d}a \tag{2.5}$$

with $[\Phi] = \mathrm{m^{-2}}$ [23]. In this text, the term absorbed dose is abbreviated by dose.
The stopping power S is closely related to the linear energy transfer (LET). The LET (also termed restricted linear electronic stopping power) of a material for charged particles is defined as:

$$\mathrm{LET}_\Delta = \left(\frac{\mathrm{d}E}{\mathrm{d}l}\right)_\Delta. \tag{2.6}$$

The quantity $\mathrm{d}E$ "is the energy lost by a charged particle due to electronic collisions in traversing a distance $\mathrm{d}l$, minus the sum of the kinetic energies of all the electrons released with kinetic energies in excess of Δ" [23]. The unit is $\mathrm{J\,m^{-1}}$ or $\mathrm{keV\,\mu m^{-1}}$. In the unrestricted linear energy transfer (LET_∞) all possible energy losses are included (i.e. $\Delta = \infty$), also the energy loss leading to a kinetic energy of the released electrons beyond the cut-off Δ. The quantity LET_Δ also includes the binding energy for all collisions, i.e. the energy loss which does not reappear as kinetic energy of the released electrons.
From a geometrical point of view the average range of the secondary electrons released by inelastic collisions of the primary particles with the atomic electrons is given by the energy $\mathrm{d}E$ transferred in such processes. The cut-off energy Δ is related to a cut-off range of these electrons defined by the corresponding electron-range model [24]. The quantity LET_Δ can therefore be considered as the mean energy lost per unit path length within a rotation-symmetrical volume of limited radius (given by Δ) along the ion track. In the case of LET_∞ there is no restriction in the volume, i.e. all secondary electrons emerging from the ion track are considered. Neglecting excitation of the target atoms the unrestricted LET therefore equals the absolute value of the stopping power S.
The absorbed dose and LET are non-stochastic quantities stating expectation values. However, energy is deposited stochastically in discrete packages by the interaction of the primary particles with matter. These packages are non-uniformly distributed throughout the irradiated volume. To account for the stochastic nature of energy deposition on the microscopic (sub-μm to μm) scale, the concept of microdosimetry was introduced [25]. There, the microdosimetry quantities to absorbed dose and LET,

specific energy z and lineal energy l are defined for single events.

2.4 Microscopic track structure

The superior biological effect of IBCT relies on the localized energy deposition of the penetrating particles. Unlike photon irradiation, densely ionizing processes along the ion trajectory occur (Fig. 2.4.1A,B). The first generation of secondary electrons released by inelastic collisions of the incident ion with the target atoms triggers a chain of further electron release. The secondary electrons can undergo further ionization events until their kinetic energy drops below a threshold when ionization is no longer possible. Then, excitation dominates leading to further energy deposition in the target volume.

The emission angle and kinetic energy of the released electrons is principally determined by the double-differential cross section. The mean kinetic energy of the released first generation of secondary electrons in water is in the order of 100 eV [26]. Due to this relatively small energy and preferred scattering in forward direction, the energy deposition by the secondary electrons is highly concentrated in a small volume along the ion track called track core. Additional δ electrons, i.e. secondary electrons having enough energy (up to several keV) to leave the track core, occur. Due to frequent scattering processes their trajectories exhibit a broad angular distribution.

Because of a much higher energy loss per unit path length for heavy ions, i.e. $S \propto Z^2/\beta^2$ (Eq. 2.2) their kinetic energies have to be much higher in order to gain the same penetration depth as lighter ions. This in turn means that more secondary electrons are liberated in ionizing processes. Thus, the diameter of the track core is slightly increasing while the total energy deposition (i.e. the absorbed dose) in the material increases strongly.

A summation over all stochastic energy deposition events by the secondary electrons along the ion track yields the track structure models by e.g. Butts and Katz [27] and Scholz (termed Scholz model in this text) [28]. The corresponding radial dose distribution (RDD) shows a steep gradient, following an $1/r^2$ dependence, and thus reflect the localized energy deposition in the close vicinity of the ion track center (Fig. 2.4.1C). The maximum range of the δ electrons determines the range cut-off in the RDD. Due to a lack of experiments, the actual dose distribution at the very center of the ion track (e.g. a plateau in the Scholz model) still remains unclear.

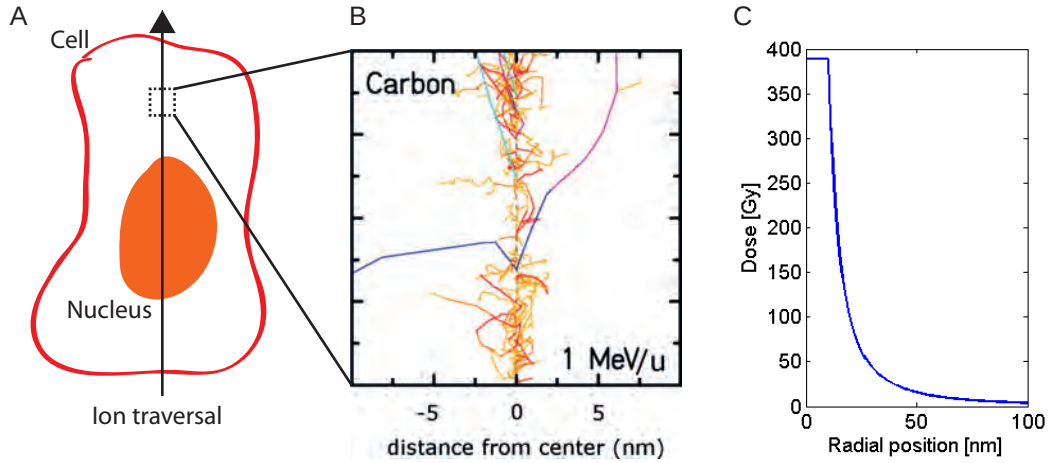

Figure 2.4.1: Spatial energy deposition of ions. (A) Schematic illustration of an ion traversing a cell. (B) Simulation of microscopic tracks of secondary electrons produced by a carbon ion, 1 MeV u^{-1}. Each line corresponds to the track of a secondary electron. Taken from [29]. (C) Radial dose distribution according to the Scholz model for carbon ions (152.05 MeV u^{-1}) with a plateau of diameter 10 nm and a steep ($1/r^2$) gradient. Computed using libamtrack [24].

2.5 Optical microscopy

2.5.1 Confocal microscopy

Confocal microscopes use of a pinhole aperture in front of a sensitive detector [30]. It allows for optical sectioning of the specimen. The pinhole acts hereby as a filter to eliminate out-of-focus light in samples whose thickness exceed the immediate focal plane. By optical sectioning, axial resolution enhancement is achieved. The acquisition of a stack of imaging planes at well defined depths allows for a retrospective 3D reconstruction of the specimen. A mean beam splitter (MBS, a dichroic mirror) reflects excitation light onto the specimen and enables only emission light of lower frequency than the excitation light (Stokes Shift) to transmit and to reach the sensitive detector. To get a point-like illumination an additional pinhole is placed after the excitation source. Excitation and emission pinholes are situated in conjugate planes.
The detected image of a point-like object in the confocal arrangement is described by the point-spread-function (PSF) h_{conf} (Fig. 2.5.1A,B) [31, 32]. It is a convolution of the light intensity distribution emerging from the point-like illumination process onto the specimen (h_{ill}) with the corresponding distribution emerging from the point-like detection (h_{det}):

$$h_{\mathrm{conf}} = h_{\mathrm{ill}} \otimes h_{\mathrm{det}}. \tag{2.7}$$

In ideal microscopes, h_{conf} is symmetrical with respect to the focal plane. The three dimensional spatial distribution of h_{conf} defines the spatial resolution of the microscope. The lateral resolution Δx can be defined by the lateral full width half maximum

(FWHM) Δd of the main maximum, called focal spot [33, 34]:

$$\Delta x := \Delta d \approx \lambda/(2n \sin \alpha) = \lambda/(2\mathrm{NA}). \tag{2.8}$$

Along the optical axis, the corresponding FWHM Δz and hence the axial resolution is related to:

$$\Delta z \approx \lambda/(2n \sin^2 \alpha). \tag{2.9}$$

Here, λ and n are the excitation wavelength and refractive index, respectively. The aperture angle α defines the half-angle of the maximum cone of light that can enter or exit the objective lens. The numerical aperture (NA) thus expresses the ability of a microscope objective to gather light.

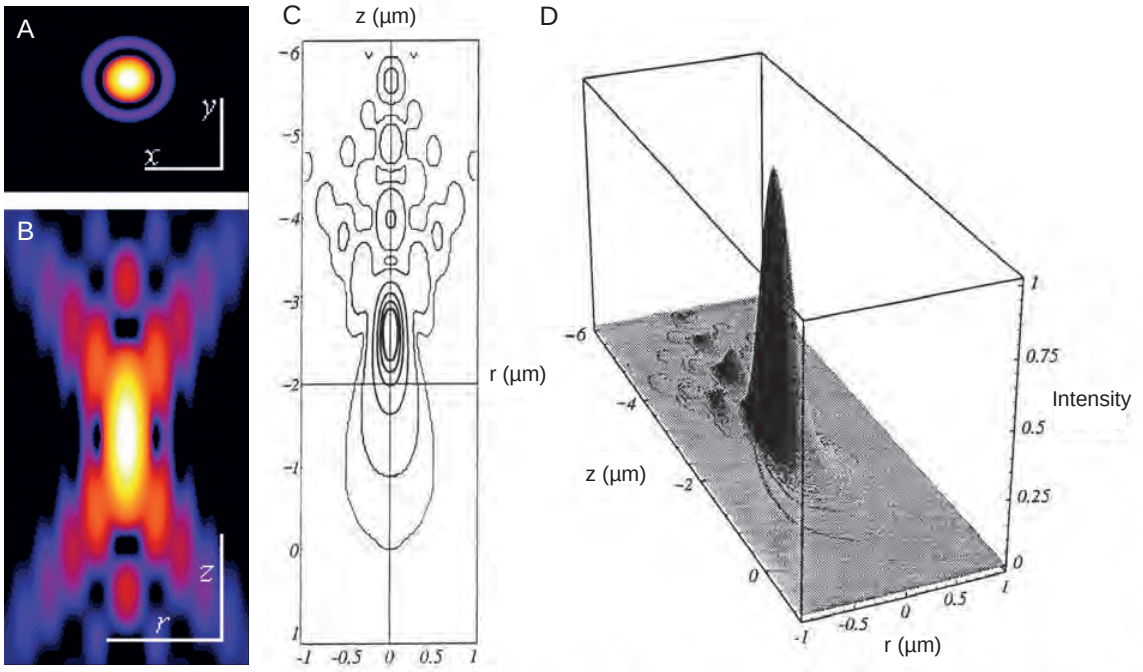

Figure 2.5.1: Point spread function (PSF) in confocal microscopy. Lateral (A) and (B) axial sectioning of an exemplary symmetrical PSF h_{conf} in the absence of aberrations. Contour plot of an axial sectioning (C) and the corresponding intensity profile (D) of h_{conf} in the presence of spherical aberrations. The originally symmetrical PSF gets distorted mainly along the z direction. Remote local maxima get strengthened. An axial shift of the focal spot center from its original position (z=0 μm) occur. (A) and (B) are adapted from [35], (C) and (D) are adapted from [31].

2.5.2 STED microscopy

Stimulated emission depletion (STED) microscopy uses the concept of switching off a fluorophore from its excited (fluorescent) state S_1 to its ground state S_0 (Fig. 2.5.2) [34, 36]. An excitation beam transferring the fluorophores into S_1 is superimposed by a depletion (so-called STED) laser beam. It quenches S_1 to S_0 by stimulated emission.

High STED pulse intensity I is needed to confine the fluorophores in S_0 and to gain saturated reduction of the fluorescence. To ensure a high probability ($> 99\%$) for switching off the fluorophore, $I > 5I_s$ is used. The saturation intensity I_s is defined as the intensity at which the probability to find the fluorophore in S_1 is reduced by half. The spatial intensity profile $I(x,t)$ of the STED laser is usually doughnut-shaped with a central zero. At this zero and close to it, fluorophores are not quenched by the STED laser. The FWHM Δd of the remaining volume where fluorescence can take place depends on the intensity of the STED laser. With increasing intensity it can be narrowed down, close to the point of zero intensity. Thus Δd and hence the lateral resolution Δx do not have a lower limit anymore. The expression for Δx is then an extension of Abbe's equation (Eq. 2.8) and is defined by

$$\Delta x \approx \frac{\lambda}{2n \sin\alpha \sqrt{1 + I/I_s}}. \tag{2.10}$$

As all molecules within Δd contribute to the fluorescence signal, STED microscopy displays the spatial distribution of the fluorophores. The specimen is scanned point-by-point, i.e. by shifting $I(x,t)$ over the sample. Parallel recording is also possible [36]. If a STED microscope is built once it can be also used as a confocal microscope by switching off the STED laser. However unlike confocality it does not rely on a point-like detector pinhole [34].

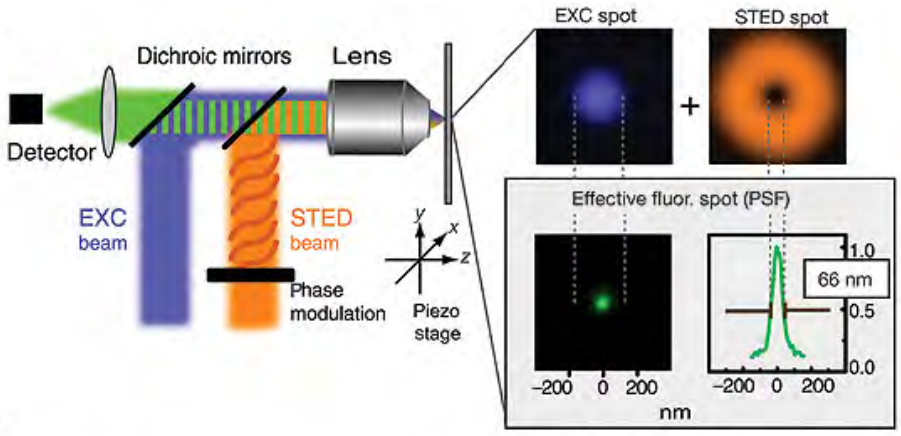

Figure 2.5.2: Working principle of stimulated emission depletion (STED) microscopy. The excitation beam is superimposed by the STED beam. The diameter of the central maximum of the effective PSF is subdiffraction-sized. Adapted from [37].

2.5.3 Spherical aberrations by refractive index mismatch

In optical microscopy, change of refractive index can occur in the light path, e.g. at the transition of the lens immersion medium to the biological specimen. At such dielectric boundaries light is partly reflected and refracted. This causes a shift in phase and

in amplitude of the propagating wave and thus a disturbance of h_{conf} (Fig. 2.5.1C,D) [31, 32]. A loss of intensity as well as axial spreading and an axial shift of the central intensity maximum occur. The detected decrease in image brightness is however a result of the confocal arrangement. By multiplication of the disturbed h_{ill} and h_{det} (Eq. 2.7), the focal region of h_{conf} gets further weakened while more remote parts (e.g. secondary maxima) get strengthened.

The aberrations are increasing with increasing distance of the light rays from the optical axis (therefore spherical aberrations). Apart from the axial shift of the focal position they are less pronounced for low NA (definition in section 2.5.1) objectives due to small aperture angles [32]. Spherical aberrations have big impacts for high NA objectives. With increasing distance to the optical axis the light rays display a greater mismatch of their intersections at the optical axis. The disturbance of h_{conf} is related to the read-out depth (with respect to the interface of refractive index mismatch). The maximum intensity is strongly decreasing with increasing depth. Exemplarily, a noticeable decrease of $> 80\%$ at $40\,\mu$m depth occurs [32].

Geometrical approaches accounting for the spherical aberrations are performed in order to calculate the actual focal position (section 3.14).

3 Materials and Methods

3.1 Materials for cell biology

Important materials for engineering Cell-Fit-HD including commercial staining kits, antibodies and cell lines are listed in the appendix (Tables A1-A6).

3.2 Al_2O_3:C,Mg based FNTD

Fluorescent nuclear track detectors (FNTDs, Fig. 3.2.1A) of dimensions 4 x 8 x 0.5 mm^3 are cut from a Al_2O_3:C,Mg single crystal [6]. Al_2O_3:C,Mg refers to α-Al_2O_3 (equivalent names: corundum, sapphire) grown in a highly reduced atmosphere of oxygen and doped with carbon and magnesium (Mg^{2+}) ions. By doping fluorescent F_2^{2+}(2Mg) color centers are created. They are aggregate defects formed by two oxygen vacancies and two Mg^{2+}-ion impurities.
The F_2^{2+}(2Mg) centers are efficient for radiation field monitoring. For this purpose the FNTD is read out non-destructively by confocal microscopy (Fig. 3.2.1B,C). Pristine F_2^{2+}(2Mg) centers can be excited at 435 nm and emit fluorescent light at 520 nm (Type-1 read, Fig. 3.2.2B). By either sequential two-photon absorption (photochromic transformation) or exposing the detector to ionizing radiation (radiochromic transformation) F_2^{2+}(2Mg) are transformed into stable F_2^{+}(2Mg) centers (Fig. 3.2.2A). The radiation-transformed color centers have different optical properties: they absorb light in the absorption band centered at 620 nm, prompting 750 nm fluorescence with a short lifetime of 75 ± 5 ns (Type-2 read, Fig. 3.2.2B). F_2^{2+}(2Mg) centers are also created during crystal growth to some extent.
FNTDs are sensitive to ions with LET_∞ in water $> 0.5\,keV\,\mu m^{-1}$ [7, 38]. The passive detector has a detection efficiency close to 100% for the entire spectrum of primary particles and fragments of energies found in IBCT [7, 39]. The current limit of maximum accessible track fluence is in the range of $0.5 \cdot 10^8\,cm^{-2}$ corresponding to clinical doses for carbon ion irradiation (i.e. 2.27 Gy in water for C-12, 90 $MeV\,u^{-1}$) [7].
FNTDs have one 4 mm by 8 mm surface polished to optical quality specified by 40/20 scratch/dig, i.e. scratch width of maximum 0.04 mm and a dig diameter of maximum 0.2 mm. The optical *c*-axis of the crystal is aligned parallel to the longer side of the detector indicated by the cut edge (Fig. 3.2.2A). The fluorescence properties of

Al_2O_3:C,Mg are anisotropic [40]. To maximize the fluorescence intensity, the polarization direction of the excitation laser light has to be aligned with the optical *c*-axis of the crystal [39]. The optical stability of the transformed color centers and the heat-resistance (up to 700°C) allows the FNTD to be read out multiple times [41] and to be autoclaved [9].

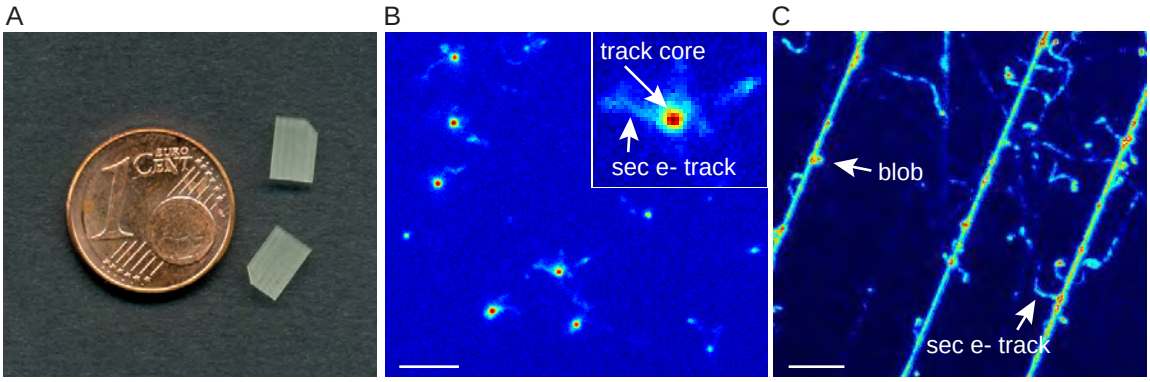

Figure 3.2.1: FNTD and fluorescence read-out signal. (A) Two FNTDs (each 4 x 8 x 0.5 mm^3). By the confocal read-out, FNTDs allow for particle track visualization of sub-μm resolution. Fluorescent images of carbon ions (270.55 MeV u^{-1}) penetrating the FNTD perpendicular (B) and parallel (C) to its surface. The occurring track spots (physical energy deposition events) are the characteristic signatures of the swift ions left in Al_2O_3:C,Mg. The intensity of a track spot depends on the energy deposition of the swift ion. Trajectories by released secondary electrons (sec e-), i.e. small structures around the ion tracks as well as local energy aggregations (blobs) are visible. Insert: magnification of a single track spot. The track core is encoded by dark red. Scale bars, 5 μm. Courtesy of M.S. Akselrod (A) and of F. Lauer (C). Taken from [9].

3.3 LSM 710

For the sequential read-out of the Cell-Fit-HD the inverted confocal laser scanning microscope LSM 710 (Carl Zeiss AG, Germany) was used. It is referred to CLSM in this text. Components important for the sequential read-out are listed in Table 3.3.1. The CLSM features two photomultipliers (PMTs), one transmission photomultiplier (T-PMT) and two avalanche-photodiodes (APD) [43]. The microscope was equipped with a scanning stage (DC 120 x 100), a z-piezo stage, and an incubator system. The CLSM including its control software (ZEN, version 2009) was provided by the DKFZ's light microscopy core facility. The acquired image data was stored with 16 bit color depth in the .lsm format (developed by Carl Zeiss AG).

3.3.1 Sample handling

For the read-out Cell-Fit-HDs were mounted in uncoated glass bottom culture dishes (MatTek Corp, USA, Cat. No. P35G-1.5-20-C) with a dish diameter of 35 mm and coverslip thickness of 0.16 - 0.19 mm. The glass diameter was 20 mm. Zeiss Immersol^{TM}518

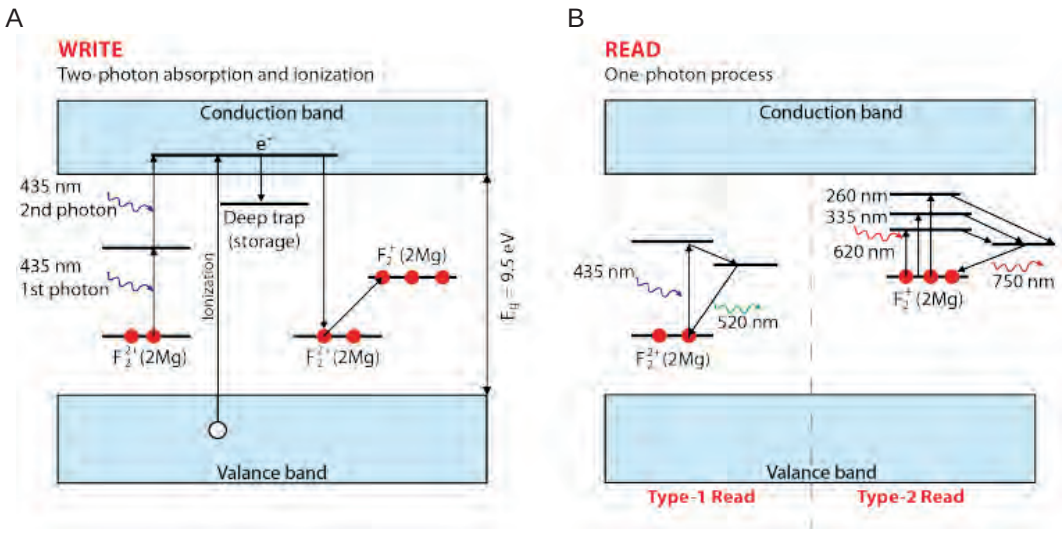

Figure 3.2.2: Band diagram of Al_2O_3:C,Mg. (A) Write: transformation by sequential two-photon absorption (photochromic) or by ionizing radiation (radiochromic) of the pristine $F_2^{2+}(2Mg)$ centers. (B) Fluorescence of the pristine $F_2^{2+}(2Mg)$ (Type-1 read) and of the $F_2^{+}(2Mg)$ (Type-2 read) centers. Alternatively to 620 nm, the $F_2^{+}(2Mg)$ centers also absorb light in the absorption band centered at 260 nm and 335 nm, prompting 750 nm fluorescence. Reproduction according to [41, 42]. Courtesy of T. Rösch.

Table 3.3.1: Important components of the CLSM (LSM 710) used for the read-out of the Cell-Fit-HD.

Components	Specifications
Excitation	
Mercury lamp	
diode laser 405 nm	30 mW nominal power
Ar laser 458/488/514 nm	25 mW nominal power
HeNe laser 633 nm	5 mW nominal power
Objective	
40x	Numerical aperture (NA): 1.40, oil
63x	NA: 1.45, oil
Main dichroic beam splitter (MBS)	
488/561/633 nm	
405 nm	
488 nm	
458/561 nm	
Avalanche-photodiode (APD)	Quantum efficiency (visual band): 40 - 75% Dark count rate: < 250 Hz Dead time: 40 ns Pulse length: 15 ns After-pulse height: 0.5% (100 - 500 ns) Maximum count rate: 20 MHz
z-piezo stage	Resolution: 5 nm Working range: 250 µm

F (Carl Zeiss AG, Germany, Cat. No. 444960-0000-000), halogen-free, with $n = 1.51$ for $\lambda = 643.8\,\text{nm}$ at 23°C was used as an immersion medium for all oil objectives. Fluoromount-G™ (SouthernBiotech, USA, Cat. No. 0100-01) was used as a water-soluble and nonfluorescent mounting medium.

3.3.2 Scanning parameters

To acquire an imaging plane, the scanning head of the CLSM samples the specimen point-by-point. The total acquisition time of a single imaging field mainly depends on the number of rescans R and on the dwell time τ per scan point. Important control parameters are listed in Table 3.3.2.

Table 3.3.2: Important scanning parameters of the LSM 710.

Control parameters	Specifications
R	Number of rescans, operated in line-averaging
τ [µs]	Dwell time for a single spot position
p [%]	Relative laser power
Pixel size [µm]	Dimension of a single scan position, step size for the sampling
Field size	Number of scan positions per imaging field, defined in number of pixels or µm
Detection pinhole diameter	1 Airy unit (AU) being the best trade-off between depth discrimination capability and efficiency

3.3.3 APD detection

The fluorescence read-out signal of the FNTD was detected by high-sensitive APD operating in single-photon counting mode [39]. It possesses superior quantum efficiency compared to the PMT especially in the long wavelength range. The fluorescence signal N detected was converted into a count-rate η:

$$\eta = N/(R \cdot \tau). \tag{3.1}$$

Due to non-linearities and saturation effects the detected count rate $\eta_{detected}$ had to be converted into the actual rate η_{actual} by:

$$\eta_{actual} = -\eta_0 \cdot \ln(1 - \eta_{detected}/\eta_0) \tag{3.2}$$

with an average saturation rate η_0 of 18 MHz.

3.4 Axiovert 40C

The standard inverted wide field microscope (Carl Zeiss AG, Germany) was equipped with halogen lamp, a phase contrast filter and standard dry objectives (10x, 20x, 40x).

3.5 Leica DM IL LED

The inverted wide field microscope (Leica Microsystems, Germany) was equipped with a mercury lamp, CY3 green filter cube, a CCD camera (Leica DFC420 C) and dry objectives (10x, 20x, 40x, 63x).

3.6 STED microscope

A STED microscope in the easy STED setup was used [44]. The excitation laser line had a wavelength of 640 nm (pulse energy: 50 pJ). The STED laser line had a wavelength of 765 nm (pulse energy: 1 - 10 nJ). The STED microscope was constructed during the PhD project of Henrich, M. [45].

3.7 Software

Routines for data analysis were mainly written with Matlab® (version 7.13.0.564, R2011b). For the analysis of the FNTD image raw data, the histogram-based background subtractor [46] and particle tracker [47, 48] from the Mosaic tool collection, the open source Java program ImageJ (version 1.44p) [49, 50], as well as the open source FNTD (version 0.5.2) and libamtrack (version 0.5.4) [24] packages for R (Version 3.0.1) were used. A detailed description of the application of the particle tracker and background subtractor on the FNTD image raw data can be found in [51].

3.8 Heidelberg Ion-Beam Therapy Center

The Heidelberg Ion-Beam Therapy Center (HIT) at Heidelberg University Hospital is a therapeutic facility with integrated research [3]. Patient treatment started in November 2009. For irradiation, various ion species including protons, helium, carbon and oxygen ions are available. Besides three treatment rooms for clinical routine including the world's first carbon ion gantry allowing for 360° rotation of the beam line additional irradiation room for quality assurance and preclinical research is available.
In all rooms active beam delivery, i.e. raster scanning with a pencil beam is available. By combination of linear accelerator and synchrotron (20 m in diameter) protons and carbon ions with kinetic energy of 48 - 221 MeV and 89 - 430 MeV u^{-1}, respectively are

delivered. These energies correspond to ranges in water of 2 - 31 cm enabling to irradiate deep-seated tumors. The 3D ion beam delivery allows for a maximum irradiation field of 20 x 20 cm^{-2} in the isocenter. The proximal and distal range resolution in water are 1.0 mm and 1.5 mm, respectively. A homogeneous irradiation field is achieved by a spatial superposition of the single beam spots of 2D Gaussian profile. The spot width (FWHM) can be adjusted between 4 mm and 15 mm. Currently, the numbers of particle per second (beam intensity) can be chosen between $2 \cdot 10^8\,s^{-1}$ and $2 \cdot 10^{10}\,s^{-1}$ for protons and between $5 \cdot 10^6\,s^{-1}$ and $2 \cdot 10^8\,s^{-1}$ for carbon ions.
Unless stated all irradiations in this PhD project were carried out in the room for quality assurance and preclinical research.

3.9 Methods in cell culture

3.9.1 General culture conditions

All cells were cultured in humidified atmosphere under standard culture conditions (37°C, 5% CO_2). Cells were harvested by centrifugation for 4 min at 800 rpm at room temperature (RT). Cell culture work was performed under sterile conditions using a laminar flow hood.

3.9.2 Culture of adherent cells

All cell lines were cultured in culture flasks. At a confluence of approximately 80% cells were split. For this purpose the media in the cell culture flasks was discarded and cells were washed with 10 ml DPBS (pre-warmed to 37°C) at RT. After discarding the supernatant, 3 ml of Trypsin-EDTA solution (pre-warmed to 37°C) were added for 3 min at 37°C (5% CO_2). Detached cells were resuspended in 7 ml fresh cell culture medium (pre-warmed to 37°C) and centrifuged at RT. After discarding the supernatant the cell pellet was resuspended in fresh culture medium and seeded in new culture flasks. The ratio of cell suspension and fresh culture medium was 1:9.

3.9.3 Determination of cell density

The density of a cell culture was determined using a Neubauer chamber slide or the Cellometer Auto T4 Cell Counter (Nexcelom Bioscience LLC, USA).

3.10 Description of fluorescence dyes and assays used

CalceinAM The initial non-fluorescent calcein acetoxymethly ester is cell permeable. After cleavage (i.e. hydrolysis) by intracellular esterases calcein becomes fluorescent

and is well-retained in the cytoplasm. The stain can be used to determine the cell viability and morphology [52].

CM-DiI CM-DiI is a DiI (lipophilic carbocyanine) derivative. It is based on a thiol-reactive chloromethyl moiety that allows the dye to covalently bind to cellular thiols. Its lipophilic nature allows the dye to incorporate into cellular membranes. CM-DiI is highly fluorescent when incorporated into membranes and is weakly fluorescent in water [53].

HOECHST 33342 This nucleic acid stain (short HOECHST) intercalates in DNA. It can be used to visualize the spatial chromatin organisation in the cell nucleus [54].

Draq5 Draq5 is an anthraquinone intercalating in DNA. It can be used to visualize the spatial chromatin organisation in the cell nucleus.

Glucose Transporter Glut1 antibody The primary antibody binds to Glut1 transporters (integral membrane glycoproteins) in the cell membrane. It can be used to visualize cellular Glut1 uptake at the cell membrane [55].

OxiSelect™ DNA Double Strand Break (DSB) Staining Kit In the vicinity of a DNA double strand break (DSB) site, H2AX (a histone H2A variant) becomes specifically phosphorylated at serine 139 (termed γ-H2AX) [56]. Phospho-histone-specific primary antibody 100X binds to γ-H2AX. A secondary antibody containing the fluorescent dye can bind to the primary antibody. The indirect labeling of the actual DSB is very sensitive.

CellPlayer™ 96-Well Kinetic Caspase-3/7 Apoptosis Assay The assay contains DEVD-NucView488, an enzyme substrate for real-time detection of intracellular caspase-3 (an apoptosis-related enzyme) activity [57]. The caspase-3 recognition motif (DEVD) is bound to the nucleus-staining fluorogenic dye NucView488. This non-fluorescent substrate is highly cell permeable and is cleaved by activated caspase-3 in the cytoplasm. After cleavage, the released (still non-fluorescent) dye enters the nucleus and binds to nucleic acids such as DNA. By intercalating in DNA, NucView488 becomes fluorescent. It is retained in the cells due to its affinity to DNA.

3.11 Protocols for cellular imaging

For live cell labeling and immunofluorescence staining standard fixation and labeling protocols for fluorescence microscopy were used. The protocols refer to a staining

of A549 cells (except DEVD-NucView488/ Draq5 used to stain A431 cells). For the labeling procedure Cell-Fit-HDs were placed in wells of a 24 multiwell plate.

3.11.1 Live cell labeling

CM-DiI Cells were labeled CM-DiI at a concentration of $1.5\,\mu g\,l^{-1}$ in 1 ml DPBS for 8 min at humidified atmosphere first and then for additional 15 min at RT. After labeling, cells were gently washed twice with DPBS. Finally the Cell-Fit-HD was placed in fresh cell culture medium [9].

Calcein AM Prior to staining the cell layer was washed with DPBS. Cells were labeled with $10^{-3}\,mol\,m^{-3}$ Calcein AM (diluted in culture medium). After incubation for 30 min at RT, cells were gently washed with DPBS. The Cell-Fit-HD was placed in fresh cell culture medium [9].

DEVD-NucView488/ Draq5 Immediately after irradiation the culture medium was exchanged with a fresh one (3 ml) containing 1 μM caspase-3 substrate and 1.2 μM Draq5.

3.11.2 Immunofluorescence staining

HOECHST 33342 Cells were fixed with 4% PFA in PBS for 10 min at RT and were incubated for 5 min at RT in HOECHST 33342/ PBS solution (protected from light) with a final concentration of $2\,\mu g\,ml^{-1}$ and washed with PBS [9].

Glut1/ HOECHST 33342 Cells were fixed with 4% PFA in PBS (10 min at RT). Cells were washed with PBS. After fixation, cells were permeabilized with 0.1% Triton X-100 in PBS (10 min at RT), washed with PBS, blocked in PBS containing 2% BSA (30 min at RT), and washed with PBS. Glut1 specific primary antibody was used in a dilution of 1:200 in 1% BSA/ PBS (incubation: 1 h at RT). After washing with PBS containing 1% BSA secondary antibody Alexa Fluor 555 goat anti-mouse IgG conjugate was used in dilution of 1:1000 in 1% BSA/ PBS (incubation: 1 h at RT). Cells were washed with PBS containing 1% BSA. For nuclear counter staining, cells were incubated in HOECHST 33342/ PBS solution (5 min at RT, final concentration: $2\,\mu g\,ml^{-1}$, protected from light) and washed with PBS [9].

γ-H2AX/ HOECHST 33342 Cells were permeabilized with 0.5% Triton X-100 in PBS (10 min at RT) and washed with PBS. Nonspecific binding was blocked by 0.1% Triton X-100 and 2% BSA (30 min at RT), and washed with PBS. Phospho-histone-specific primary antibody 100X was used in a dilution of 1:100 in 1% BSA/ 0.02%

Triton-X100 (incubation: 1 h at RT). After washing with PBS containing 1% BSA/ 0.02% Triton-X100 secondary antibody Alexa Fluor 488 goat anti-mouse IgG conjugate (final concentration: 2 μg ml^{-1}) in 1% BSA/ 0.02% Triton-X100/ PBS was incubated for 45 min at RT. Cells were washed with PBS containing 1% BSA/ 0.02% Triton-X100. For nuclear counter staining, cells were incubated in HOECHST 33342/ PBS solution (5 min at RT, final concentration: 2 μg ml^{-1}, protected from light) and washed with PBS [11].

3.12 Irradiation geometry of the Cell-Fit-HD

Irradiation geometry at HIT was chosen in a way that the beam propagation vector $\vec{s}$ (parallel to the z axis in the beam coordinate system) and the k-axis of Al_2O_3:C,Mg (parallel to the z axis in the FNTD coordinate system) span the polar angle θ (Fig. 3.12.1A) [10]. The angle $\gamma = 90° - \theta$ was defined for practical purpose. It is the angle between $\vec{s}$ and the xy plane in the coordinate system of the FNTD. The azimuth angle ϕ was defined as the angle between the optical c-axis of the FNTD and $\vec{e}_{x,y}$, the projection of the ion beam onto the exposed FNTD surface. The angle ϕ played only a minor role for the irradiation setup.
The particle fluence Φ was assessed by dividing the number of particles N detected in an FNTD imaging plane by its corresponding area A:

$$\Phi = N/A. \tag{3.3}$$

3.13 Routine for ion track reconstruction in 3D

For reconstruction of the 3D ion trajectory in the Cell-Fit-HD the ion was assumed to follow a straight line [10]. A line was justified by the high energies of the incident ions, hence multi-coulomb scattering of the projectile in the crystal lattice is very small [13]. The routine was realized in Matlab.
In a first step the coordinates of the ion track centers were identified using the approaches *iw centroid, rel thres, abs max* (section 4.2.3). The coordinates are used to reconstruct the ion trajectory in the physical (FNTD) compartment. Due to statistical variation in energy deposition and inhomogeneities of the color center density, only uncertainties in the horizontal coordinates (x,y) of the ion track centers were taken into account. Uncertainty in z by the high-precision z-piezo stage (in the nm range) were neglected. The fitting procedure was split up into two separate linear regression analysis (LRA) using least-square estimation [58] for the x- and y-coordinates of the

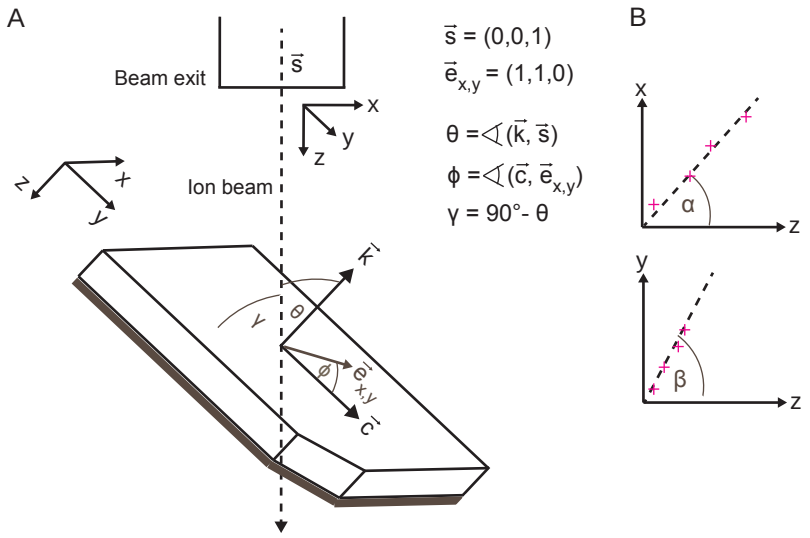

Figure 3.12.1: Irradiation geometry of the Cell-Fit-HD at HIT and ion track reconstruction. (A) The ions are traversing the detector under the angle θ – the angle between direction of propagation of the ions $\vec{s}$ and k-axis of the FNTD. The vectors $\vec{k}, \vec{c}, \vec{e}_{x,y}$ and all angles refer to the coordinate system of the FNTD; $\vec{s}$ refers to the beam coordinate system. The cell-coating is indicated by the gray layer. (B) Splitting of fitting procedure into two separate linear regression analysis for the x- and y-coordinate of the track spot centers (indicated by magenta crosses). Adapted from [10].

ion track centers respectively (Fig. 3.12.1B):

$$x(z) = a_x + b_x \cdot z \tag{3.4}$$

$$y(z) = a_y + b_y \cdot z \tag{3.5}$$

The flight direction (parametrized by θ and ϕ) of the incident ions was determined by

$$\theta = 90^\circ - \gamma, \tag{3.6}$$

$$\gamma = \arctan[(\tan^{-2}\alpha + \tan^{-2}\beta)^{-0.5}] \tag{3.7}$$

with $\tan\alpha = b_x$ and $\tan\beta = b_y$. The angle ϕ was calculated by

$$\phi = \arctan[\tan(\alpha)/\tan(\beta)]. \tag{3.8}$$

In a second step, the reconstructed ion tracks in the physical compartment was extrapolated into the biological compartment (cell layer). Besides the parameters $\Delta\theta$, $\Delta\phi$ (95% confidence intervals gained by the LRA) accuracy of track reconstruction was further expressed by the 95% prediction intervals $\mathrm{PI_{x,y}}$ on future observation (x_0, y_0). Future observations referred to locations of the ion track in different depths of the cell layer. The confidence interval with $\mathrm{PI_{x,y}} = [x_0 - a_x - b_x \cdot z_0, y_0 - a_y - b_y \cdot z_0]$ was

calculated by

$$PI_x = s \cdot t_{n-2,97.5} \cdot \sqrt{1 + \frac{1}{n} + \frac{1}{\hat{s}}(z_0 - \bar{z})^2} \tag{3.9}$$

$$s = \sqrt{\frac{\sum_{i=1}^{n} (a_x + b_x \cdot z_i - x_i)^2}{n-2}} \tag{3.10}$$

$$\hat{s} = \sum_{i=1}^{n} (z_i - \bar{z})^2 \tag{3.11}$$

$$\bar{z} = \frac{1}{n} \cdot \sum_{i=1}^{n} z_i \tag{3.12}$$

and analog for PI_y using y_i, a_y and b_y in (3.10). The parameter n is the number of ion track centers (with coordinates x_i, y_i, z_i) considered for the fit, and $t_{n-2,97.5}$ is the 97.5% quantile of the t-distribution with n − 2 degrees of freedom.

3.14 Correction for axial geometrical distortion

A negative ($n_{oil} = 1.51 > n_{cell} = 1.47$ [31]) refractive index mismatch at the immersion oil-cell layer boundary and a positive ($n_{Al_2O_3:C,Mg} = 1.76 > n_{cell}$) mismatch at the cell layer-FNTD boundary introduces spherical aberrations in the optical path of the confocal imaging [10, 31, 32]. The refractive indices of the glass bottom dish and the immersion oil were assumed to equal. To correct for the axial distortion of the focal position resulting from the negative mismatch an improved linear correction method for high NA lenses introduced in [59] was applied. The axial scaling factor (ASF) to recalculate the nominal focal position z_1 in the cell layer was determined by:

$$ASF_1 = c_1 \Delta n / n_{oil} + c_2 \arctan(c_3 \Delta n / n_{oil}) \tag{3.13}$$

with $c_1 = 1.132$, $c_2 = 0.0065$, $c_3 = 100$ and $\Delta n = (n_{cell} - n_{oil})$. To account for the positive mismatch the paraxial approximation

$$ASF_2 = n_{Al_2O_3:C,Mg} / n_{cell} \tag{3.14}$$

was applied. This approximation was used as $n_{Al_2O_3:C,Mg}$ exceeds the range of mismatch being considered for the improved linear correction method [59] and as it was previously approved to approximate experimental results well [31].

3.15 Routine for nucleus segmentation

The algorithm was used to isolate the total area covered by the cell nuclei in an image acquired by the CLSM. The nuclei were labeled with Draq5 (section 3.10). A separation of all overlapping nuclei was not possible. The routine was realized in Matlab.

1. The 2D input image A_{in} (16 bit depth, floating point data) is converted into a grayscale image A_{gray} with pixel values in the interval $[0; 1]$ (floating point data).

2. A_{gray} is converted into a 2D binary image BW (0: background, 1: foreground), based on a manually defined threshold of 0.1.

3. The binary image BW_{filled} is created by filling holes in BW. All background pixels which are surrounded by foreground pixels and can therefore not be reached by filling in the background from the edge of the image are converted into foreground pixels.

4. All foreground objects (an object is a set of connected foreground pixels) in BW_{filled} with an area smaller than 600 pixels are erased.

5. Dilation of the foreground objects in BW_{filled}. All foreground pixels are superimposed by a 2D disc-shaped binary matrix H of radius 2 pixels. All background pixels being overlapped by positioning the hot spot of H on the boundary foreground pixels are set to 1.

6. The binary image BW_{final} is created by filling holes in BW_{filled} (according to step 3). The resulting foreground objects account for the nuclei.

4 Experiments

The objective was to develop a FNTD-based hybrid detector (termed Cell-Fit-HD) enabling 3D spatiotemporal correlation studies of cell damage with respect to the intracellular ion traversal in clinical ion beams. The first milestone was to develop the actual hybrid composite and to evaluate its potential application spectrum (**4.1 Engineering Cell-Fit-HD**). Experiments were carried out covering of the FNTD (the physical compartment) with cell layers thus creating viable and uniform biological compartments. A protocol was developed to image the color centers transformed by the swift particles in the physical compartment and various fluorescent biomarkers for identification of different cell structures in the biological compartment by the very same CLSM. For a functional read-out, i.e. to achieve spatial correlation between single ion hits in the cell coating and the biological response the ion traversals had to be reconstructed in 3D using the depth information gained by the FNTD read-out. Making use of the trajectory information provided by the FNTD the accuracy of 3D track reconstruction of particles traversing the hybrid detector was investigated in the second part (**4.2 Ion track reconstruction in 3D**). In a validation study the Cell-Fit-HD was proved to be a radiobiological tool enabling accurate spatial correlation between ion traversals and subsequent radiation damage on a subcellular level (**4.3 DNA damage response to particle irradiation**). Location and orientation of the actual ion tracks extrapolated from the physical compartment were compared to their corresponding biological surrogates in the cell layer. Besides the sole spatial correlation it was of great interest to extend the colocalisation and directly correlate number and quality of cell damaging events to microscopic beam parameters. It was investigated in parallel whether it is principally possible to resolve the particle spectrum (e.g. in the tumor volume) from the FNTD read-out signal (**4.4 Resolving therapeutic particle spectrum**). To do so the possibility was studied to deduce from a single track spot – the ion's characteristic signature left in the detector after traversal – information on ion typ and energy. By high resolution (STED) microscopy the diffraction-limited read-out barrier was overcome. The track spot profile was compared to the profile of a corresponding radial dose distribution (RDD) model. In a final experiment the Cell-Fit-HD was utilized to correlate survival of individual cells to the energy deposition in the nucleus by the impinging ions (**4.5 Probing single cell fate after therapeutic ion irradiation**). In order to assess the spatial microscopic energy deposition distri-

bution the microscopic physical parameters of each incident were extracted.
All experiments were carried out independently with different objectives. They are therefore listed separately. However, data sub sets gained by a sequential read-out of the Cell-Fit-HD could be used for several experiments, especially for sections 4.2 and 4.3. This is highlighted in Table 4.2.1 displaying the settings for the read-outs.

4.1 Engineering Cell-Fit-HD

In a first step it was tested whether the FNTD provides a biocompatible surface for prolonged cell culture. To evaluate cell adherence, cell viability and conformal coverage, different seeding densities and alternative coating with fibronectin (a component of the extracellular matrix) were tested. It was evaluated whether autoclaving or prolonged exposure to high humidity under standard culture growth conditions could affect the chemical reactivity of the Al_2O_3:C,Mg surface. In a second step to test whether the FNTD as a substrate interferes with standard fixation and staining procedures, the biological compartment of the Cell-Fit-HD was labeled with a series of dyes. By using various biomarkers viability, metabolism, and density of the cell coating was characterised. In a third step an imaging protocol was developed to acquire 3D image stacks of the physical and biological compartment sequentially by a single CLSM without removing the cell layer at any time. It was tested whether technical limitations by the CLSM interferes the hybrid detector read-out. It was tested whether the development of the hybrid composite affects the signal quality of the sole FNTD read-out. It was also tested whether the read-out of the physical compartment interferes with biological compartment as well as its read-out quality and vice versa. The corresponding publication entitled *"Engineering cell-fluorescent ion track hybrid detectors"* is enclosed in the appendix C.

4.1.1 Creating the hybrid composite

The polished surface of the FNTD was coated with six different permanent human and murine cell lines (of varying seeding densities, Table 4.1.1). Prior to the coating, FNTDs were autoclaved and washed with DPBS. Pre-coated FNTDs were placed in a bath-type sonicator for 15 min (by placing the detectors in DPBS-filled PCR tubes). Before autoclaving the pre-coated detectors were washed with DPBS to remove any solid left overs. For the coating each single FNTD was placed in a well of a 24 multiwell plate and was covered with 0.5 ml cell-suspension. The cell-coated FNTDs were kept in humidified atmosphere until a confluent monolayer had developed. At regular intervals the cell coating was monitored using a wide-field microscope equipped with phase contrast filter (Axiovert 40C). The culture medium was changed the first time after 24 h and then in 48 h intervals. To test alternative covering, FNTDs were coated with fibronectin (of varying concentrations, Table 4.1.1) and were incubated for 50 min in humidified atmosphere. Afterwards they were gently washed twice with DPBS and covered with cells. The cells were monitored for more than 120 h (5 d).

Table 4.1.1: Cell coating of the FNTD. The polished surface of the FNTDs were coated with different cell lines with and without a fibronectin intermediate layer. Each well of the multiwell plate contained 500 μl. Except SMA-560 (murine cell line) human cell lines were used. Adapted from [9].

Cell line	Seeding density [1/well]	Fibronectin [ng/ml]
SMA-560	10 000 150 000 150 000	2.5, 5, 10, 20 2.5, 5, 10, 20 -
U87	10 000 150 000 150 000	2.5, 5, 10, 20 2.5, 5, 10, 20 -
PC3	200 000 200 000	2.5 -
A431	200 000 200 000	2.5 -
A549	50 000 150 000 150 000	- 1, 2.5, 5 -

4.1.2 Cell labeling and immunofluorescence staining

In the following steps the focus was on A549 cells as they formed a uniform, viable, tightly packed epithelial like monolayer. The biological compartment was labeled with a series of dyes for live cell imaging and histochemical stainings for fluorescence microscopy. For the labeling and fixation standard protocols were used (section 3.11).
For single cell tracking and to test conformal coverage of the cell layer the biological compartment was labeled with CM-DiI. To test cell viability and metabolism, the biological layer was labeled with Calcein AM. To visualize the cellular membranes as well as to detect cell-cell adhesion and to monitor the cell density, Glut1/ HOECHST dual stain was used. To monitor the density of the cell coating after irradiation the biological compartment was fixed 15 min after irradiation and stained with HOECHST.
For the imaging, the corresponding microscopy settings are listed in Table 4.1.2. The imaging parameters (CLSM: p, τ and R) were adjusted to avoid photobleaching, phototoxicity and any other hazard to the specimen. For imaging with Leica DM IL LED the Cell-Fit-HDs were placed in a 24 multiwell plate. For imaging with the CLSM, glass bottom culture dishes were used. Fluoromount-G$^{\text{TM}}$ was used as a mounting medium for Glut1/HOECHST dual stain. For HOECHST single stain, PBS was used. For live cell imaging (Calcein AM, CM-DiI) cell culture medium was used as mounting medium.

4.1.3 Therapeutic ion irradiation

Perpendicular ($\theta = 0° \pm 5°$) carbon ion ($^{12}C^{6+}$) irradiations of Cell-Fit-HD were performed with the therapy beam at HIT (section 3.12 and Fig. 4.1.1). The ion beam fluence was adjusted to $1.5 \cdot 10^6\,\text{cm}^{-2}$ using controls of the treatment system. This

Table 4.1.2: Fluorescent dyes and the microscopy settings used. The detection window for Calcein AM could in principle be narrowed around the emission peak at 513 nm. As Calcein AM was the single dye detected, no potential spectral overlap with other dyes was possible.

Dye	Microscope	Excitation	Emission	Detection
CM-DiI	Leica DM IL LED (10x/ 63x)	Mercury lamp	CY3 green filter	CCD camera
Calcein AM	LSM 710 (63x oil)	488 nm laser line	MBS 488 nm	PMT: 493–617 nm
HOECHST	LSM 710 (63x oil)	405 nm laser line	MBS 405 nm	PMT: 410-550 nm
Glut1/ HOECHST	LSM 710 (40x oil)	561 nm/ 405 nm laser line	MBS 458/561, MBS 405 nm	PMT: 566-697 nm / 410-550 nm

results in an average of 1.3 hits per nucleus (all nuclei were assumed to be of equivalent size with an area of 10 x 10 μm^2). A 12 x 12 cm^2 field was irradiated homogeneously using raster scanning with a pencil beam of 10.1 mm in diameter (FWHM) and a distance of 2 mm between two raster spots. Approximately 60,000 particles were delivered in each spot. The Bragg peak was extended by using a 3 mm Ripple filter. The cell layer was placed in the rising flank of the Bragg peak with a corresponding energy of 52 MeV u^{-1} (initial carbon ion energy of 270.5 MeV u^{-1}, corresponding equivalent range in water r_{H_2O} = 13.70 cm) [24]. As stopping material 11.30 cm of PMMA with r_{H_2O}= 13.16 cm was placed in front of a 24 multiwell plate containing the cell-coated FNTDs. The horizontal-aligned ion beam in the quality assurance room required a vertical positioning of the multiwell plate for irradiation under $\theta = 0°$. The FNTDs were 0.5 mm thick with equivalent range in water r_{H_2O}= 1.65 mm. The back side of the FNTDs without cell coating were facing the incident beam and were attached to the bottom (polystyrene with r_{H_2O}= 1.2 mm) of the multiwell plate by agarose droplets. The air gap between the culture well and the PMMA was not considered in the total r_{H_2O}. In order to keep the cell coating viable during irradiation the wells were filled with cell culture medium. The total amount of materials in front of the isocenter (vacuum exit window, beam application monitoring system, air) corresponds to a r_{H_2O} of 2.89 mm.
To compute the r_{H_2O} of a material, the corresponding water equivalent path length (WEPL) value was multiplied by the thickness of the material. The WEPL value for PMMA (1.165) was taken from [60], the values for Al_2O_3:C,Mg (3.29) and polystyrene (1.04) were gained according to personal communication (Christoph Tremmel).

4.1.4 Sequential read-out protocol

After irradiation the hybrid detector was placed in a well of a 24 multiwell plate and the biological compartment was fixed and stained for HOECHST 15 min after irradiation without removing the cell layer from the FNTD (section 3.11.2).
The Cell-Fit-HD was mounted in a glass bottom culture dish, filled with PBS. The

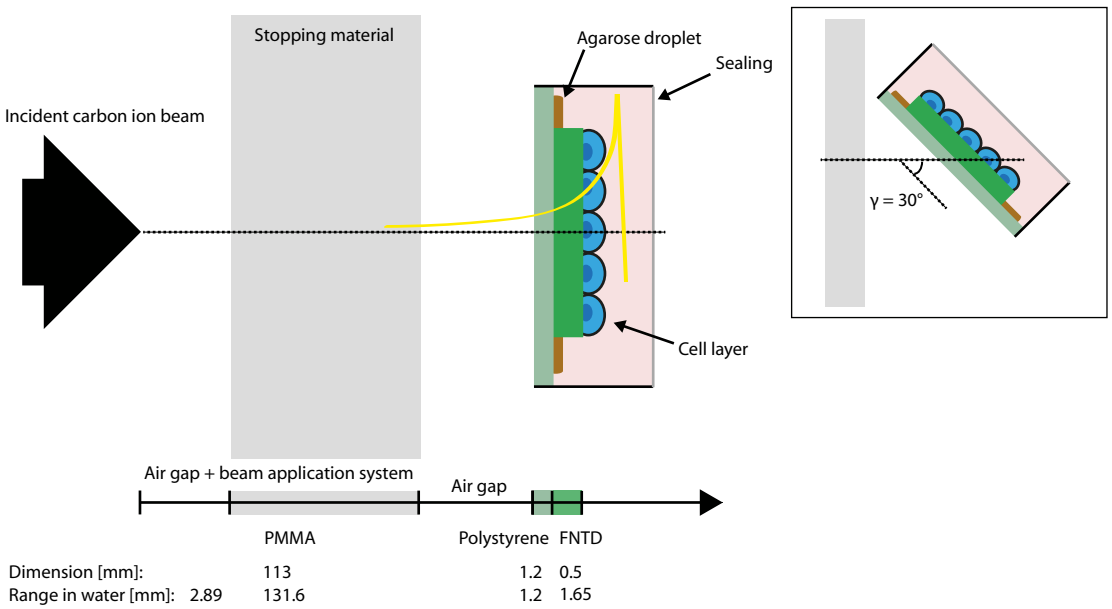

Figure 4.1.1: Irradiation setup at HIT. The Cell-Fit-HD was irradiated perpendicular ($\theta = 0°$) to the incident therapeutic carbon ion beam. The cell layer was placed in the rising flank of the Bragg-peak as schematically indicated by the yellow line. Only a single well of a multiwell plate is shown. The FNTD is attached by agarose droplets to the polystyrene bottom of the multiwell plate. The well is filled with culture medium to keep the cells viable during irradiation. It is sealed with Parafilm M®. The air gap between the PMMA block and the multiwell plate is neglected as the corresponding energy loss is very small. The range in water (r_{H_2O}) of all elements in the beam path (position and fluence monitors) between exit window of the beam line and isocenter of the incident ion beam is 2.89 mm. Insert: Angular irradiation ($\theta = 60°$, $\gamma = 90° - \theta$) with adapted irradiation setup and adapted geometrical dimensions. Adapted from [9].

biological and the physical compartment were imaged in-situ in two consecutive steps by the very same CLSM (Fig. 4.1.2). The cell layer remained on the FNTD and no post-chemical processing of the FNTD was necessary. The CLSM was equipped with the 63x oil objective and was operated in APD photon-counting for the FNTD and in PMT detection mode for the cell layer read-out. T-PMT detection was used in parallel in both read-outs. The detector pinhole aperture was set to 1 AU.
In the first step, the physical compartment was scanned by the 633 nm Helium Neon laser line (100% transmission). The MBS 488/561/633 nm and the 655 nm long-pass detection filter were placed in the optical path. In a second step, the cell layer was imaged with a 405 nm diode laser line (4.0% transmission) for HOECHST. The MBS 405 nm was used and the PMT detection window was limited to 410 nm - 495 nm. For the FNTD and cell layer acquisition, R and τ were set to 4 and 2.80 μs, respectively (Table 4.2.1).
In both read-outs, the size of the imaging field was 134.784 x 134.784 μm^2 with a total number of 1152 x 1152 pixels and a pixel size of 0.117 x 0.117 μm^2 (estimated according to Rayleigh criterion). The acquired FNTD image stack was adjusted to cover an axial range of about 120 μm (measured from the detector surface) with a z-interval ($\widehat{\Delta z}$) of 3 μm. The acquired cell layer stack covered a range of approximately 10 μm ($\widehat{\Delta z}$= 0.3 μm). The FNTD image stack was extended into the cell layer and vice versa.

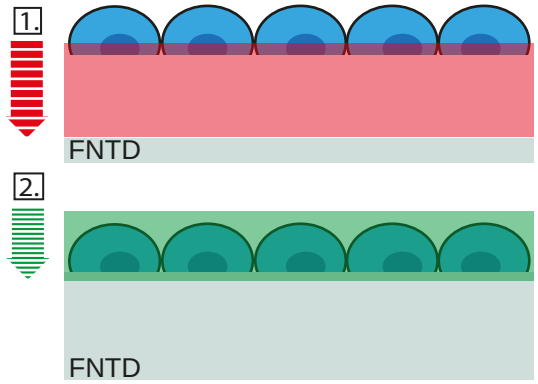

Figure 4.1.2: Sequential read-out of the Cell-Fit-HD. The imaging is first performed on the physical (FNTD) and after that on the biological compartment (cell layer). The optical sectioning (determined by $\widehat{\Delta z}$) of the biological and physical compartment is indicated by the striped arrows. Taken from [9].

4.2 Ion track reconstruction in 3D

In this study FNTD signals were analysed after perpendicular ($\theta = 0°$) and angular ($\theta = 60°$) carbon ion irradiation of the Cell-Fit-HD. The depth information gained by the FNTD read-out was then used to reconstruct the ion track in the physical and to extrapolate it into the biological compartment. Correction for axial geometrical distortion arising from refractive index mismatches in the optical imaging path was introduced. The potency of acquiring 3D information on energy deposition und angular irradiation was reported in [61]. The corresponding publication entitled *"Ion track reconstruction in 3D using alumina-based fluorescent nuclear track detectors"* is enclosed in the appendix D.

4.2.1 Creating Cell-Fit-HD and irradiation setup

Cell-Fit-HDs were created by covering FNTDs with a confluent A549 monolayer (plating density: 100 000 ml^{-1}, 0.5 ml per well) with the protocol described in section 4.1.1. 15 minutes after carbon ion irradiation the cells (remaining on the FNTD) were fixed and stained with HOECHST (section 4.1.2).
Irradiations were performed under θ of $0° \pm 5°$ and $60° \pm 5°$ (Insert, Fig. 4.1.1). The irradiation setup under $\theta = 0°$ is described in section 4.1.3. Under $\theta = 60°$, 11.05 cm of PMMA absorber with a corresponding r_{H_2O}= 12.87 cm was placed in front of the multiwell plate. In addition, the multiwell plate was placed at an angle of $\gamma = 30° \pm 5°$ towards the incident ion beam. The different PMMA thickness compared to $\theta = 0°$ results from the different thickness of the bottom of the multiwell plate (polystyrene, $\theta = 0°$: r_{H_2O}= 1.2 μm, $\theta = 60°$: r_{H_2O}= 2.5 μm) and of the FNTD ($\theta = 0°$: r_{H_2O}= 1.65 mm, $\theta = 60°$: r_{H_2O}= 3.29 mm).

4.2.2 Confocal read-out

Irradiated Cell-Fit-HDs were mounted in glass bottom culture dishes (filled with PBS) and were read-out with the protocol described in section 4.1.4. The CLSM was equipped with the 63x oil objective. Important acquisition parameters for the physical and biological compartment are listed in Table 4.2.1.

4.2.3 Ion track center detection

For the subsequent image processing the acquired raw images (without background-correction) were converted into floating point data (with pixel values in the interval $[0; 1]$). A routine in Matlab was developed to a) detect the ion track centers in all selected planes of the recorded image stack and to b) reconstruct the ion track in the Cell-Fit-HD based on the positions of the identified centers (section 3.13). Three

Table 4.2.1: Image acquisition parameters for all sequential read-outs of the physical (FNTD) and the biological (cell layer) compartment. Experiment-ID: section 4.1 (**A**), section 4.2 (**B**), section 4.3 (**C**) and section 4.5 (**D**). Partly the data (especially for the physical compartment) gained by a single sequential read-out could be used for different experiments (A,B,C). However, each experiment had a different objective. #: number of planes of an image stack. (*) The data set is displayed for completeness but not described in the text (B: Fig. 1B)

ID		p [%]	τ [µs]	R	Pinhole [AU]	Image size [pixel]	Pixel size [µm²]	#	$\widehat{\Delta z}$ [µm]	Axial range [µm]	MBS [nm]	PMT [nm]	APD [nm]	T-PMT	Tile scan
FNTD															
A, B, C *	Perpendicular	100	2.80	4	1	1152 x 1152	0.117 x 0.117	41	3	120	488/561/633	no	> 655	yes	single field
B, C	Angular	100	4.97	4	1	1300 x 1300	0.104 x 0.104	33	3	96	488/561/633	no	> 655	yes	2 x 2
D	Perpendicular	40	12.90	4	1	2000 x 2000	0.117 x 0.117	2	10	10	488/561/633	no	> 655	yes	single field
Cell layer															
A, B, C *	HOECHST	4	2.80	4	1	1152 x 1152	0.117 x 0.117	55	0.3	16.2	405	410 - 495	no	yes	single field
											488	493 – 630			
C *	γ-H2AX	1.2													
B, C	HOECHST	5.5	4.97	4	1	1300 x 1300	0.1038 x 0.1038	67	0.3	20.1	405	410 - 495	no	yes	2 x 2
											488	493 - 630			
C	γ-H2AX	1.5													
D	Draq5	1	1.61	2	1	2000 x 2000	0.117 x 0.117	11	2	20	488/561/633	no	> 655	yes	single field
D	NucView 488	2									488	499 – 600	no		

different approaches to detect the center of the track spots and the resulting accuracy in track reconstruction were compared:

(A) Detection of intensity-weighted centroids applying a global threshold (*iw centroid*):
all pixels within a region of interest (ROI) with values greater than a manually defined global threshold of 0.4 were considered for the calculation of the intensity-weighted centroid.

(B) Detection of intensity-weighted centroids applying a dynamic threshold (*rel thres*):
the threshold was set to 2/3 of the maximum pixel value within an ROI.

(C) Detection of the absolute intensity maximum (*abs max*):
the pixel with the maximum value within the ROI was considered as the track spot center.

The ROI was defined as a window limited to 30 x 30 pixels for perpendicular and 120 x 30 pixels for angular irradiation.
Firstly, in a manually selected first and last imaging plane (i_{first}, i_{last}) of an acquired image stack, threshold-based image segmentation of an ROI (with the above defined dimension and centered at the expected ion track spots) was applied. A global threshold of 0.4 showed best suitability. A calculation of the intensity-weighted centroids accounting for the coordinates of the temporary first and last ion track centers $\hat{x}_{first}$ and $\hat{x}_{last}$ was applied. In the following steps, the ROI in the imaging plane i ($i = i_{first}...i_{last}$) was centered at the position of the connecting line $\overline{\hat{x}_{first}\hat{x}_{last}}$ in i. The coordinates of the ion track centers were identified by using the above described approaches (*iw centroid, rel thres, abs max*). Each ROI contained only a single track spot $(x, y)_i$. Due to possible δ electron tracks sprouting from a track spot each ROI could contain several local intensity maxima dividing it into several sub-areas. The largest area was isolated and considered to account for the track core (a halo of secondary electrons around the center of a track spot, Fig. 5.2.1). The smaller areas mainly arise from dense energy depositions induced by strongly scattered δ electrons having enough energy to leave the ion track core.

4.2.4 Quantifying accuracy of ion track reconstruction

Accuracy of ion track reconstruction in 3D was quantified by the parameters $\Delta\theta$, $\Delta\phi$ (95% confidence intervals gained by the LRA) and by the 95% prediction interval $PI_{x,y}$ of the extrapolated track location in the cell layer (section 3.13).
20 tracks each for angular and perpendicular irradiated Cell-Fit-HDs were reconstructed in the physical and were extrapolated (with depth increments of 0.1 μm) into

the biological compartment of constant thickness of 10 μm. Next to the different detection approaches (*iw centroid, rel thres, abs max*, above), the total number n of track spots considered for a single fit and the distance in z between two neighboring track spots (Δz) were varied to study their impact on accuracy of track reconstruction:

1. Δz= 3 μm, n= 21 track spots
2. Δz= 6 μm, n= 11 track spots
3. Δz= 15 μm, n= 5 track spots

A maximum n of 21 was chosen which corresponds to a 60 μm fitting range in z. This is the range allowing to track a traversing ion within a single imaging field (135 x 135 μm^2) under angular irradiation. For greater ranges, the imaging field has to be moved, i.e. tile scans have to be performed. In this study all extrapolations into the biological layer were assumed to start at a same depth of 3 μm below the FNTD surface. The position of the surface in z was determined by the intensity of the HOECHST signal. It disappears at the cell-FNTD boundary. Simultaneously, the background signal in the HOECHST channel is increasing at the transition into the physical compartment as excitation by 405 nm causes a photoionization of the pristine F_2^{2+}(2Mg) aggregate defects located beneath the FNTD surface.

4.2.5 Correction for axial geometrical distortion

The refractive index mismatch occurring in the optical imaging path was compensated by introducing axial scaling factors (ASFs, section 3.14). The actual position z_{act} of the focal point in z (origin is at the well bottom of the glass bottom culture dish) in the physical compartment was calculated by

$$z_{act}(z) = ASF_1 \cdot z_1 + ASF_2 \cdot z. \tag{4.1}$$

The parameters ASF_1 and ASF_2 account for the immersion oil-cell layer and cell layer-FNTD interfaces. The parameter z_1 is the nominal thickness of the cell layer (distance between the well bottom of the glass bottom culture dish and the detector surface) and z is the nominal position in the FNTD (measured from the detector surface). The aqueous medium between dish bottom and cells was neglected in the correction for axial distortion.
Uncertainty Δs in the position of the surface s translates directly into the error $\hat{z}_{act}$ and $\hat{x}$ (error of the location of the track in the horizontal):

$$z_{act}(z, \Delta s) = z_{act}(z) \pm \hat{z}_{act}(\Delta s) = z_{act}(z) \pm (ASF_1 - ASF_2)\Delta s \tag{4.2}$$

$$\hat{x}(\theta, \Delta s) = (ASF_1 - ASF_2)\Delta s / \tan(90° - \theta) \tag{4.3}$$

starting from

$$z_{act}(z) = ASF_1(s - o_1) + ASF_2\left[(\hat{n} - 1)\widehat{\Delta z} - (s - o_2)\right] \tag{4.4}$$

and defining $z := (\hat{n} - 1)\Delta z$ as a function of the actual plane number $\hat{n}$ of the acquired image stack and the interval between two consecutive image planes $\widehat{\Delta z}$. The parameters o_1 and o_2 are the respective positions in z of the first imaging plane of the cell and of the FNTD image stack.

4.3 DNA damage response to particle irradiation

To prove spatial correlation between particle traversal and subcellular response by the Cell-Fit-HD, biomarkers labeling radiation-induced γ-H2AX foci (RIF) at DSB sites in the cell layer were used (section 3.10). The RIFs form a distinct pattern along the ion trajectory hence creating a surrogate for the ions' flight paths in the cell layer. The corresponding publication entitled *"Subcellular Spatial Correlation of Particle Traversal and Biological Response in Clinical Ion Beams"* is enclosed in the appendix E.

4.3.1 Design of validation study

Based on the initial experiments under perpendicular irradiation (not described here, see B: Fig. 1B) the validation study was designed to prove spatial correlation with

a) a minimal probability of coincidental correlation (i.e. false-positive events) at

b) a worst accuracy in ion track reconstruction from a physical-mathematical aspect.

Angular irradiation creating prolonged RIF sequences along a particle track [62] was applied meeting above-named side-conditions (Fig. 4.3.1A). Under perpendicular irradiation sequences with a minimum number of distinct RIFs (due to a short path length in the nucleus) would give rise to coincidental correlation. A RIF sequence was further defined to comprise at minimum three distinct γ-H2AX foci. Such signature allows for a robust study of high specificity and lowers the probability of coincidental correlation as not all foci necessarily account for irradiation induced DSBs [63, 64]. To analyse the 3D geometry of the RIF sequences, the feet of the perpendicular (FOPs: intersection of the ion track with the perpendicular of the corresponding γ-H2AX foci) were assessed.

4.3.2 Creating Cell-Fit-HD and particle irradiation

Cell-Fit-HDs were created by covering FNTDs with a confluent A549 monolayer (plating density: 50 000 ml^{-1}, 0.5 ml per well) with the protocol described in section 4.1.1. The Cell-Fit-HDs were kept in humidified atmosphere until the confluent monolayer had developed after 48h. The cellular compartment of Cell-Fit-HD was fixed 15 min after irradiation and stained for γ-H2AX and HOECHST (section 3.11.2).
Cell-Fit-HDs were irradiated angularly ($\theta \approx 60°$) with carbon ions (initial 270.55 MeV u^{-1}, rising flank of the Bragg peak, $r_{H_2O} = 13.70$ cm). The irradiation setup (Insert, Fig. 4.1.1) and the beam parameters are described in sections 3.12 and 4.2.1.

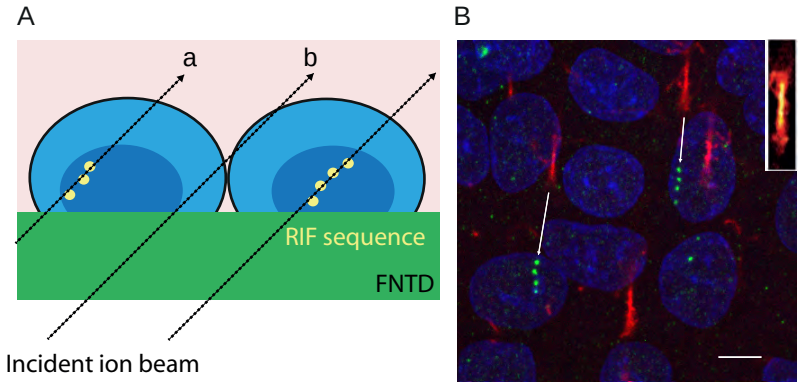

Figure 4.3.1: Cellular response to angular ion irradiation. (A) RIF (i.e. γ-H2AX foci) sequences create a surrogate for the ions' flight paths in the cell nuclei. False-negative (a) and false-positive (b) events are at equilibrium in the ion hit statistics. (B) A superposition of a maximum intensity z-projection (cell nuclei blue, γ-H2AX foci green) of cellular response data with an imaging plane of the acquired FNTD stack proximate to the detector surface is shown. The arrows connect the track spots of the corresponding ion tracks to the radiation-induced γ-H2AX foci sequences. Only a section of the total imaging field is shown. Inset: Elongated track spot under angular irradiation. Scale bar, 5 μm. Adapted from [11].

4.3.3 Confocal read-out

For the sequential read-out of the Cell-Fit-HD the CLSM was equipped with the 63x oil objective. The protocol for the sequential read-out is described in section 4.1.4. The imaging parameters for the physical (FNTD) and biological (HOECHST and γ-H2AX labeling) compartment of the angular irradiated Cell-Fit-HDs are listed int Table 4.2.1. To increase the imaging field, 2x2 adjacent images (a tile scan) were taken. The glass bottom culture dish was filled with PBS.

4.3.4 Ion track reconstruction in 3D

Ion traversals corresponding to a RIF sequence (with minimum of three γ-H2AX foci) were reconstructed using the FNTD read-out signals and were extrapolated into the biological compartment (Fig. 4.3.1B). Methods and routines used for the detection of the ion track centers, reconstruction (Δz= 3 μm) and extrapolation are described in sections 3.13, 4.2 and 6.2.5. Detection of intensity-weighted track spot centroids (*iw centroid*) was applied with a global threshold of 0.4 (with pixel values in the interval $[0; 1]$). For less intense track spots the threshold was adapted to 0.3 and 0.2. Intersecting ion trajectories hindered partly an automated detection of the track spot centers. The dimension of the ROI containing the expected track spot (section 4.2.3) had to be adapted in order not to falsify the actual coordinates of the centroids by an overlapping neighboring track spot. A background correction was not applied for the track reconstruction.

To account for systematic errors in the ion track reconstruction, the uncertainty Δs in the position of the FNTD surface in z was assumed to be 1 μm. Further, small-scale

scratches and digs in the polished detector surface (section 3.2) were neglected and the position of the surface in z was assumed to be constant. Concerning correction of axial geometrical distortion the thickness of the cell layer was assumed to be constant (sections 3.14 and 4.2.5).

4.3.5 Ion hit statistics

For the ion hit statistics of the biological compartment (but not for the actual validation study), a hit was counted if the track center at the FNTD-cell boundary falls into the maximum intensity projection of the nucleus (HOECHST signal). All ion tracks were assumed to have the same orientation, parameterized by θ_{ion} and ϕ_{ion}. Due to the fact that the majority of tracks had the same orientation false positive and false negative were at equilibrium (Fig. 4.3.1A). The number of such hits was multiplied by

$$A_c/A_n \tag{4.5}$$

to calculate the total number of cellular hits. The parameters A_c and A_n are the mean area of cell and of nucleus evaluated by the HOCHEST signal. All cells in the imaging field were taken into account, i.e. also cells being partially located in the imaging field. For the validation study however the hits per nucleus were assessed by a track reconstruction of the corresponding ions traversing the 3D nucleus body. The nucleus body was gained by a 3D reconstruction of the HOECHST data.
To categorize the ion traversals by carbon ions and by lighter fragments the background subtractor was applied on the FNTD image stack with a sliding window of a length of 80 pixels (section 3.7). In the imaging plane proximate to the detector surface (approximately 10 μm in depth) each track spot was masked by a rectangle of dimensions $\Delta x \cdot \Delta y = 20 \cdot 100$ pixels. The sizee of the rectangle proved to be best suitable to include the whole ellipsoidal track spot (Insert, Fig. 4.3.1B) and to minimize adjacent background. The detected intensity values N in the rectangle were converted into the count rate η_{actual} (Eqs. 3.1 and 3.2) and were summed. The saturation rate η_0 was 16.2 MHz.

4.4 Resolving therapeutic particle spectrum

To resolve the incident particle spectrum in a target volume, information on type and energy of the single ions are irremissible. Both parameters can not be assessed directly from the FNTD read-out signals. It was therefore aimed to find surrogates for the LET and the maximum secondary electron range (r_{max}) being related to ion type and energy. The correlation between the fluorescence track amplitude and the LET has already been investigated in other studies but using a different confocal microscope for the FNTD read-out [38]. Despite the explicit interest in clinically relevant ion types and energies the spectrum was extended to particles of higher atomic number ($Z \geq 12$). Amongst others they are released by the interaction of cosmic radiation with spacecraft shielding hence being a severe threat in manned space mission.
In a first step the confocal read-out data was investigated. In a second step nanoscopic microscopy (STED) was employed to reduce the impact of the PSF on the read-out signals. It was investigated whether it is possible to resolve the minimal feature in a track spot by STED microscopy. It was also investigated whether it is principally possible to resolve the radial dose distribution (RDD) of the swift ions in Al_2O_3:C,Mg. The corresponding publication entitled *"Spatial correlation between traversal and cellular response in ion radiotherapy - Towards single track spectroscopy"* is enclosed in the appendix A.

4.4.1 Range of ion types and energies

For a reference data set FNTDs were irradiated with a broad range of ions and energies (Table 4.4.1). Unless explicitly stated irradiations were performed during the Master's thesis by Julia Osinga at HIT, at RADiation Effects Facility RADEF at the University of Jyvaeskylae, Finland, at SNAKE, Maier-Leibnitz-Laboratorium, Munich, Germany, and at the Max Planck Institute for Nuclear Physics in Heidelberg, Germany [42]. To ensure mono-energetic particles all FNTDs were placed in the entrance channel, perpendicularly towards the incident ion beam ($\theta = 0°$). Despite termed LET here, actually the stopping power S (also termed LET_∞, section 2.3) in Al_2O_3 was calculated.

4.4.2 Confocal read-out

Image stacks of the FNTDs were acquired with the CLSM, equipped with the 63x oil objective. The imaging parameters (MBS 488/561/633 nm, APD detection: > 655 nm, detection pinhole: 1 AU) used were equivalent to the parameters used for the sequential read-outs (Table 4.2.1). The detected fluorescence signal was converted into the actual count rate η_{actual} (section 3.3.3). The scanning parameters (p= 86%, τ= 89.6 μs, R= 4) were adjusted to avoid detection saturation effects for lighter ions (H-1 and C-

Table 4.4.1: Particle spectrum for FNTD irradiation including parameters for image acquisition and image processing. Parameters of the particle tracker refer to radius (pixel), cut-off and percentile (%). The LET (strictly S) and maximum secondary electron range (r_{max}) values refer to Al_2O_3 and were calculated using libamtrack [24]. (*) Irradiation was performed in vacuum. Gray shading: additional read-out by STED microscopy.

Ion type	Energy [MeV u^{-1}]	LET [keV µm^{-1}]	r_{max} [µm]	p [%]	τ [µs]	R	Image size [pixel]	Pixel size [µm^2]	Depth [µm]	Particle tracker		
$^{1}H^{+}$ *	3.00	34.64	0.08	86	89.6	4	1152 x 1152	0.117 x 0.117	30	3	3	0.2
$^{1}H^{+}$ *	6.00	20.79	0.26							3	3	0.2
$^{1}H^{+}$ *	12.00	12.27	0.86							3	3	0.2
$^{1}H^{+}$ *	21.00	7.90	2.23							3	3	0.2
$^{1}H^{+}$ *	49.37	4.00	9.53							3	3	0.2
$^{12}C^{5+}$ *	4.00	951.80	0.13						30	3	3	0.2
$^{12}C^{6+}$	91.14	90.23	27.02							3	3	0.2
$^{12}C^{6+}$	114.60	76.92	39.88							3	3	0.01
$^{12}C^{6+}$	152.05	62.68	64.50							3	3	0.01
$^{12}C^{6+}$	224.81	48.59	125.39							3	3	0.2
$^{12}C^{6+}$	428.77	34.42	375.80							3	3	0.2
$^{24}Mg^{8+}$ *	4.00	3203.60	0.13						10	3	3	0.2
$^{32}S^{9+}$ *	3.13	5524.17	0.09							3	3	0.1
$^{56}Fe^{15+}$ *	5.19	9457.75	0.21							3	3	0.09
$^{56}Fe^{15+}$ *	9.30	7517.21	0.56							3	3	0.09
$^{84}Kr^{22+}$ *	9.40	12337.28	0.56							3	3	0.3
$^{131}Xe^{35+}$ *	5.50	24246.50	0.23							6	3	0.3
$^{131}Xe^{35+}$ *	9.30	21687.85	0.56							6	3	0.2

12). Heavier ions (Mg-24, S-32, Fe-56, Kr-84, Xe-131) were added subsequently to the reference data set. The imaging parameters were retained to ensure a comparability of all acquired data. To maximize the fluorescence intensity signal the FNTDs were mounted in glass bottom culture dishes accordingly (section 3.2). The read-out depth was adjusted to approximately 30 μm, measured from the detector surface. For incident ions stopping in the FNTD the read-out depth had to be limited to 10 μm (marked in Table 4.4.1).

4.4.3 Parameterization of the intensity profile of a track spot

It was tested whether the maximum intensity signal of a track spot and its FWHM are possible measures for the LET and r_{max}. To correct for the inhomogeneous large-scale background (i.e. greater than the actual track spot) the background subtractor was applied on the FNTD image stack with a sliding window of length 15 pixels (showed best suitability). The track spots were detected using the particle tracker (section 3.7) with the parameters listed in Table 4.4.1. To define an ROI each identified track spot was masked by a disc of radius r_d with $5 \leq r_d \leq 20$ pixels. To exclude incomplete (i.e. at the margin of the imaging field) or overlapping track spots, the area of the ROI had to be in the interval $[0.95 \cdot r_d^2\pi; 1.3 \cdot r_d^2\pi]$. The intensity profile of a track spot was parametrized by its global intensity maximum and its FWHM. Both parameters were assessed by either

a) direct measurements or

b) by fitting a 2D symmetrical Gaussian function.

In the first approach the FWHM of the track spot was computed by

$$\text{FWHM} = \sqrt{4A_{FW}/\pi}. \tag{4.6}$$

It is the diameter of a disc with the area A_{FW} of all pixels with a count rate $\eta \geq 0.5 \cdot \hat{\eta}$ ($\hat{\eta}$: maximum count rate). The 2D Gaussian fit, second approach,

$$\eta(x, y, A, \sigma, B) = A/(2\pi\sigma^2) \cdot \exp(-0.5/\sigma^2((x - x_0)^2 + (y - y_0)^2)) + B \tag{4.7}$$

with the peak value $\hat{A} = A/(2\pi\sigma^2)$ had the advantage of directly assessing and considering constant small-scale background B still present in the ROI. FWHM and σ are related by $\text{FWHM} = 2\sqrt{2\ln 2} \cdot \sigma$.
For each particle irradiation approximately 100 - 200 track spots were analyzed.

4.4.4 Characterisation by STED microscopy

Irradiated FNTDs (gray-shaded in Table 4.4.1) were read out by a home-built STED microscopy [45]. Due to circularly-polarized excitation laser light a corresponding mounting of the FNTD to maximize the fluorescence intensity signal could be neglected. The read-out depth was adjusted to approximately $10\,\mu$m (except C-12, $224.81\,\text{MeV}\,\text{u}^{-1}$: $40\,\mu$m) measured from the detector surface.
In a first step, the correlation between the FWHM Δx_{meas} (and hence the resolution, Eq. 2.10) of the track spots (H-1, $49.37\,\text{MeV}\,\text{u}^{-1}$ and C-12, $224.81\,\text{MeV}\,\text{u}^{-1}$) and the intensity I of the STED laser was investigated. The parameter Δx_{meas} was obtained by

a 2D Gaussian fit (built-in function in the microscope control software) of the STED raw data.
The data points of Δx_{meas} were fitted by

$$\Delta x_{\mathrm{meas}} = \sqrt{\Delta x_{\mathrm{act}}^2 + \Delta x_{\mathrm{PSF}}^2} \tag{4.8}$$

$$\Delta x_{\mathrm{PSF}} = \beta \frac{\lambda}{2n \sin\alpha \sqrt{1 + I/I_S}} \tag{4.9}$$

with the fit parameters Δx_{act} the actual feature size, a scaling factor β, and the saturation intensity I_S (section 2.5.2) [45]. Equation 4.8 describes the recorded intensity profile. It is a convolution of the actual Gaussian-shaped intensity profile of FWHM Δx_{act} with a Gaussian-shaped focal spot of FWHM Δx_{PSF}.
In a second step, the extracted PSF (Δx_{PSF}) was convoluted with the RDD in Al_2O_3 using the Scholz model (Fig. 2.4.1C) [24, 28]. The FWHM Δx_{meas} was compared with the FWHM of a track spot obtained by the convolution in order to draw conclusions on the radius of the central plateau in the RDD.
For irradiated FNTDs with corresponding doses $> 50\,\mathrm{Gy}$, photon-dose response correction was applied, to account for the saturation in color center transformation (Fig. A1). Below 50 Gy linear scaling was assumed.
All corresponding confocal images were recorded with the STED microscopy in confocal mode by switching off the STED laser.

4.5 Probing single cell fate after therapeutic ion irradiation

The focus in this study was on the functional read-out of the Cell-Fit-HD. Apoptotic cell death kinetics indicated by caspase-3/7 activity in the cell was related to the physical energy deposition in the nucleus as well as to biological constraints (cell density). For this purpose the survival time of each cell and the corresponding apoptotic index, defined as the number of caspase-3/7 positive objects divided by the total number of observed cells were determined.

4.5.1 Creating Cell-Fit-HD

FNTDs were placed in single wells of a 24 multi-well plate and the polished surface was covered with A431 cells (plating density of $10^5\,\mathrm{ml}^{-1}$, 0.5 ml per well) as described in section 4.1.1. The Cell-Fit-HDs were kept in humidified atmosphere for 24 h. After 24 h the cell culture medium was exchanged.

4.5.2 Irradiation and apoptosis assay

Cell-Fit-HDs were irradiated perpendicularly ($\theta = 0°$) with carbon ions (of initial $270.55\,\mathrm{MeV\,u}^{-1}$). The biological compartment was placed in the rising flank of the Bragg-peak of corresponding $35.95\,\mathrm{MeV\,u}^{-1}$ ($\mathrm{r_{H_2O}}$= 14.09 cm, dose in water= 0.94 Gy [24]). The irradiation setup is described in section 4.1.3. The fluence was adjusted to $10^7\,\mathrm{cm}^{-2}$ and the irradiation field was limited to 8 x 8 cm^2. 11.6 cm of PMMA ($\mathrm{r_{H_2O}}$ = 13.51 cm) was placed as stopping material in front of the Cell-Fit-HD (Fig. 4.1.1).
Immediately after irradiation, actual irradiated and sham irradiated (i.e. positive control) Cell-Fit-HDs were placed in a single glass bottom culture dish and stained with DEVD-NucView488/ Draq5 (section 3.11.1).

4.5.3 Time-lapse imaging

The Cell-Fit-HDs were imaged sequentially using the CLSM (section 4.1.4) with the parameters listed in Table 4.2.1. The irradiated Cell-Fit-HD and the positive control were placed in a single glass bottom culture dish (filled with culture medium). The hybrid detectors were mounted accordingly to maximize the fluorescence intensity signal (section 3.2).
Live-imaging started 1 h after irradiation. Initially, the physical compartment was read out. A single imaging plane at 30 μm depth (according to section 4.4.2) with respect to the FNTD surface was acquired in a high cell density area (hD area). Time series of

the hD area and a single area in the positive control (pC) were subsequently recorded. The total lapse of time was approximately 19 h with an interval Δt of approximately 45 min, i.e. the interval between the acquisition starts of two consecutive time points (in total 25 time points). The actual irradiation was defined as time point 0. Within a time point, the hD area and the pC were imaged sequentially. In the last time point additional position in the biological compartment of less cell density (lD area) was imaged including the corresponding imaging plane at 30 μm depth in the physical compartment. For this position, the acquisition parameters remained the same (except for the recorded image stack comprising 9 imaging planes).
Imaging was done under humidified atmosphere (37°C, 5% CO_2). The incubation chamber of the microscope was started to heat 4 h prior to the imaging.

4.5.4 Image processing

Physical compartment In a first step, the particle tracker (radius= 3 pixels, cut-off= 0, percentile= 2%) was applied on the raw image data to identify the positions of the ion track centers. In a second step, the background subtractor with a sliding window of length 16 pixels (according to section 4.4.3) was applied on the raw image data. The corrected fluorescence signal was converted into the actual count rate (section 3.3.3). To define an ROI in the corrected imaging plane, each track spot center was masked with a rectangle of dimensions $\Delta x \cdot \Delta y = 5 \cdot 5$ pixels. The maximum intensity was assessed in each ROI. The corresponding coordinates of the track spot center (floating point numbers) were rounded to integers for further image processing purposes.

Biological compartment Image segmentation of the maximum intensity z projection of the Draq5 channel (time point 1) was carried out to identify all cell nuclei. Overlapping cells hindered a clear separation by automatic segmentation (algorithm is displayed in section 3.15). Semi-automatic processing. i.e. defining the nucleus margin manually, was therefore carried out to allow an isolation of each nucleus (in total five different binary masks). The binary masks (0: background, 1: nucleus area) were projected onto the maximum intensity z projection of the NucView488 (i.e. caspase-3/7) channel at each time point. Depending on the position of the cell nucleus in depth only the corresponding imaging planes of the NucView488 channel were used for the maximum intensity z projection.

4.5.5 Ion hit statistics

Instead of track extrapolation (section 4.2) and intersection with the nucleus body a simpler approach was used. The ion track center coordinates were projected onto the coordinate system of the biological compartment. This should however approximate the

actual nuclei hit distribution by ions with $\theta \neq 0°$ well. Using high fluences ($10^7\,\mathrm{cm}^{-2}$) actual false-positive and false-negative nucleus traversals with $\theta \neq 0°$ should be at equilibrium.
The local LET was defined as the mean LET per nucleus. It is the arithmetic mean of all occurring LET values within a nucleus area. The 2D nucleus area was defined by the corresponding binary mask. To assess the LET of the penetrating ions registered, the mean maximum count rate of the track spots per nucleus was calculated and converted into the LET_∞ (Eq. 6.1). The parameter LET_∞ is abbreviated by LET. The local fluence was defined as the number of direct nuclei hits per nucleus area. The local dose (i.e dose per nucleus) was calculated using Equation 2.4. The absolute value of LET_∞ is equivalent to the stopping power S. For the density, water was assumed. The dose was assumed to be constant within a nucleus.

4.5.6 Survival analysis

According to the median of the assessed quantities parametrizing the energy deposition in the nucleus, the cells in the hD area were grouped. The following quantities were considered: number of hits per nucleus, LET, fluence as well as dose in the nucleus. According to the mean LET per nucleus and using the histogram-based threshold (Fig. 5.5.3A) all cells were categorized whether the nucleus was primarily hit by carbon ions or lighter fragments. The apoptotic index was computed for each group and for each time point. If the caspase-3/7 signal of an individual cell exceeded a certain threshold it was defined to be apoptotic.
A log-rank test was performed to compare the survival distributions over time for the sub-sets of a group (Kaplan Meier curves). Survival was defined as (1 - apoptotic index). Cells, still non-apoptotic in the last imaging time point were censored. The null hypothesis was defined as *"No difference between the survival curves of the sub-sets, i.e. the sub-sets exhibit the same probability to undergo radiation-induced apoptosis."*. A 5% level of significance was assumed. For the survival analysis all cells were assumed to be non-apoptotic (apoptotic index= 0) at the time of irradiation (time point 0).

5 Results

5.1 Engineering Cell-Fit-HD

5.1.1 Creating the hybrid composite

The FNTD provides a biocompatible surface. By varying plating density, fibronectin concentration as well as incubation time under humidified atmosphere all human and murine cell lines were able to form a viable and stable cell layer (i.e. the biological compartment) on the polished surface of an autoclaved FNTD, the physical compartment. Gliomas (SMA-560) and U87 cells formed networks of overlapping cells. Epithelial tumor cell lines (A431, PC3, A549) formed tightly-packed monolayers (Fig. 5.1.1A,B). A detailed description of optimizing cell-coating and quantifying cell proliferation kinetics of the hybrid composite can be found in B: *Results, FNTD crystals are biocompatible* [9].
Concerning the morphology all cells were spread and flat. They exhibited the same shape as grown on standard cell culture treated surfaces under controlled conditions (incubator, humidified atmosphere).

5.1.2 Probing viability of the biological compartment

The FNTD surface was found to be compatible with all fluorescence-based stainings tested in the biological compartment comprising A549 cells [9]. The dyes did not accumulate at the FNTD surface neither by live cell labeling (Calcein AM, CM-DiI) nor by immunofluorescence staining (Glut1, HOECHST).
High levels of fluorescence signal under Calcein AM labeling as well as the round shape of the cell nuclei indicated good cell viability (Fig. 5.1.1E). The cytoplasm comprised multilamellar bodies with high esterase activity (bright spots) which correlate to an active metabolism. CM-DiI used to achieve a better contrast between the biological and physical compartment, suggested an exocytotic activity of the cells (Fig. 5.1.1C,D). Small bodies with high fluorescent signal were present in the intercellular space (Fig. 5.1.1D).
Immunohistochemical analysis using HOECHST as nuclear stain revealed a high bulk cell density of approximately $6.3 \cdot 10^5\,\mathrm{cm}^{-2}$ (Fig. 5.1.1F). Glut1 staining displayed a sharply bounded network of plasma membranes (Fig. 5.1.2). Together with CM-DiI,

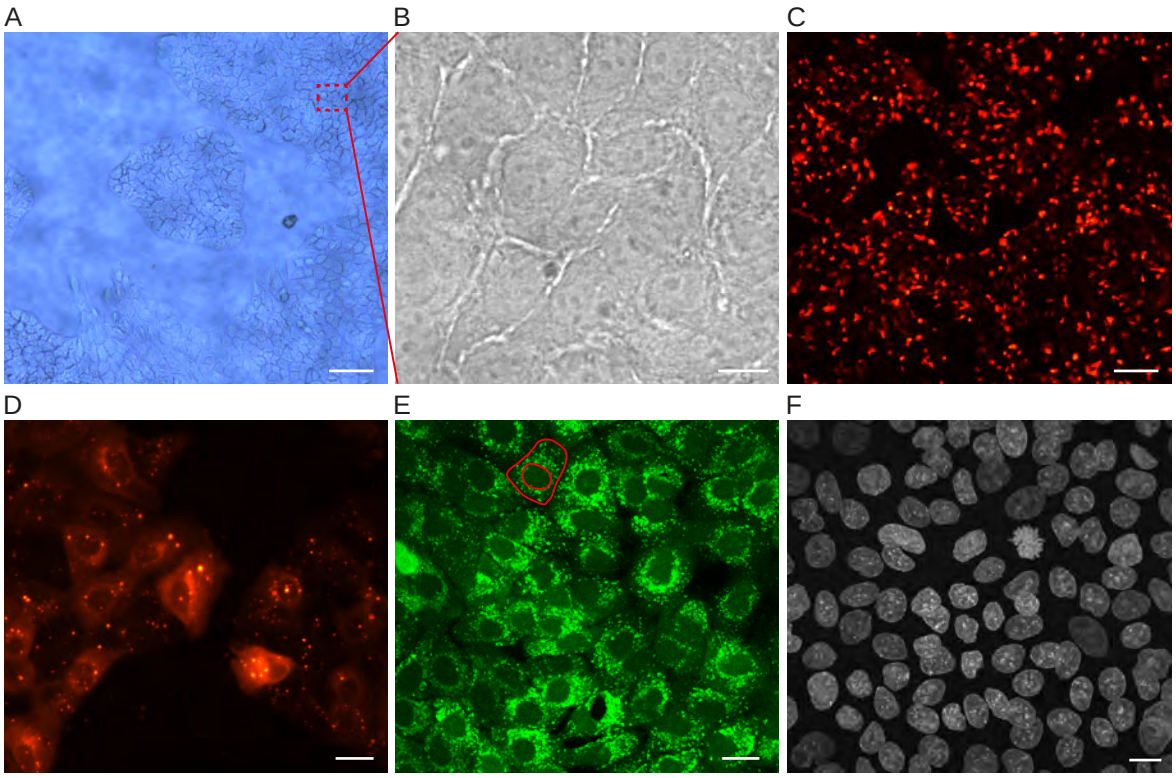

Figure 5.1.1: A549 cell coating. (A) A549 cells starting to form a confluent monolayer. An island formation with branching cells is visible. Scale bar, approximately 200 μm. (B) Magnified section of a confluent monolayer. The cells are tightly packed. It is difficult to contrast cells from the transparent FNTD with light microscopy. Scale bar, approximately 200 μm. (C) CM-DiI labeled and proliferating cells forming a confluent monolayer. Scale bar, approximately 200 μm. (D) Section of CM-DiI labeled monolayer. Cytoplasmic granules exhibit a strong fluorescent signal. Scale bar, approximately 20 μm. (E) Cell layer labeled with Calcein AM to test cell viability. The outer red line indicates the cell membrane. The cell nucleus is defined by the inner red line. A strong perinuclear fluorescent signal with many bright spots (cytoplasmic organelles) and round nuclei indicate good cell viability. Scale bar, 20 μm. (F) Immunofluorescent labeling of cell nuclei by HOECHST 33342 stain. A uniform monolayer of proliferating cells is visible. Scale bar, 10 μm. Images (A), (C), and (D) were obtained by wide field microscopy whereas images (B, E, and F) were obtained in confocal mode. Images (A)-(E) show live cell stainings. In (F) cells are fixed with 4% PFA. Taken from [9].

Glut1 demonstrated that A549 cells maintained their tight epithelial cell-cell contact when cultured on the FNTD surface.

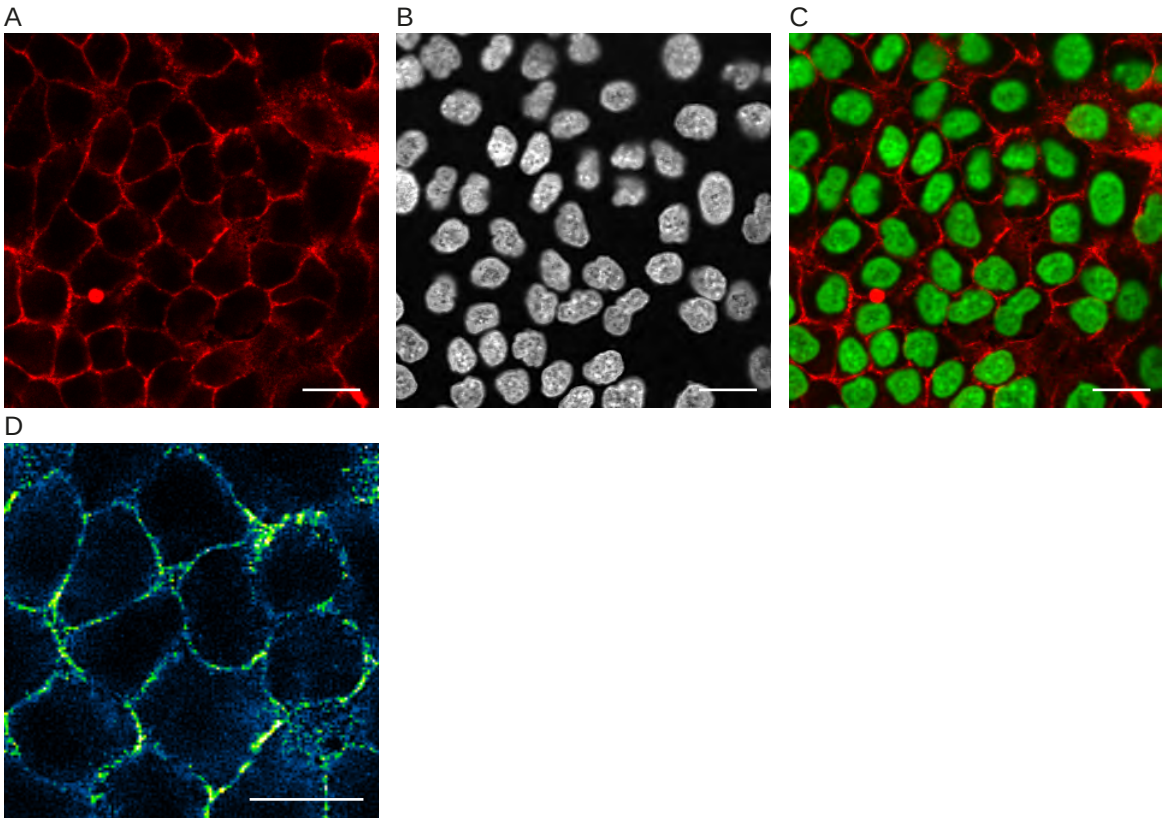

Figure 5.1.2: Glut1/ HOECHST dual staining of A549 cell layer. (A) Glucose transporter Glut1 staining visualizes the A549 cell membrane. Glut1 is mainly accumulated at the membrane. The diffuse cytoplasmic signal may arise from permeabilisation during immunofluorescence staining. (B) HOECHST staining as nuclear counterstain. (C) Merging of Glut1 and HOECHST images. A549 cells form a tightly packed monolayer with strong cell-cell adhesion. (D) A section of (A) with different color coding (blue-green-yellow) is shown. The yellow bright spots indicate a strong accumulation of Glut1 at the membrane. Scale bars, 20 μm. (A)-(D) were obtained by confocal fluorescence microscopy. Taken from [9].

5.1.3 Therapeutic particle irradiation

Mounting each Cell-Fit-HD with agarose in a single well of a multiwell plate, allowed for an easy handling in the irradiation setup (Fig. 4.1.1). By filling the well with culture medium enabled the cells to stay alive during irradiation. The pH-indicator in the culture medium indicated a stable CO_2 level (a drop is potentially dangerous). The carbon ion irradiation of the hybrid detector of dimensions 4 x 8 x 0.5 mm^3 with a fluence of $1.5 \cdot 10^6\,cm^{-2}$ lasted less than 10 s.

5.1.4 Sequential read-out of Cell-Fit-HD

The biological, stained for HOECHST and the physical compartment could be imaged successfully in two consecutive steps by the very same CLSM. No post-irradiation chemical processing of the FNTD or a removal of the cell layer was necessary. Standard immunofluorescence staining could be employed to co-register and to correlate cell biology and ion track information (Fig. 5.1.3). It was possible to achieve a relatively fast acquisition of the physical compartment (frame-acquisition time of 14.9 s by adjusting the scan and detection parameters, Table 4.2.1), crucial for live imaging without forfeiting much signal-to-noise ratio (SNR).
When reading-out the physical prior to the biological compartment the quality of ion track information was not compromised in Cell-Fit-HD as compared to the FNTD alone. However when imaging the biological prior to physical compartment an increase in the detector background signal by the light cone of the 405 nm laser used for HOECHST imaging occurred. Neither the creation of the hybrid composite under humidified atmosphere nor additional staining procedures affected the signal quality of the sole FNTD read-out. Technical limitations by the CLSM itself, e.g. working distance of the objective did not interfere the hybrid detector read-out.

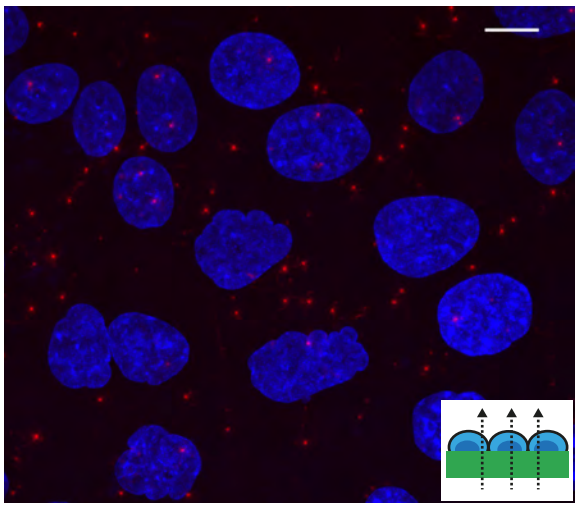

Figure 5.1.3: Spatial correlation between carbon ion tracks and A549 cell layer achieved by the sequential read-out. A superposition of a maximum intensity z-projection (cell nuclei are labeled with HOECHST, blue) with an image of the acquired FNTD image stack is displayed. Compared to the diameter of a cell nucleus ($\approx 10\,\mu$m) track spots (red spots) have a diameter of less than $1\,\mu$m. The small trajectories branching from the track spots are tracks of secondary electrons released in Al_2O_3:C,Mg. Insert: The surface of the Cell-Fit-HD was set perpendicular to the incident carbon ion beam. Scale bar, $10\,\mu$m. Taken from [9].

5.2 Ion track reconstruction in 3D

5.2.1 Intensity profile of a track spot

Under perpendicular irradiation ($\theta = 0°$) the intensity profile of the track spots is almost radial symmetric (Fig. 5.2.1A). The track core exhibits a steep gradient. Trajectories of scattered δ electrons having a broad angular distribution emerge from it. Their Bragg peaks, i.e. local intensity maxima at their track ends, are clearly visible.
Under angular irradiation ($\theta = 60°$) the intensity profile of the track spots is ellipsoidal and extended along beam direction (Fig. 5.2.1B). It has tattered edges and also branching δ electron trajectories of broad angular distribution. The complex profile exhibits an intensity rise with a global maximum, most probably accounting for the angular track core. On average, an elongated track spot has a size of approximately 7 x 0.5 μm^2 – compared to the diameter of 0.9 μm of a symmetrical track spot.
Under perpendicular and angular irradiations the positions of the intensity-weighted track spot centers detected by applying a global threshold (*iw centroid, A*) and dynamic thresholding (*rel thres, B*) are nearly identical (Inserts, Fig. 5.2.1). Larger deviations from these positions occur for identifying the absolute intensity maximum (*abs max, C*). The spatial mismatch is much more pronounced under angular than under perpendicular irradiation.

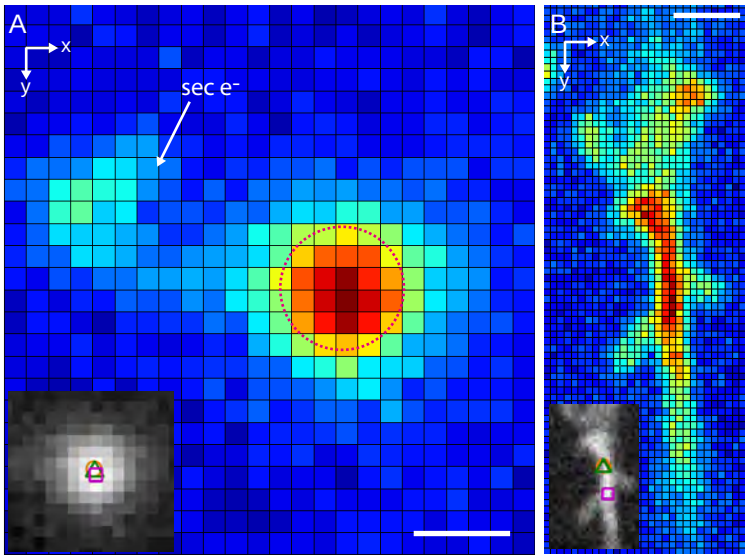

Figure 5.2.1: Dependency of the FNTD read-out signal on the irradiation angle. Intensity profile of the read-out signal after (A) perpendicular ($\theta = 0°$) and (B) angular irradiation ($\theta = 60°$). The track core (masked by the point spread function of the CLSM) is indicated by the red dashed circle. In both cases δ electron trajectories are sprouting from the symmetrical and ellipsoidal track spot. Inserts: The track spot centers detected by identifying the intensity-weighted centroid applying a manually defined threshold (ocher circle), by identifying the intensity-weighted centroid applying dynamic thresholding (green triangle) and the absolute maximum (magenta rectangle) and do not coincide. Scale bars, 0.5 μm (A) and 1 μm (B). Taken from [10].

5.2.2 Residuals of the fit

A detailed description of the residuals gained from LRA can be found in D: *Results, Residuals of the fit* [10]. Generally, the mean absolute residuals (in an initial step the absolute residuals corresponding to a single fit were averaged) perpendicular to beam direction (x) are smaller than along beam direction (y) for all identification approaches and for all Δz (the distance in z between two neighboring track spots, Fig. 5.2.2). Identification approaches A (*iw centroid*) and B (*rel thres*) result in similar and smaller residuals than approach C (*abs max*).
Under angular irradiation (Fig. 5.2.2A), the residuals fluctuate around 0.10 μm in x and around 0.58 μm in y for all Δz (A and B) and increase under C (x $\approx$ 0.12 μm, y $\approx$ 0.68 μm). Standard error of the mean (SEM) in x ($\leq$ 0.02 μm) and in y ($\approx$ 0.10 μm) approximately equal for all Δz and for all identification approaches.
Under perpendicular irradiation the residuals in x and y approaches. The wide gap between x and y disappears (Fig. 5.2.2B). All residuals are smaller than 0.05 μm ($\leq$ 0.04 μm for A and B, $\Delta z = 3, 6\,\mu$m) with SEM $\leq$ 0.01 μm.

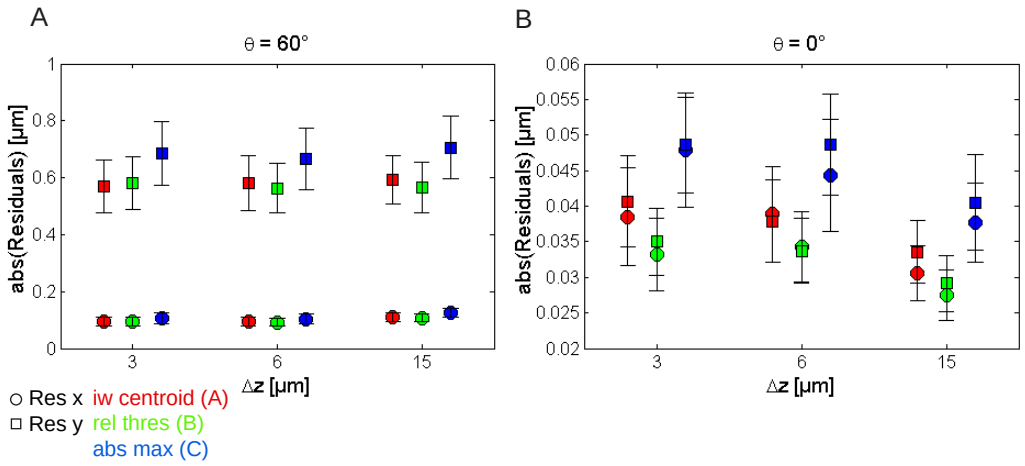

Figure 5.2.2: Residuals in ion track reconstruction. Mean absolute residuals in x (circles) and in y (solids) resulting from different fitting procedures. The distance Δz between two consecutive track spots was varied and different approaches to detect the track spot centers were used (red: intensity-weighted centroid, green: dynamic thresholding, blue: absolute maximum). The error bars are the SEM. (A) Angular irradiation, $\theta = 60°$. (B) Perpendicular irradiation, $\theta = 0°$. Taken from [10].

5.2.3 Accuracy of ion track reconstruction in 3D

The limits of accuracy shall be given here. A detailed analysis can be found in D: *Results, Accuracy of ion track reconstruction in 3D* [10].
For angular irradiation the mean values $\theta = 59.03°$ and $\phi = 84.68°$ differ of maximum 0.07° and 0.01° respectively for all LRA (D: Table 1). The corresponding error $\Delta\theta$ lies between 0.89° (A, $\Delta z = 3\,\mu$m) and 3.45° (C, $\Delta z = 15\,\mu$m, D: Fig. 5a,b). The error $\Delta\phi$

$\leq 0.2°$ (except $\Delta z = 15\,\mu$m). For $\Delta z < 15\,\mu$m, mean prediction interval $PI_x \leq 0.4\,\mu$m and is increasing to $0.77\,\mu$m (C, $\Delta z = 15\,\mu$m, D: Fig. 6a,b). Mean PI_y lies between $1.72\,\mu$m (A, $\Delta z = 3\,\mu$m) and $4.58\,\mu$m (C, $\Delta z = 15\,\mu$m).
For perpendicular irradiation $\theta \approx 1.22°$ differs less than 0.02° and $\phi \in [45°; 46°]$ (D: Table 2). Whereas $\Delta\theta$ lies between 0.06° (B, $\Delta z = 3\,\mu$m) and 0.26° (C, $\Delta z = 15\,\mu$m), $\Delta\phi$ covers a broad range – between 1.53° and 4.77° (D: Fig. 5c,d). The mean PIs in x and in y are generally much smaller than $0.3\,\mu$m (D: Fig. 6c,d).
At the transition to $\Delta z = 15\,\mu$m ($\theta = 0°$, 60°), both the distributions of $\Delta\theta$ and $\Delta\phi$, indicated by their standard deviation (SD), and their mean values show a steep rise under A-C (D: Fig. 5). The mean PIs behave similarly (D: Fig. 6).

5.3 DNA damage response to particle irradiation

5.3.1 Ion hit statistics

In Figure 5.3.1 an example of co-detection and co-registration of track information from the physical and cellular response from the biological compartment is shown. The biological compartment comprised a confluent and tightly-packed monolayer of A549 cells. The total imaging field (total area of $0.073\,\text{mm}^2$) comprised approximately 515 cells with $A_c = 158\,\mu\text{m}^2$ and $A_n = 83\,\mu\text{m}^2$.
The carbon ion beam was parametrized by the actual fluence Φ of $5.62 \cdot 10^5\,\text{cm}^{-2}$ (Eg. 3.3) and by a mean ion flight direction of $(\theta, \phi)_{ion}$= (58.98°, 84.69°). By evaluating the intensity (converted into η_{actual}) of the track spots, the ion traversals could be categorized into two populations: primary carbon ions ($\approx$ 33%) and lighter fragments ($\approx$ 67%), most probably protons (Fig. 5.3.3A). 30% of the fragments showed large angular scattering, i.e. were deflected more than 10° away from the mean ϕ_{ion}.
The total number of nuclei hits in the total imaging field by ions was estimated to be 242 (on average 0.467 total hits per nucleus). 103 hits by carbon ions and 139 by fragments with the following hit distribution: 315 nuclei were not hit (322 according to an ideal Poisson distribution), 159 nuclei were hit once (151), 40 nuclei were hit twice (36) and 1 nucleus was hit three times (6). The total number of cellular hits was calculated to be 461.
In sum 17 RIF sequences could be correlated to single ion tracks, i.e. 4% of all cellular hits caused a RIF sequence. In four cases two RIF sequences were located in the same nucleus. The probability (4/17) of having two sequences in a single nucleus coincides well with the probability (40/242) of two hits per nucleus.

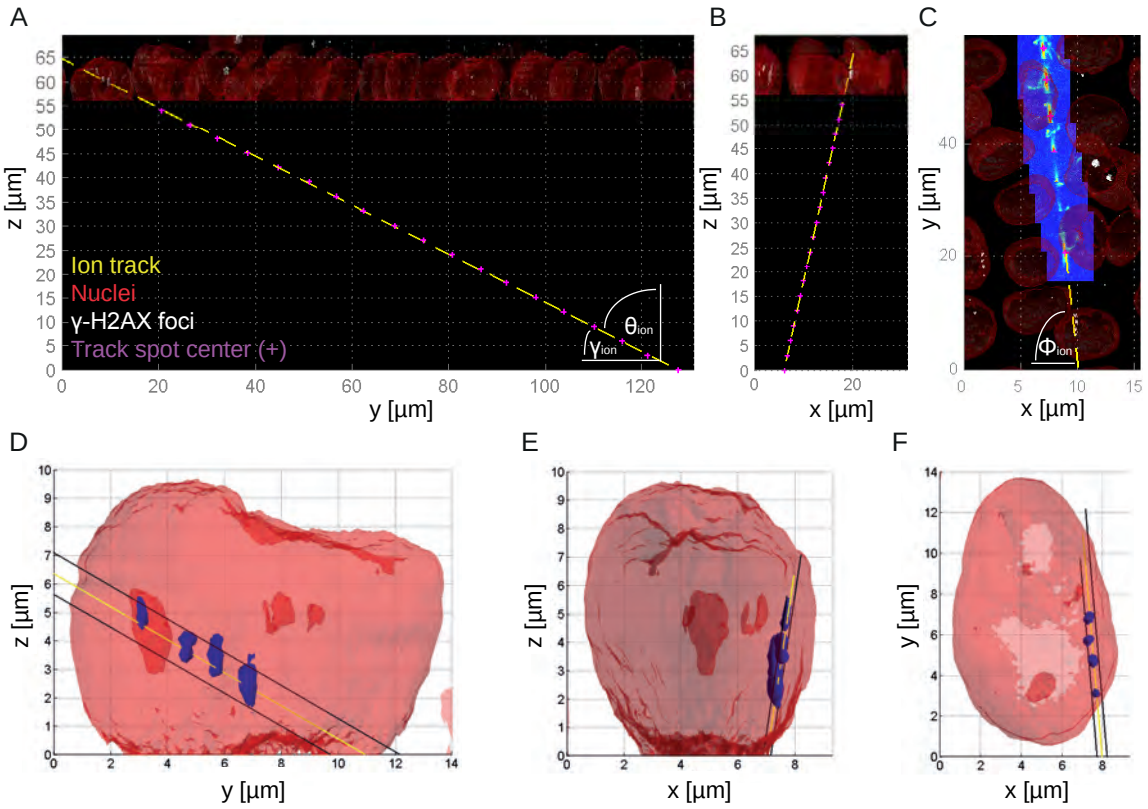

Figure 5.3.1: Spatial correlation gained on a subcellular scale. Projections (yz, xz, xy) of a reconstructed ion track and its extrapolation into the cellular compartment. (A-C) The ion track parametrized by θ_{ion}, γ_{ion} and ϕ_{ion}, is indicated by the yellow dashed line. The magenta crosses indicate the positions of the detected track spot centers in the corresponding imaging plane of the FNTD image stack. Cell nuclei and γ-H2AX foci (RIF) are depicted in red and white, respectively. (C) A section of the xy projection including subvolumes of the detector imaging planes with the ellipsoidal track spots is depicted. (D-F) Spatial correlation between the ion track (yellow line), cell nucleus (red), and γ-H2AX foci (blue). The black lines indicate the 95% prediction intervals; only the upper right and the lower left boundaries are shown. Taken from [11].

5.3.2 Residuals and dynamics of the RIF sequence

The mean residuals between the centroids of the scattered RIFs and the most-likely ion tracks in x and y were 1.09 μm ± 0.23 μm and -1.72 μm ± 0.82 μm (SD) respectively (Fig. 5.3.2). The mean slope of the reconstructed tracks γ_{ion}= 31.02°± 0.80°and the mean polar angle ϕ_{ion} (84.69°± 1.13°) coincided well with the mean slope γ_{RIF}= 33.40 °± 5.94°and the mean ϕ_{RIF}= 86.46°± 3.71°of the scattered RIF-sequences (Fig. 5.3.1D-F). Generally there was a trend for the tracks to be located above (i.e. in positive z) the RIF sequences (indicated by negative residuals in y).
The mean perpendicular between the ion track and the RIF was 1.58 μm ± 0.69 μm (E: Fig. 4B). The mean FOP distances clustering in $[2; 3.3\,\mu\text{m}]$ are correlated to the corresponding track spot intensities accumulating at [400; 800MHz] (Fig. 5.3.3B). The distribution of all FOP distances exhibits multiples of 1 μm (Insert, Fig. 5.3.3B).

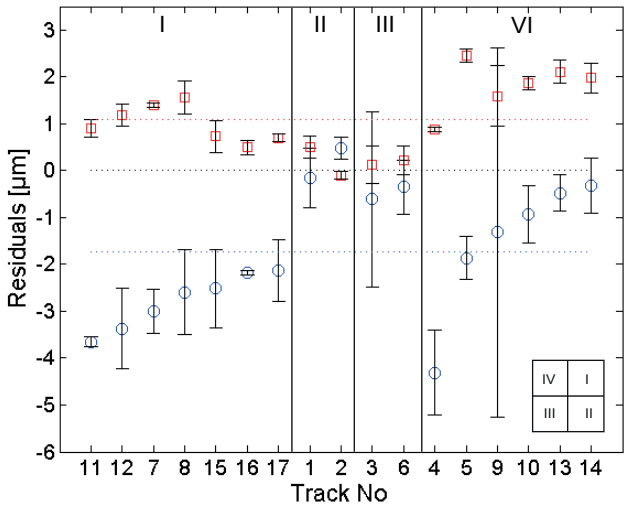

Figure 5.3.2: Mean lateral residuals between the radiation-induced γ-H2AX foci (RIFs) and the corresponding ion tracks. In an initial step the residuals corresponding to a single ion track were averaged. The overall mean in x (solids) is 1.09 μm ± 0.23 μm (SD, red dotted line) and in y (circles) is -1.72 μm ± 0.82 μm (blue dotted line). Inset: The residuals were sorted with respect to the quadrant of the tile scan. Taken from [11].

5.4 Resolving therapeutic particle spectrum

5.4.1 Direct measurement: $\hat{\eta}$ and FWHM

A masking of the track spots with a disc of diameter 15 pixels for all particle types and energies seemed to be most suitable. The ROI comprised the entire track spot. The maximum count rate $\hat{\eta}_{actual}$ is increasing with rising LET. It follows an approximately exponential function (Fig. 5.4.1) [8, 38]. The increase in the therapeutic relevant LET range $[0; 100\text{keV}\,\mu\text{m}^{-1}]$ could be approximated by a line applying simple LRA (Insert,

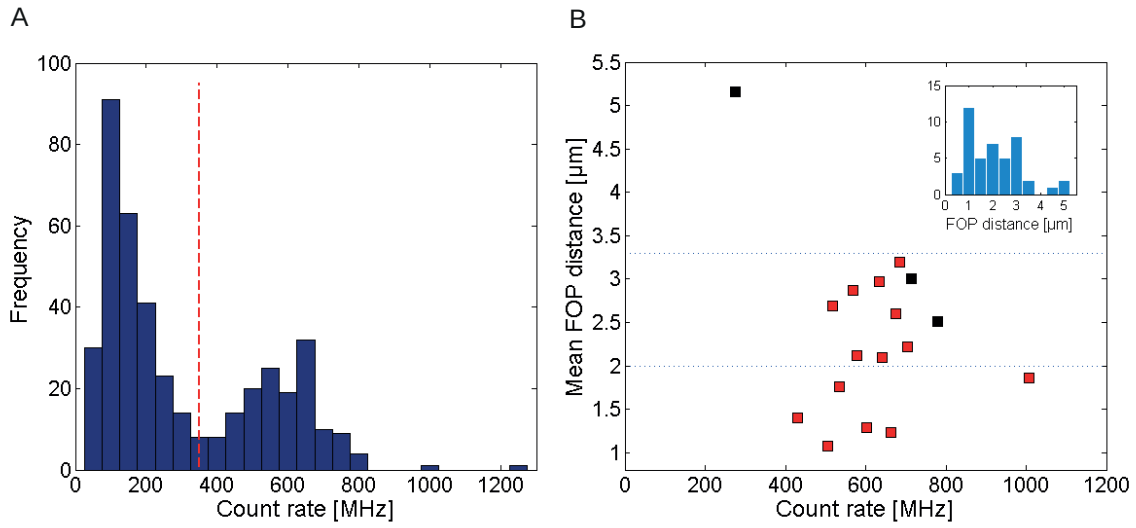

Figure 5.3.3: Correlation between the intensities of the track spots and the mean distance between neighboring feet of the perpendicular (FOPs). (A) Distribution of the summed track spot intensities, converted into count rate. According to the histogram the threshold was set to 350 MHz (red dashed line) to distinguish between primary particles and lighter fragments. (B) The mean FOP distances corresponding to carbon ion tracks are clustered in the interval $[2; 3.3\,\mu\text{m}]$. The track-spot intensities represented by the black solids are in fact smaller. Two very close neighboring tracks partly intersecting hinder a clear separation by the track spot intensity analysis. The distances were calculated only between FOPs located in the same cell. Inset: The distribution of all FOP distances exhibits accumulation around $1\,\mu$m, $2\,\mu$m, and $3\,\mu$m. Taken from [11].

Fig. 5.4.1A).

Figure 5.4.2 displays the correlation between the FWHM and r_{max} (maximum secondary electron range). There seems to be a linear trend for track spots with a FWHM greater than $0.5\,\mu$m. Concerning Fe-56 and Xe-131, the FWHM seems to rise with increasing particle energy. Concerning H-1 and C-12 the FWHMs seem to be identical ($\approx 500\,$nm) for all corresponding particle energies.

5.4.2 2D Gaussian fit

The distribution of $\eta_{detected}$ was fitted by a 2D Gaussian function to get an estimation of the net count rate. For the track spot masking the following disc radii seemed to be most suitable: 10 pixels (H-1 and C-12), 15 pixels (Mg-24 and S-32) and 20 pixels (Fe-56, Kr-84 and Xe-131). These disc radii ensured a suitable trade-off between sufficient background signal in the ROI and not to exclude too many track spots by overlapping ROIs. Except for Mg-24 and S-32 the mean Gaussian peak amplitude $\hat{A}$ is rising with increasing atomic number of the incident ions (Fig. 5.4.3A) [8]. Within a certain particle type, there is a general trend for $\hat{A}$ to decrease with increasing particle energy and hence decreasing LET. The background pedestal B follows the same tendency: it is increasing with rising atomic number (and rising disc mask radius) and declining with

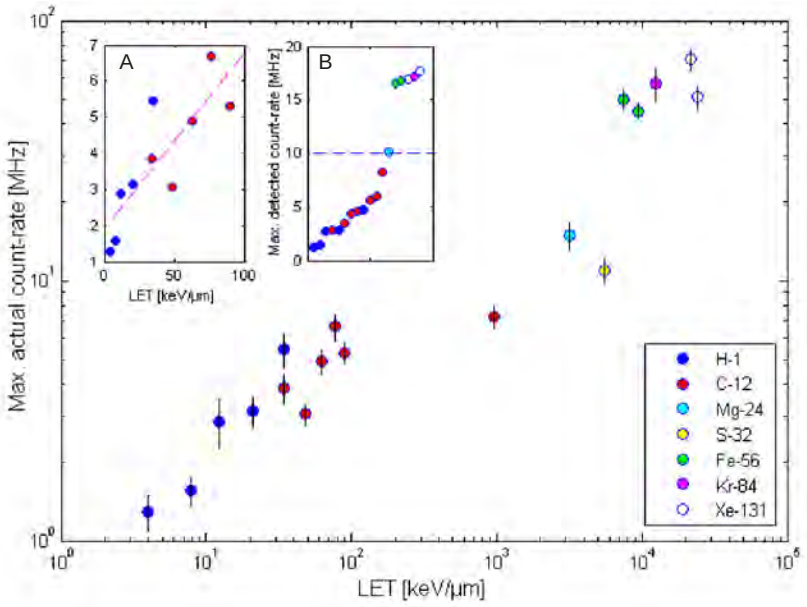

Figure 5.4.1: Correlation between the mean maximum count rate $\hat{\eta}_{actual}$ of a track spot and the LET of the incident particle. The error bars show the SD. The disc radius for the track-spot masking is 15 pixels for all particle types and energies. Inserts: (A) fitting of H-1 and C-12 count-rates (except C-12 4 MeV u^{-1}) by a straight line. (B) Mean maximum detected count rates $\hat{\eta}_{detected}$ sorted in ascending order. Above 10 MHz saturation effects occur. Taken from [8].

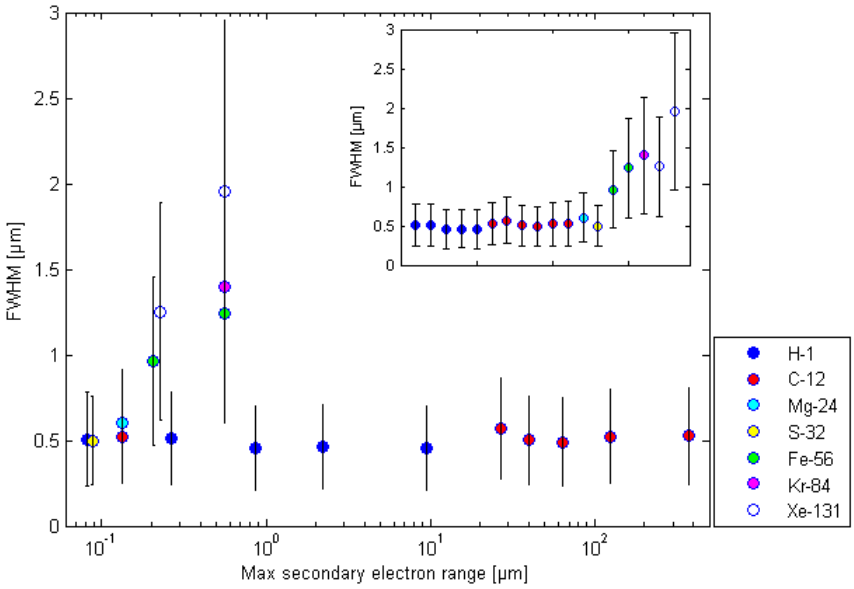

Figure 5.4.2: Correlation between the mean FWHM of a track spot (η_{detected}) and the maximum secondary electron range (r_{max}). For a certain particle type r_{max} is increasing with rising particle energy. The error bars show the SD. The disc radius for the track-spot masking is 15 pixels for all particle types and energies. There seems to be a linear relationship for track spots with a FWHM $> 0.5\,\mu$m. Insert: mean FWHM sorted in ascending order. Taken from [8].

increasing energy of a certain particle type (Insert, Fig. 5.4.3A).
For all ions lighter than Fe-56, σ hardly varies (Fig. 5.4.3B). There is yet a significant increase for particles heavier than S-32.
Except for heavier ions (in particular Xe-131) the parameters gained by direct measurements and by the 2D Gaussian fit coincide (Fig. 5.4.3).

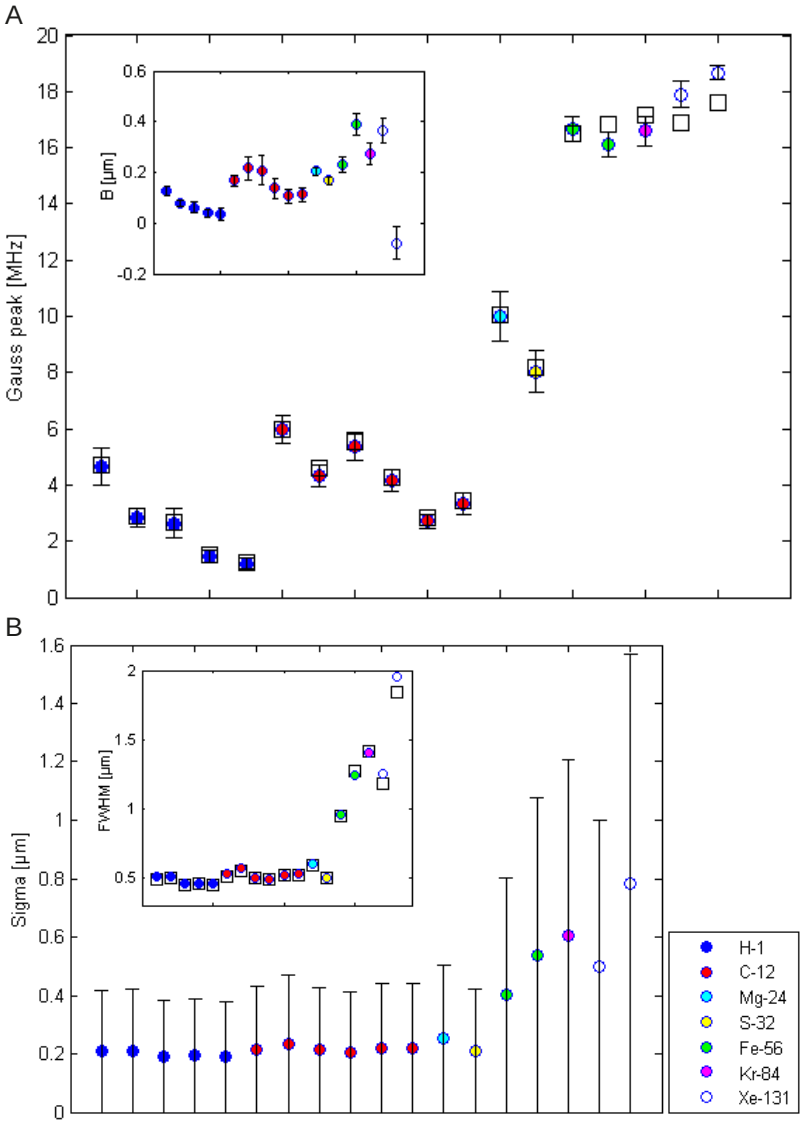

Figure 5.4.3: Track spots ($\eta_{detected}$) parametrized by a 2D Gaussian fit. Values of the mean Gaussian peak amplitude $\hat{A}$ and mean σ are sorted in ascending order with respect to the atomic number and energy of the incident particle. (A) The value of $\hat{A}$ is declining with increasing energy within a particle type. Insert: the background B is rising with increasing atomic number. (B) Mean σ is nearly constant for ions lighter than Fe-56. Insert: The corresponding mean FWHM gained by the fit nearly coincides (except Xe-131) with the mean FWHM gained by track spot characterisation. Taken from [8].

5.4.3 Characterisation by STED microscopy

A read-out of the irradiated FNTDs by STED microscopy is principally possible (Fig. 5.4.4). Generally the FWHM (Δx_{meas}) of a track spot could be reduced by a factor of approximately two compared to the confocal imaging data (Fig. 5.4.5). Compared to the confocal read-out, an increase in background and a decrease of the foreground signal (colorbars in Fig. 5.4.4) under STED occurred. De-excitation of transformed color centers at very high STED laser intensities was also possible .
Whereas the intensity profiles of protons and carbon ions seems to be peaked, the profile for xenon seems to exhibit a plateau (Fig. 5.4.4G-I). The resolvable carbon ion beam fluence ($> 10^8\,\mathrm{cm}^{-2}$) could be increased by a factor of at least two compared to the maximum resolvable fluence of $5 \cdot 10^7\,\mathrm{cm}^{-2}$ by confocal read-out according to [7] (Fig. 5.4.6).
The FWHM (Δx_{meas}) of the investigated track spots (C-12, $152.05\,\mathrm{MeV\,u}^{-1}$ and H-1, 49.37 MeV) is decreasing – and hence the resolution is increasing – with increasing STED pulse intensity (personal communication with Henrich, M.). For C-12 and H-1 it is approaching to 147 nm and 110 nm, respectively [45]. The effective STED PSF had a FWHM (Δx_{PSF}) of approximately 70 nm.

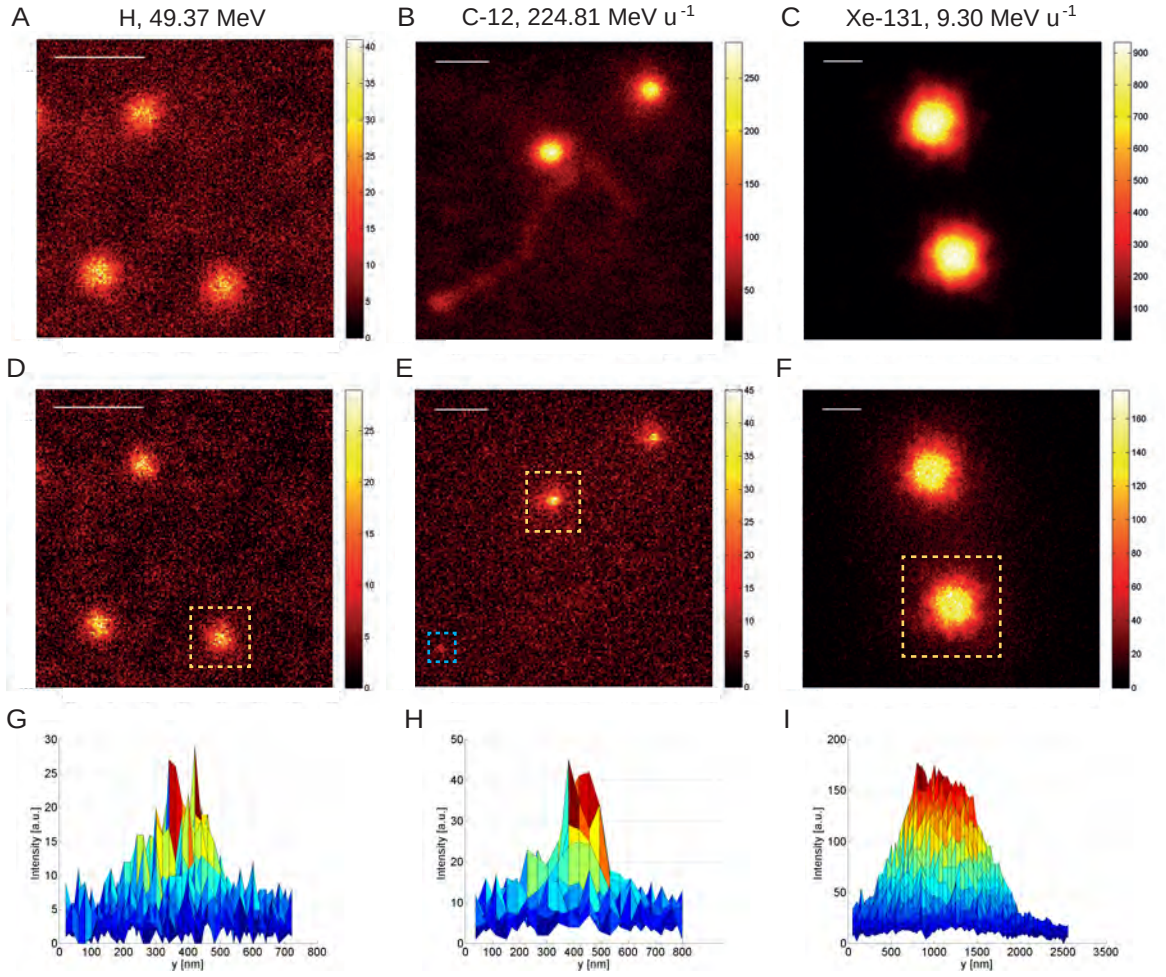

Figure 5.4.4: Exemplary track spots gained by confocal and STED read-out. (A-C) Confocal and (D-F) STED read-out. A reduction of the FWHM and the intensity values under STED compared to the confocal data is clearly visible. A secondary electron trajectory including its track end (indicated by the blue rectangle) is visible (B,E). (G-H) Plots of exemplary intensity profiles of the track spots indicated by the yellow rectangles in (D-F). Unlike for protons and carbon ions the intensity profile ($\Delta x_{\mathrm{meas}} \approx 1200\,\mathrm{nm}$) of xenon ions (H) exhibits a plateau. The fluctuations are most probably by photon-shot-noise. Scale bars, $1\,\mu\mathrm{m}$.

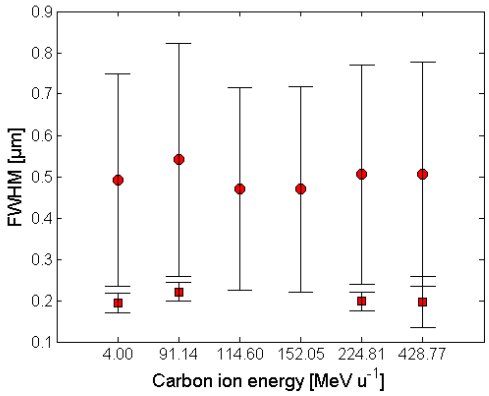

Figure 5.4.5: Comparison of the FWHM (Δx_{meas}) of carbon ion track spots gained by confocal (circles) and by STED (rectangles) microscopy. STED data was available for limited ion energies. Number of track spots investigated by STED microscopy (4.00, 91.14, 224.81, 428.77 MeV u^{-1}): 7, 5, 5, 8. The confocal data were gained by the read-out with the CLSM (Insert, Fig. 5.4.2). The error bars are the SD.

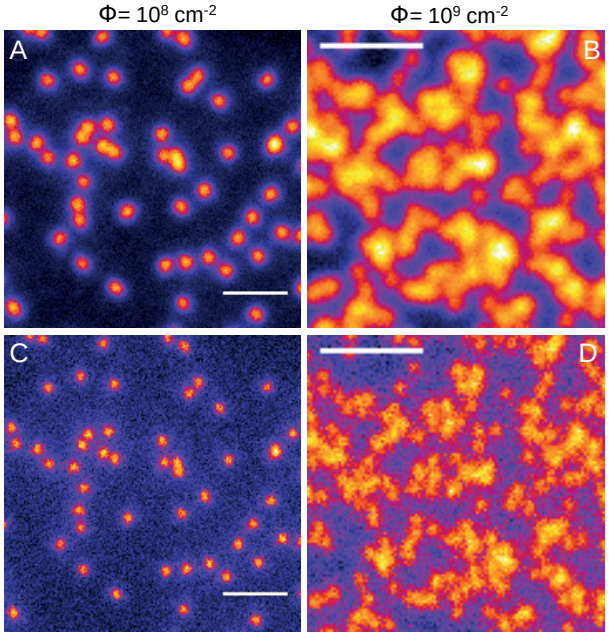

Figure 5.4.6: Comparison of the ion beam fluence resolved by confocal and STED microscopy. Carbon ion (4 MeV u^{-1}) beam fluences Φ resolved by confocal (A,B) and STED (C,D) microscopy. Unlike in the confocal data (A) very close track spots could mostly be separated in the STED data (C) at $\Phi = 10^8$ cm^{-2}. Currently, a clear discrimination at $\Phi = 10^9$ cm^{-2} is impossible for both imaging techniques (B,D). Scale bars, 2 μm.

5.5 Probing single cell fate after therapeutic ion irradiation

5.5.1 Morphological characterisation of the biological compartment

The tightly packed layer of A431 cells comprised a bulk cell density of approximately $3.05 \cdot 10^5\,\mathrm{cm}^{-2}$ (hD area, Fig. 5.5.1 and Table 5.5.1). Areas of lower cell density of approximately $1.06 \cdot 10^5\,\mathrm{cm}^{-2}$ occurred (lD area). Cells were partly overlapping in both areas. Shrinkage of the cell nuclei occurred during the total imaging period of approximately 19 h. Dense chromatin aggregates occurred in both areas. In the hD area and pC (positive control), cells seemed to halt proliferation during the whole imaging period.

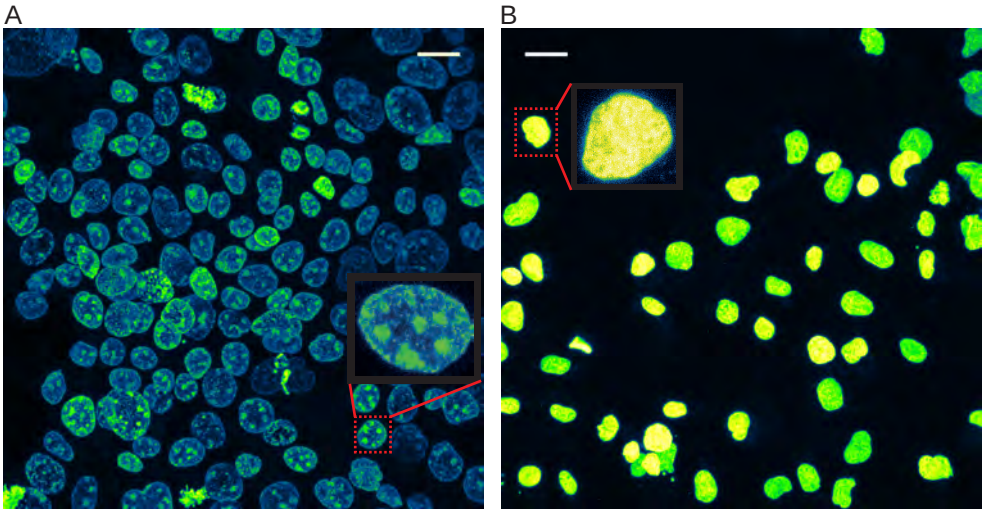

Figure 5.5.1: A431 cell coating. hD (A) and lD (B) areas 19 h after the irradiation. DNA in cell nuclei were stained with Draq5. Dense chromatin aggregates are visible in both areas. (B) Crescent-shaped chromatin aggregates occur. Inserts: Examples of localized (A) and very dense (B) chromatin condensation in the nucleus. Color coding: low (blue) and high (yellow) chromatin density. Scale bars, 20 μm.

Table 5.5.1: Characterisation of the A431 cell coating. The hD area and the pC were characterized 1 h, the lD area was characterized 19 h after irradiation. The pC represents also a high cell density area with a similar mean nucleus area A_n. In both positions the total nucleus area $A_{n,t}$ made up more than half of the imaging field. Semi-automatic ($A_{n,t}$) and automatic ($A_{n,t,a}$) segmentation of the nuclei gained similar results for the hD area and for the pC.

Imaging field (224 x 224 µm^2)	**# Cells**	**Cell density** [cm^{-2}]	**A_n** [µm^2]	**$A_{n,t}$** [%]	**$A_{n,t,a}$** [%]
High cell density (hD) area	167	3.05 * 10^5	168.09	55.9	54.6
Low cell density (lD) area	58	1.06 * 10^5	111.34	12.9	-
Positive control, pC	177	3.23 * 10^5	167.43	59.1	55.2

5.5.2 Ion hit statistics

All positions of identified ion traversals in the hD area are displayed in Figure 5.5.2A. All nuclei were hit twice at minimum (Fig. 5.5.2B,C). The median was 21 hits per nucleus. The number of nuclei hits seemed to be direct proportional to the nucleus area A_n (Fig. 5.5.2D). Greater hit numbers (> 41 hits, upper 5 percentile) were assigned to nuclei with increased A_n. The ion traversals were categorized into traversals by carbon (primary) ions and lighter fragments of ratio 1:2 (Fig. 5.5.3A).
Figure 5.5.3B displays a spatial inhomogeneity of the local LET (defined as mean LET per nucleus) in the hD area. The median was $54.81\,\mathrm{keV}\,\mu\mathrm{m}^{-1}$. Eight nuclei faced a local LET $\geq 78.65\,\mathrm{keV}\,\mu\mathrm{m}^{-1}$ (upper 5 percentile).
The actual macroscopic ion beam fluence in the hD area was assessed to be $1.34 \cdot 10^7$ cm^{-2} (Eq. 3.3). The local fluence (defined as number of hits per nucleus area) map shows also an inhomogeneous spatial distribution (Fig. 5.5.4A). There, the median was $1.34 \cdot 10^7\,\mathrm{cm}^{-2}$. Deviations by a factor of approximately 2.7 from the adjusted macroscopic ion beam fluence ($10^7\,\mathrm{cm}^{-2}$) occurred. On average, a nucleus was exposed to local dose (defined as the dose per nucleus) of 1.21 Gy (median) in the hD area (Fig. 5.5.4B). Eight cells faced a high dose in the nucleus $\geq 1.96\,\mathrm{Gy}$ (upper 5 percentile).
In comparison, the actual macroscopic ion beam fluence in the lD area was assessed to be $1.19 \cdot 10^7\,\mathrm{cm}^{-2}$. The ratio between incident carbon ions and lighter fragments was approximately 2:5. All nuclei were hit, at minimum twice. The median was at least 11.5 hits per nucleus.

5.5.3 Caspase-3/7 kinetics

Caspase-3/7 activation in the hD area was detectable within one hour after irradiation (Fig. 5.5.5). At the time point of irradiation all cells were assumed to be non-apoptotic. Despite small fluctuations, the caspase-3/7 activity was constantly rising. In the last time point (19 h after irradiation) the median has increased by a factor of approximately 1.4 compared to its initial value (Fig. 5.5.5B). A maximum response (and a subsequent fall-off) within the total time interval was yet not detectable. In comparison, caspase activation in the pC is also increasing but has a lower initial off-set and a lower maximum by a factor of approximately 4 and 2.1, respectively. On the contrary, the caspase activity in the lD area (19 h after irradiation) is much greater – by a factor of 5.5 – compared to the hD area. There all cells seemed to undergo apoptosis (apoptotic index: 100%).
Based on the minimum caspase signal in the lD area being considered as a threshold for apoptosis all apoptotic cells in the hD area and pC were identified accordingly (hD area: Fig. 5.5.6A). Despite a small initial fluctuation, no apoptosis seems to be triggered within the first 9 h after irradiation (Fig. 5.5.6B). The apoptotic index is

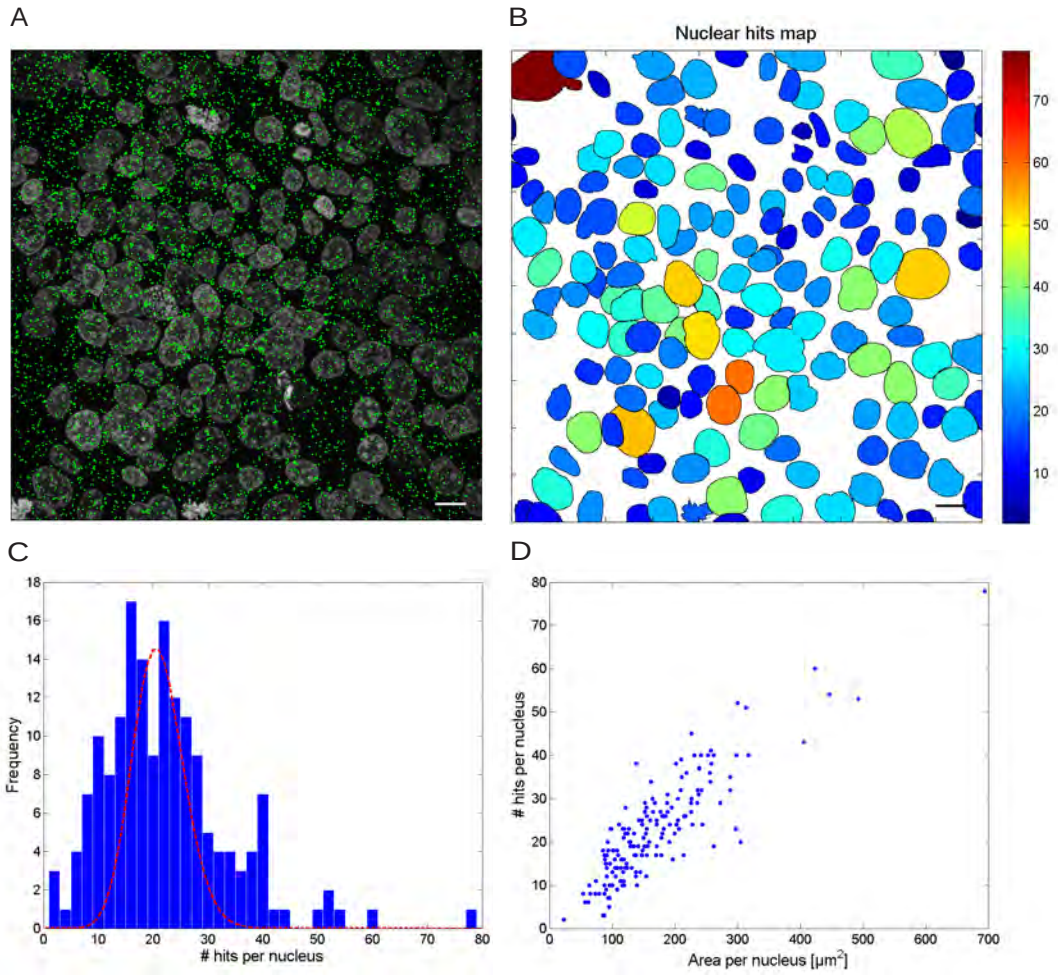

Figure 5.5.2: Ion hit statistics for the hD area. (A) Positions of all identified ion track centers (green crosses) in the high cell density (hD) area. Nuclei are labeled with Draq5. Corresponding map (B) and histogram (C) of all nuclei hits. (C) The red dotted line indicates the corresponding Poisson distribution ($\lambda = 21$). (D) Correlation between the number of nuclei hits and the area per nucleus in the hD area. Scale bars, 15 μm.

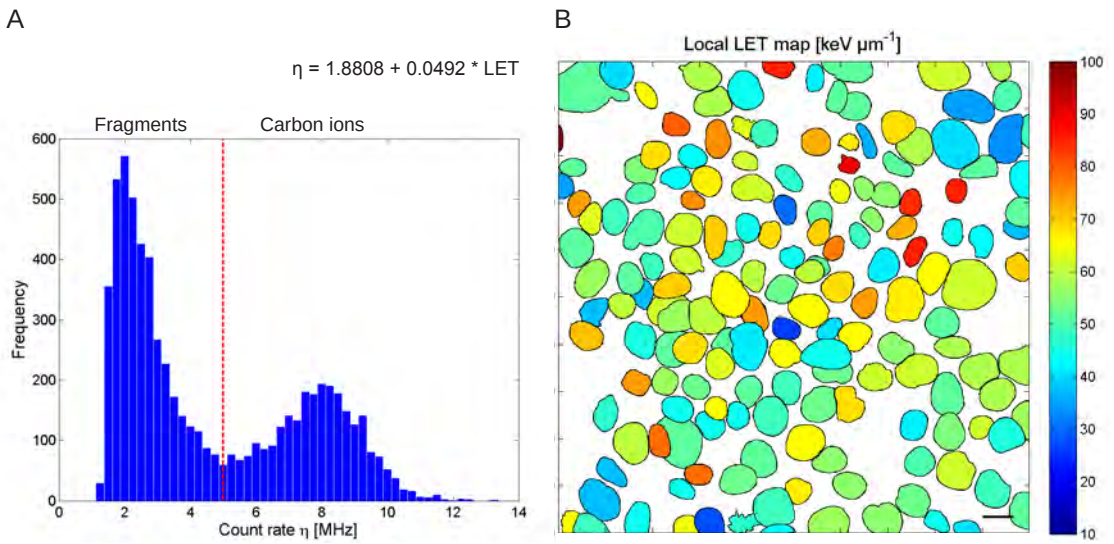

Figure 5.5.3: Intensities of the track spots and corresponding local LET in the hD area. (A) The maximum intensity (converted into the count rate η_{actual}) of each track spot was identified. According to the histogram the threshold was set to 5 MHz to distinguish between primary ions and fragments. (B) Local LET map of the ion traversals. Using the linear conversion (Eq. 6.1, also displayed here) the mean η_{actual} per nucleus was converted into the corresponding mean LET per nucleus. Scale bar, 15 μm.

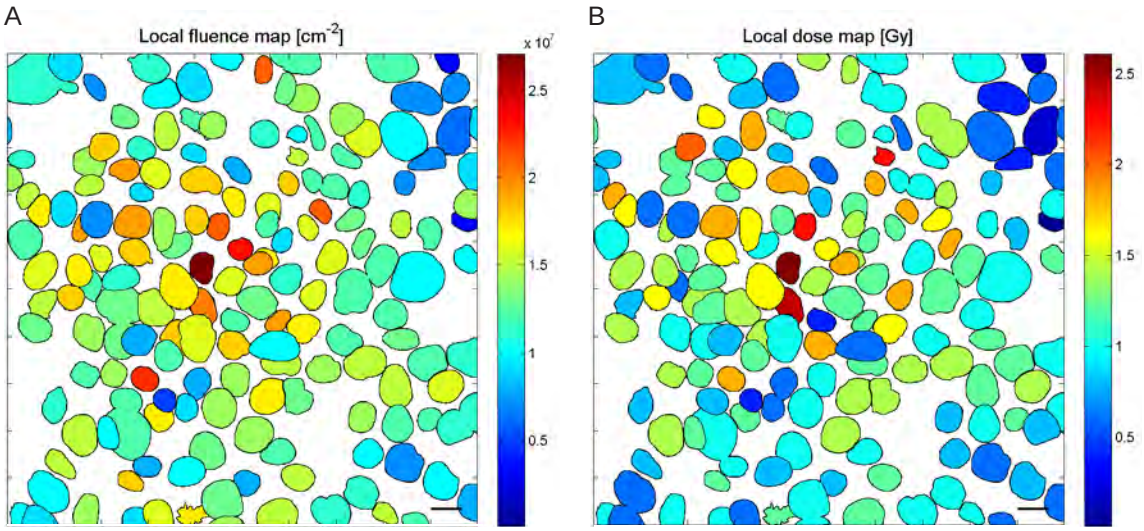

Figure 5.5.4: Local fluence and dose distribution in the hD area. (A) The local fluence was defined as the number of hits per nucleus divided by the nucleus area. (B) The local dose was calculated using Equation 2.4. Within a nucleus the fluence and dose was assumed to be constant. Scale bars, 15 μm.

increasing to 7.2% (in total 12 apoptotic cells) 19 h after irradiation. On the contrary, the apoptotic index of the pC is fluctuating around 1.13% (2 apoptotic cells) and is finally decreasing to zero.

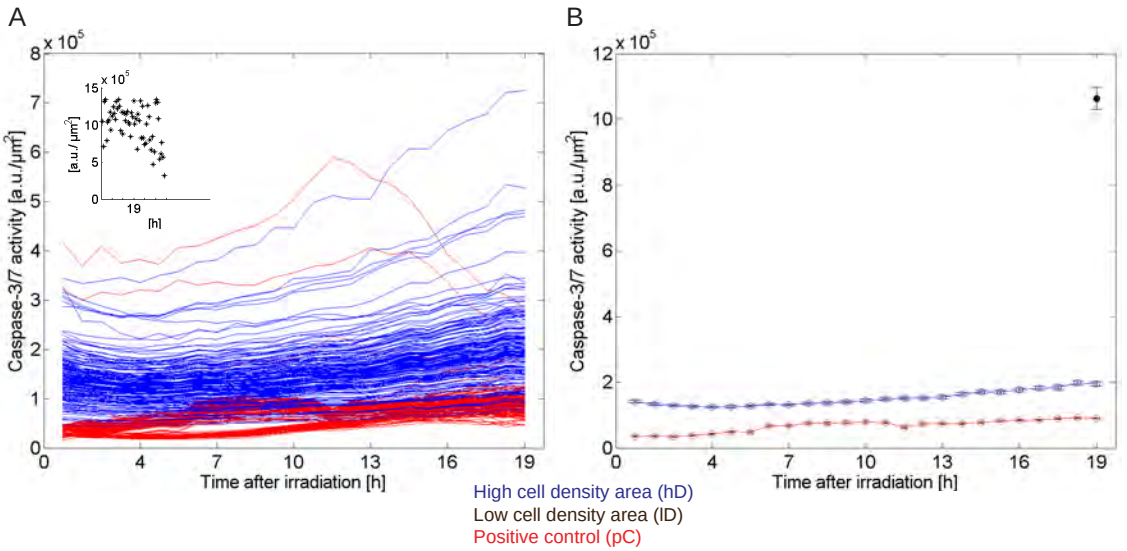

Figure 5.5.5: Caspase-3/7 activity. (A) Caspase signal per unit area (hD area: blue, pC: red) over time. Each line corresponds to the caspase activity of an individual cell. Few outliers with high activity occurred in the pC. Insert: a much higher activity was measured in the lD area 19 h after irradiation. (B) Median caspase signal over time. The error bars are the SEM.

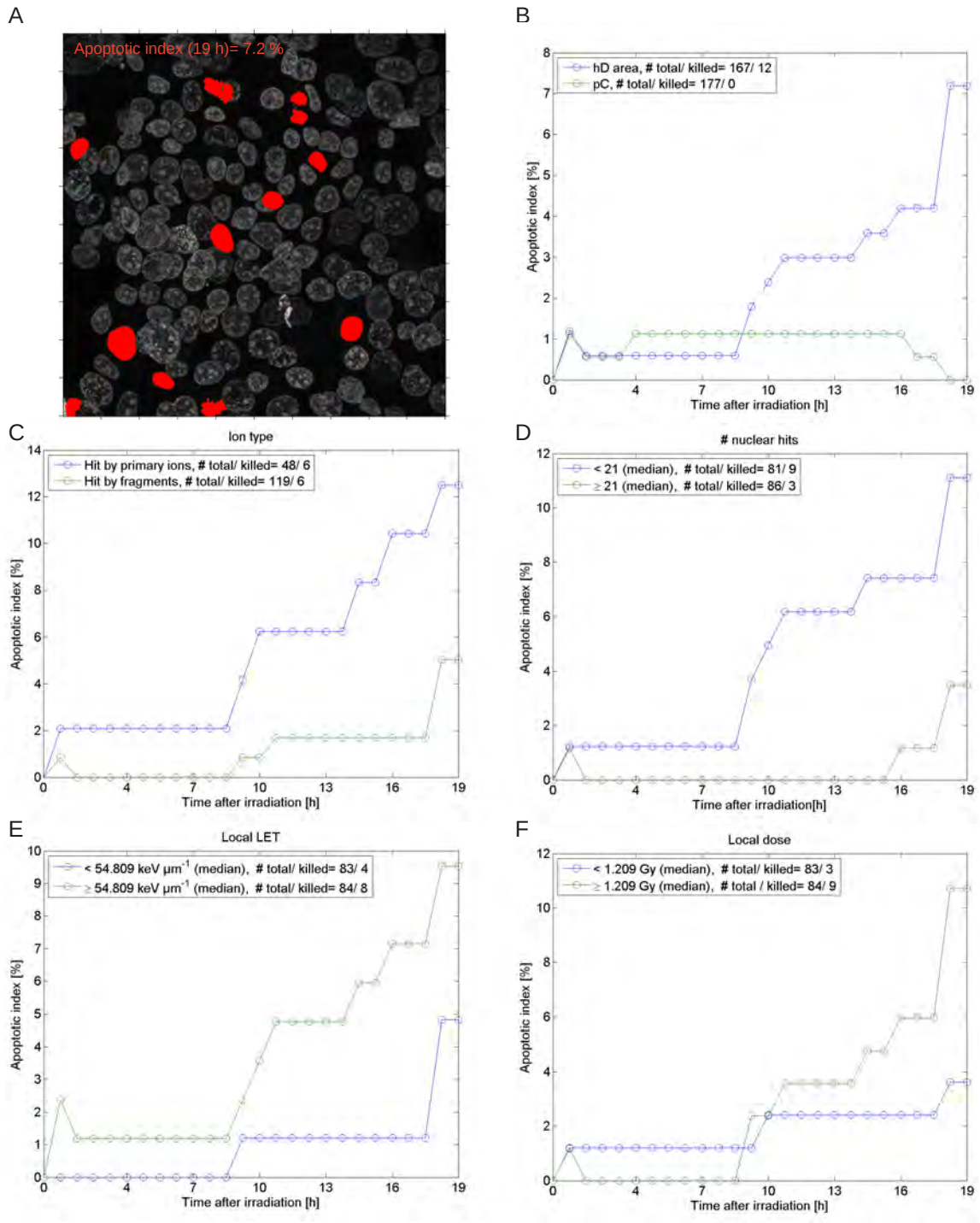

Figure 5.5.6: Apoptotic index of the hD area. (A) Apoptotic cells (19 h after irradiation) are labeled in red. (B) Apoptotic index over time in the hD area and in the pC. (C-F) According to the physical energy deposition in the nuclei the cells in the hD area were grouped (see legend, number of total and apoptotic cells of a sub-group are also displayed). The apoptotic index was determined for all sub-groups. The apparent decrease of the apoptotic index (especially in the pC) with increasing time could be attributed to inaccurate segmentation of the nuclei or to a temporal decrease in caspase activity.

6 Discussion

6.1 Engineering Cell-Fit-HD

The cell-coating experiments indicated that Al_2O_3:C,Mg is biocompatible with all cell lines tested. The cells were flat and spread thus indicating good cell attachment. Compared to standard treated surfaces for cell culture neither the morphology nor physiological properties of the cells seemed to be compromised when plated onto the FNTD surface. Further the physical properties of the surface seemed not to be affected by autoclaving and prolonged exposure to high humidity.
To improve coating by human U87 and murine SMA-560 cell line at low seeding concentration using an intermediate layer the fibronectin concentration should be optimized or another ECM component tested (Table 1 in B: *Results, FNTD crystals are biocompatible*). Concerning further experiments the focus should be on the A549 cell line. The cells maintain active metabolism, form tightly-packed monolayers with strong cell-cell adhesion and therefore limit cell migration possibly interfering future ion hit statistics (Fig. 5.1.1).
The FNTD surface seems to be compatible with common staining and fixation procedures. No dyes were accumulating at the surface causing an increased background during imaging and the cells maintained their morphology after fixation by PFA. It is possible to label (in terms of radiobiology) key cellular compartments like the nucleus or other key molecular and signaling events like Glucose uptake by immunofluorescence staining techniques (Fig. 5.1.2).
The cell layer and the FNTD could be read-out in-situ by the very same CLSM. No post-irradiation chemical processing nor a removal of the cells was necessary thus eliminating a significant source of error. Co-detection and correlation of radiation track information with cell biological parameters was possible (Fig. 5.1.3). The quality of the read-out signals of both compartments were not affected in the sequential acquisition. Together with application of common staining techniques, these are important pre-conditions for spatial correlation studies between physical energy deposition and biological response including the assessment of microscopic beam parameters.

6.2 Ion track reconstruction in 3D

The accuracy – expressed by $\Delta\theta$ and $PI_{x,y}$ – of 3D ion track reconstruction using the depth information gained by the FNTD read-out strongly depends on the irradiation angle θ and the approach to assess the track spot center [10].

6.2.1 Intensity profile of a track spot

Besides the energy of the swift ions, θ primarily governs the complexity of the intensity profile of a track spot (Fig. 5.2.1) [8]. Shallow angles cause elongation of the original radial-symmetric profile along beam direction. Tracks of δ electrons of broad angular distribution further distort the profile. In addition, the number of δ electron trajectories apparently rises under $\theta = 60°$. Due to a greater geometrical cross section of the incident ion with Al_2O_3:C,Mg the probability of producing such electrons increases. However, additional electron trajectories from neighboring ion traversals above or below crossing or being scattered into the actual imaging plane are also detected.
A masking of the actual physical track spot by the PSF of the CLSM occurs. Refractive index mismatches at the oil-cell layer and cell layer-FNTD boundary introduce spherical aberrations, leading to a distortion of the original PSF [31, 32, 65]. Next to a decrease in brightness, a blurred appearance of the track spots including the tattered edges under angular irradiation could be the effect.

6.2.2 Ion track center assessment

Evaluating the residuals of the LRA, weighting by intensity (approaches A: *iw centroid* and B: *rel thres*) seemed to assess the center of the track core best. A global threshold of 0.4 seemed to be appropriate to detect the sole track core (without δ electron trajectories). Additionally, dynamic thresholding (B) has the advantage of responding to different intensity profiles of a spectrum of particle types and energies constituting the incident ion beam. There, a threshold of 2/3 of the intensity maximum seemed to be appropriate not to run into the global maximum (the intensity profile exhibits a steep gradient) which is likely not to coincide with the actual center of the track spot. This mismatch could most likely be attributed to statistical fluctuations of energy deposition and local fluctuations of the F_2^{2+}(2Mg) color center density.
A fitting of the intensity profile by a 2D Gaussian function (symmetrical under perpendicular, elliptical under angular irradiation) could be an improvement to detect the actual center of a track spot (x_0, y_0) and hence improve the subsequent LRA.

6.2.3 Accuracy on particle track reconstruction in 3D

The irradiation angle θ governing the complexity of the track spot geometry has a major impact on the accuracy of track reconstruction. The much greater – by a factor of approximately six – residuals along (x) than perpendicular (y) to beam direction under $\theta = 60°$ gets directly reflected in greater $\Delta\theta$ (by a factor of approximately 10) compared to $\theta = 0°$, irrespective of the identification approach (D: Tables 1 and 2). The same manner goes for the PIs, especially for PI_y ($\theta = 60°$) being more than 10 times greater than the symmetrical PIs under $\theta = 0°$.
The great values of the error $\Delta\phi$ ($\theta = 0°$, D: Table 2), arising from the narrow distribution of the projections of the track spots onto the yz plane, could (as well as $\Delta\theta$) significantly be reduced by enlarging the total read-out range in z to 114 μm (D: Table 3). The PIs however remained nearly identical.
To assure a minimal extrapolation interval and hence to minimize the PIs in general it is favorable to start the read-out of the physical compartment close to the detector surface (Eq. 3.9).
A reasonable trade-off between a fast read-out ($\Delta z = 15\,\mu$m) and still high-accuracy, i.e. low $\Delta\theta$, $\Delta\phi$, is only possible under $\theta = 0°$. The PIs are however increasing as they depend on the inverse number of track spots considered for the LRA (Eq. 3.9).

6.2.4 Correction of axial geometrical distortion

Distortion by the refractive index mismatch mainly affects the axial position of the focal point and hence θ, the direction of the ion track. The introduction of non-linear corrections [59] and a spatial dependence of the ASF due to a different refractive index for individual organelles [66] could further improve track reconstruction.
To reduce spherical aberrations, cell-mounting medium 2,2'-Thiodiethanol (98%, n= 1.518) having the same refractive index as glass (hence a reduction to a single cell layer-Al_2O_3:C,Mg boundary) could be used [67]. Perpendicular irradiation should be favoured in particular for live-cell imaging. There, the nominal focal position can be approximated with the actual one.
The error term $(ASF_1 - ASF_2)\Delta s$ in Equation 4.2 affecting the actual focal position is independent of z and does not influence the flight direction of the ion. The error $\hat{x}$ (Eq. 4.3) of the position of the ion track in the horizontal is smaller than 0.5 μm for shallow irradiation angles (i.e. $\theta \leq 60°$, $\Delta s = 1\,\mu$m). It decreases steeply with θ approaching zero as long as $(ASF_1 - ASF_2) < 1$. The quantity $\hat{x}$ becomes yet more relevant for the spatial correlation of ion traversal and biological response on the molecular level.

6.2.5 Practical considerations

"To achieve the desired accuracy in determining the angle θ with an error smaller than 1° under angular irradiation at $\theta = 60°$ the intensity-weighted centroid detection and a 21 image stack separated by $\widehat{\Delta z} = 3\,\mu$m was found as the best set of image acquisition and processing parameters. Increasing $\widehat{\Delta z}$ to $6\,\mu$m (i.e. half the number of track spots) deteriorates the accuracy, i.e. $\Delta\theta$ and PI, roughly by 30% and 20% respectively. Concerning angles of irradiation with θ close to 0° and using the same fit parameters, $\Delta\theta$ decreases by a factor of at least 10 with nearly symmetrical lateral error distribution.
The required increase in accuracy of track reconstruction also increases the total read-out time of the detector. To further improve accuracy if necessary one could extent the total axial range of the image stack, to increase the number of images and decrease the image depth increment between two consecutive image planes ($\widehat{\Delta z}$). This, however, is more time consuming. Naturally the total microscope time is directly affected by the acquisition time of a single imaging plane (mainly governed by laser power p, dwell time τ, number of rescans R and total number of spots per imaging field [39]) influencing the signal-to-noise ratio and thus the quality of the detection of the track spot center."[1] [10].

6.3 DNA damage response to particle irradiation

With the Cell-Fit-HD it was possible to correlate 17 occurring RIF sequences – with at minimum 3 γ-H2AX foci – to the corresponding ion tracks. Despite a high sensitivity for DSB detection [56] only 4% of the cellular hits were causing a RIF sequence. Possible reasons could be cell-cycle arrest with a slowed down DNA repair dynamic (and hence lack of γ-H2AX) in the tightly packed A549 cell layer as well as DSBs already repaired within the time-frame before fixation.

6.3.1 Residuals

The mean residuals between the scattered RIFs and the ion tracks showed a systematic shift in x (perpendicular) and y (along beam direction, Fig. 5.3.2). An orchestrated rotation as well as a collective translation of the entire cell layer in the horizontal could be excluded to be main contributors as the orientation of the RIF sequences and of the ion tracks correlate well. Further small residuals (e.g. track 1) occur. Migration of individual cells in a tightly-packed cell layer is very unlikely. In contrast, the SD of γ_{RIF} (5.94°) and ϕ_{RIF} (3.71°) parametrizing the angular distribution of the RIF sequences could indicate slight rotations of individual nuclei.

[1] taken from D: *5. Conclusions*

Rather, inaccurate mechanical alignment of the microscope stage during the tile scan and the systematic error Δs (the uncertainty in the position of the FNTD surface in z) seemed to impose the residuals, especially in y a spatial dependence [11]. Additional systematic error in the residuals caused by limitation in the microscopy setup (stage precision, lowering of the stage in z, etc.) was below 1 μm.
Stress-induced cellular rearrangements as well as DSB repair dynamics (whether by passive diffusion [68] or directed migration of the DSBs [69]) could also lead to a residual shift. Further, the assumed isotropic labeling of the chromatin region surrounding the actual DSB (comprising approximately 2000 γ-H2AX [56]) is on a much greater length scale than the physical DSB and has to be critically considered.

6.3.2 Dynamics of the RIF sequence

Compared to the residuals being on the μm scale, the narrow distributions of the mean perpendicular per ion track emphasize a scattering of individual RIFs within a sequence on the sub-μm scale (E: Fig. 4B). The total ion interaction path length in the nucleus is only a limited measure for the number of RIFs per ion track. Additional biological parameters like the nucleus organisation have to be considered. The rather regular than random spacing between neighboring FOPs and RIFs (Insert in Fig. 5.3.3B) could be attributed to chromatin organisation [62, 70, 71] as well as RIF clustering [69, 72]. It could also indicate unrevealed correlations between the LET (expressed by the track-spot intensity, Fig. 5.4.1) and recurring biological response patterns. The majority of RIF sequences seemed to be caused by high-LET carbon ions (Fig. 5.3.3B). The appearance of distinct RIFs emphasizes a stochastic energy deposition rather than a continuous interaction pattern by the traversing ion (Fig. 5.3.1D,E,F). This resembles well with the appearance of blobs along single ion tracks (i.e. aggregations of energy depositions, Fig. 3.2.1C) which characterises the Al_2O_3:C,Mg based FNTD a promising biological cell surrogate candidate to mimic biological response to ion irradiation.

6.4 Resolving therapeutic particle spectrum

6.4.1 Characterisation by confocal microscopy

The analysis of the FNTD read-out signals showed a direct correlation of the maximum intensity of the track spot, whether assessed by direct measurements ($\hat{\eta}$) or 2D Gaussian fit ($\hat{A}$) to the LET of the incident particles (Figs. 5.4.1 and 5.4.3A). The additional energy loss and hence rising LET with increasing read-out depth (30 μm compared to 10 μm) as well as increasing spherical aberrations were neglected in the correlation. Color center inhomogeneities within and also between individual FNTDs were also neglected causing small-scale variations in the read-out signal.

Within the clinically relevant LET range $[0; 100\,\mathrm{keV}\,\mu\mathrm{m}^{-1}]$, a linear relationship seems to be a good approximation for the overall exponential function (Fig. 5.4.1):

$$\hat{\eta}\,[\mathrm{MHz}] = 0.00492 \cdot \mathrm{LET}\left[\mathrm{keV}\,\mu\mathrm{m}^{-1}\right] + 1.8808 \tag{6.1}$$

A mean variation of the actual count-rate of 10% (mean SD of $\hat{\eta}_{actual}$ for H-1 and C-12) translates into a LET uncertainty of about 14%. Strictly, the conversion is only valid for LET values $\geq 4.00\,\mathrm{keV}\,\mu\mathrm{m}^{-1}$ and $\leq 90.23\,\mathrm{keV}\,\mu\mathrm{m}^{-1}$ (Table 4.4.1). Despite its limitation Equation 6.1 was used to convert all occurring LET values (in the clinically relevant range) in this project. A characterisation of the track spot intensities of particles of very low LET and further investigations how these signals would behave with increasing read-out depth are crucial to improve this conversion. It has further to be investigated whether the range cut-off introduced by the masking of the track spots could be related to the LET_{Δ} (section 2.3).
A direct correlation between the FWHM of the track spots and the maximum secondary electron range (r_{max}) is limited by a masking of the read-out signals by the PSF of the CLSM. There seems to be an increase for particles heavier than C-12; for lighter particles (FWHM ≤ 0.5 μm) the PSF dominates the actual track spot profile. A FWHM of 500 nm seems to agree with the resolution of the CLSM ($\approx \lambda/2 = 320$ nm, Eq. 2.8) disturbed by spherical and other aberrations in the imaging path. At current stage, an indirect correlation between particle type and FWHM is therefore very limited.

6.4.2 Characterisation by STED microscopy

The decrease of the foreground signal (Fig. 5.4.4) could be attributed to – besides a smaller focal spot in lateral dimensions – a non vanishing intensity in the central zero of the STED laser. This causes a de-excitation of F_2^{2+}(2Mg) centers in the focal center. The increase in background by photochromic transformation or even vanishing track spots (by de-excitation of the color centers) might be caused by an increased probability of sequential two-photon absorption at high STED pulse energies (Fig. 3.2.2A).
The converging FWHM (Δx_{meas}) with increasing STED pulse energies – while the FWHM (Δx_{PSF}) of the PSF still declines – is a strong evidence to resolve the smallest feature of the track spots (personal communication with Henrich, M.). Together with a resolution capacity (Δx_{PSF}) of approximately 70 nm, the nanoscopic imaging could promise to probe the RDD of the swift ions in solid state detectors on the nm-scale. A retrospective convolution of the corresponding RDD (using the Scholz model) with the extracted PSF would reveal a plateau in the track core of radius 30 nm (H-1, 49.37 MeV) and of 45 nm (C-12, 152.05 MeV u^{-1}), respectively (Fig. 6.4.1). The plateau

of the RDD of xenon ions ($9.30\,\mathrm{MeV\,u^{-1}}$) would have a radius of approximately 110 nm. However, photon-dose response correction (Fig. A1) applied to account for saturation effects of the color centers (strictly speaking recorded under confocal microscopy) is only an approximation for the STED data and adds additional uncertainty in the RDD determination.

The decrease in the FWHM of the track spots under the STED read-out has a direct impact on the maximum resolvable ion beam fluence. The actual resolution of approximately 150 nm (Δx_{meas}, C-12, $152.05\,\mathrm{MeV\,u^{-1}}$) would allow to resolve a fluence up to $4.44 \cdot 10^{9}\,\mathrm{cm^{-2}}$ (assuming that two neighboring ion track centers have to be separated by Δx_{meas}). In reality the single ion traversals are however not equally spaced (Fig. 5.4.6). This limits the possibility to resolve every track spot at such a high fluence.

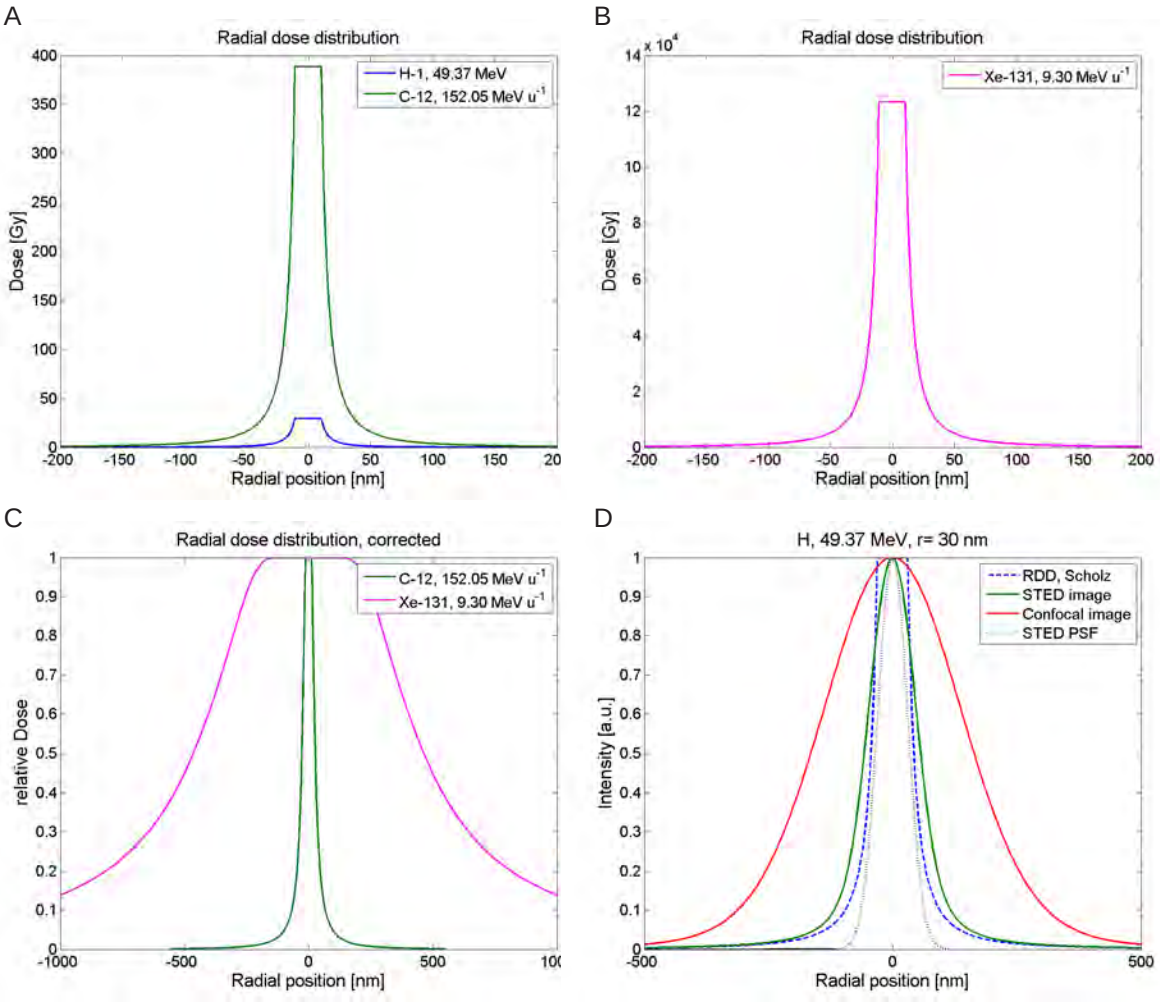

Figure 6.4.1: Radial dose distribution (RDD) and corresponding imaging data. (A) RDD using the Scholz model (plateau of radius 10 nm) for protons (49.37 MeV), carbon (152.05 MeV u^{-1}) and (B) xenon (9.30 MeV u^{-1}) ions. Computed using libamtrack [24]. (C) Corrected and scaled RDD for C-12 and Xe-131, applying the photon response saturation model to doses > 50 Gy. (D) Example of an actual track spot profile of H-1, 49.37 MeV gained by STED microscopy (green curve). The actual RDD (Scholz model, plateau radius of 30 nm, blue dashed curve) was convoluted with the PSF of the STED (black dotted curve, $\Delta x_{\mathrm{PSF}} = 70$ nm). The red curve shows the corresponding track spot gained by confocal microscopy. The confocal PSF has a FWHM of 300 nm (not shown here).

6.5 Probing single cell fate after therapeutic ion irradiation

The functional read-out of Cell-Fit-HD enables to probe single cell fate after therapeutic carbon ion irradiation. Live imaging of the biological compartment could successfully be employed to track the radiation-induced kill of individual cells over a time period of approximately 19 h. Besides the energy deposition in the nucleus, biological constraints (i.e. cell density) seemed to play an important role in the apoptotic cell death kinetics of A431 cells.

6.5.1 Ion hit statistics

Next to the visualization of tracks of penetrating ions on the sub-μm scale, the read-out of the physical compartment also allows to parametrize the spatial energy deposition distribution in each nucleus (Figs. 5.5.2, 5.5.3, 5.5.4). The decline in the fluence of primary ions by a factor of approximately two due to fragmentation processes in the absorber material in front of the hybrid detector could successfully be monitored. However, the increase of the total fluence by a factor of 1.34 is apparently too low. Due to the lower LET_∞ threshold of 0.5 keV $\mu\mathrm{m}^{-1}$ in water, the FNTD seemed not to detect emerging fast protons of kinetic energies > 170 MeV. Additionally, a clear separation between track spots by fast protons and by secondary electrons released in Al_2O_3:C,Mg was not always possible affecting the detected ion beam fluence. Due to their low LET the corresponding contribution to the physical dose deposition and hence the biological effect of the fast protons (compared to the carbon ions) is however small.
Despite a simplified approach, the assessed LET (54.81 keV $\mu\mathrm{m}^{-1}$) and dose per nucleus (1.21 Gy) seem to approach the computed macroscopic LET (58.46 keV $\mu\mathrm{m}^{-1}$) and dose (0.94 Gy) of the adjusted ion beam well. Despite the apparent discrepancy the actual difference should be in fact smaller. Projectiles of lower kinetic energies emerging from the stochastic nature of energy deposition were neglected in the computation according to [24]. The computed values should therefore be shifted to greater numbers. Counting only direct nuclei hits and assuming the dose to be constant within the nucleus (Fig. 5.5.4B) is only an approximation of the actual microscopic dose distribution in the nucleus. Further, the deposited dose was assumed to be equal to the absorbed dose. To further improve the actual dose distribution energy deposition by released δ electrons of nearby ion traversals should also be taken into account superimposing the localized energy deposition (i.e. deposited dose) by direct hits.

6.5.2 Relating caspase activity to microscopic beam parameters

The ion hit statistics in the hD and lD area nearly equals. The apparent smaller number of nuclei hits in the lD area seems to arise from the shrinkage of the cell nuclei. The correlation for this area was performed 19 h after irradiation. Despite 21 (median) nuclei hits in the hD area only 7.2% of the cells were caspase-3/7 positive objects 19 h after irradiation. The occurring resistance could be induced by increased cell-cell communication due to the high cell density with a subsequent delay in caspase activity. On the contrary all cells in the lD area were identified to be apoptotic. Morphological indications for apoptosis (formation of dense and crescent-shaped chromatin aggregates, Fig. 5.5.1B) accompanied the activation of caspase in the hD area.
According to the p values of the log-rank test (Table 6.5.1) the survival (1- apoptotic index) of the irradiated cells over time does not significantly depend on the microscopic energy deposition in the nucleus (Fig. A2). Except the local LET, the corresponding p values are yet close to the 5% level of significance. Increasing the level of significance to 10%, cells facing a higher dose, fluence and hits by primarily carbon ions in the nucleus have a significant greater probability to undergo radiation-induced apoptosis within 19 h after irradiation. At a first glance it seems that cells facing a smaller number of nuclei hits exhibit a significantly higher probability to become apoptotic. Although a small number of nuclei hits, the hits were mostly caused by primary ions of higher LET ($\geq 63.40\,\mathrm{keV}\,\mu\mathrm{m}^{-1}$).
The small number of apoptotic cells in the hD area however limits the possibility to draw reliable and evidence-based conclusions. It is therefore necessary to extend the total imaging time in order to conclude whether the low apoptotic index is only temporarily or whether it is actually governed by a combination of physical and biological constraints.
To minimize the influence by the possible cytotoxicity of intercalating dyes transgenic cell lines expressing nucleus-tethered fluorescence markers (e.g. h2a-mCherry or 53bp-mCherry) with a signal sufficient for nuclear segmentation algorithms could be used [73]. Despite the viability of the cell coating – characterized by the nuclear morphology and low caspase-3/7 activation in the pC – intercalation of Draq5 in the DNA seems to have an anti-proliferative effect [74].
In order to analyse a much greater number of cells and to reduce the image processing time, image segmentation algorithms could be applied. The hereby assessed total nucleus area $A_{n,t,a}$ coincided well with the total nucleus area $A_{n,t}$ under semi-automatic segmentation (Table 5.5.1). Despite a successful identification of the cell nuclei it was yet not possible to separate overlapping nuclei by such routine (Fig. 6.5.1).
Caspase-3/7 independent apoptotic pathways as well as other forms of cell kill (e.g. necrosis) should additionally be considered to gain the total number of dying cells and to hence estimate the tumor control.

Table 6.5.1: P values of the log-rank test.

Group	p value
Ion type	0.0798
Number of nuclear hits	0.0532
LET	0.227
Fluence	0.0856
Dose	0.0798

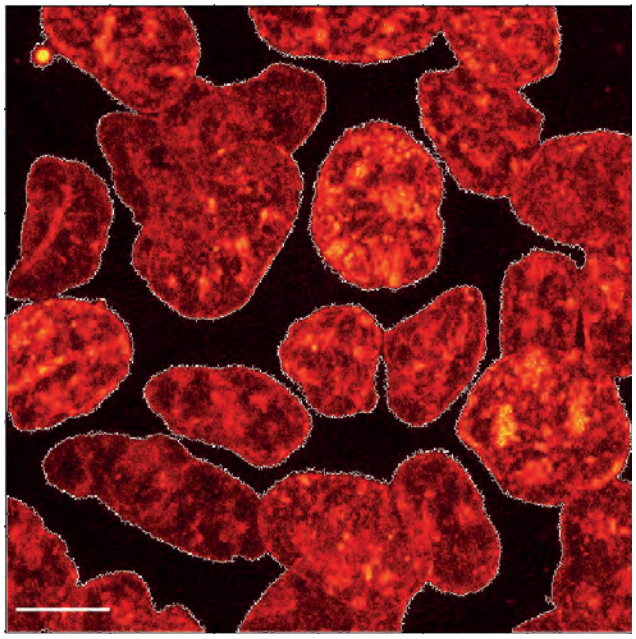

Figure 6.5.1: Automatic nuclei segmentation using the Draq5 channel. Only a section is displayed. The perimeter of the identified nuclei is indicated in white. With the algorithm used it is not possible to separate overlapping nuclei. Scale bar, 10 μm.

7 Conclusions and Outlook

The novel hybrid detector Cell-Fit-HD was successfully developed and validated. The hybrid comprises the fluorescent nuclear track detector (FNTD) – a cell substrate as well as a detector for particle track visualization and reconstruction. A viable cell coating of the FNTD (the physical compartment) adds additional biological compartment and thus forms the hybrid composite. Cell-Fit-HD provides full 3D visualization and direct spatial correlation of single ion tracks and the corresponding subcellular damage sites. It allows to extract microscopic physical parameters of each detected ion and to correlate them to the cellular damage response pattern. The read-out in-situ by a single CLSM, available in many state-of-the-art life science research facilities, is the key feature of this radiobiological tool. Neither a removal of the biological nor post-irradiation chemical processing of the physical compartment are required for the read-out. The unique spatial resolution limited only by the employed method of optical microscopy allows the Cell-Fit-HD to be applicable in clinical ion beams. The hybrid detector is not restricted to any irradiation facility.

Validation studies revealed the functionality of Cell-Fit-HD on different length- and time scales in IBCT (Fig. 7.0.1). Besides the demonstrated correlation of the physical energy deposition (i.e. the ion tracks) to the radiation-related cellular events on the subcellular and single cell level, the hybrid detector principally sets no constraints for a correlation on greater length scales. The biocompatible surface of the FNTD allowing for prolonged and sterile cell culture promises to coat with cell structures from living tissue (ex-vivo) as well as 3D cell culturing in order to establish a model more representative of the in-vivo state. At the moment the working distance of the objective (around 180 μm) imposes the major restriction on the cell layer height.

The hit-response analysis is not restricted to a single glimpse in time. The ability for live-cell imaging of the biological compartment (without affecting the 3D information stored in the physical compartment) enables not only spatial but also important temporal correlations studies over a longer time-period. Combined with a subcellular resolution, cell-killing effects in the vicinity of a particle hit can be studied in order to identify other critical targets than the nucleus. Simultaneously, the radiation-related molecular mechanism can be related to the cell survival kinetics (and hence tumor control) of the biological compartment on greater time scales.

Despite the currently limited parameterization of the penetrating ion registered in the

physical compartment, it yet allows for unique correlations between microscopic biological response quantities and microscopic beam parameters. By optical nanoscopy it could be even possible to reveal substructures of a single physical energy deposition event. This can help to refine the current standard model for predicting biological damage from ionizing radiation and to model tissue response as a function of a plethora of physical and biological constraints. Making a transition back from a microscopic to a macroscopic scale (i.e. the whole tumor) could help to adjust therapeutic ion beam parameters, elucidate the superiority of IBCT for the treatment of certain tumors, and estimate the effect of normal tissue complication. These studies will be valuable in the search for a more appropriate parameter for the quantification of tumor response to IBCT than the dose absorbed.

The simple design of Cell-Fit-HD and its confocal read-out as well as the possibility of carrying out conventional cell labeling and detection experiments (as with cells grown on ordinary substrates) could be instrumental for research in radiobiology laboratories with limited access and expertise in detector technology. A very short irradiation time (less than 10 s for a single Cell-Fit-HD) makes experiments under therapeutic conditions feasible.

Collectively, Cell-Fit-HD could provide a basis for future radiobiological experiments to gain a deeper understanding between particle hits and resulting biological effects beyond the statistical relations we know today.

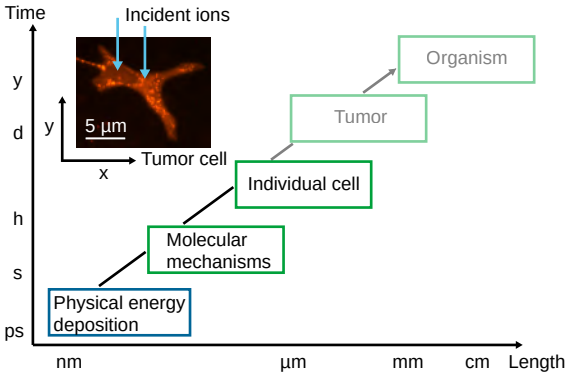

Figure 7.0.1: Current status of biological response to ion irradiation on a multi-scale approached by Cell-Fit-HD. Principally, there is no limit to achieve correlation on greater length scales (e.g. tumor).

Acknowledgements

Ich möchte mich bei all den Personen bedanken, die mein Promotionsprojekt mit unermüdlicher Unterstützung begleiteten.
Besonders bedanken möchte ich mich bei Herrn Professor Dr. O. Jäkel, Leiter der Schwerionentherapiegruppe am DKFZ. Er unterstützte mich in all meinen Vorhaben unermüdlich und ohne zu zögern. Durch seine positive und offene Art hatte ich mich schnell in seiner Arbeitsgruppe integriert und fühlte mich von Anfang an wohl. Er ermöglichte mir den Besuch vieler Konferenzen, welche mich inspirierten und für mich eine große Bereicherung waren.
Ich möchte mich bei Herrn Professor Dr. Dr. J. Debus, ärztlicher Direktor der Radioonkologie und Strahlentherapie des Universitätsklinikums Heidelberg, für die kontinuierlichen, offenen Diskussionen bezüglich meiner Forschungsergebnisse und der Beurteilung neuer Forschungsvorhaben bedanken.
Ein Dank geht an Frau Professorin Dr. S. Combs, leitende Oberärztin in der Radioonkologie und Strahlentherapie des Universitätsklinikums Heidelberg, für die jährliche Evaluation meiner Projektergebnisse.
Ein großer Dank gilt auch Herrn Dr. Dr. A. Abdollahi, Leiter der translationalen Radioonkologie am DKFZ, für seine Zusammenarbeit in der Radiobiologie. Er gewährte mir uneingeschränkten Zugang zu seinen Laboren und Mitteln. Konstruktive Diskussionen mit ihm halfen mir bei meinem Forschungsvorhaben.
Ich möchte mich von ganzem Herzen bei Herrn Dr. S. Greilich bedanken, der dieses Promotionsprojekt initiierte. Gemeinsam konnten wir neue Wege gehen und unsere hochgesetzten Ziele erreichen. Nicht nur beruflich, sondern auch in vielen privaten Gesprächen stand er mir zur Seite.
Ein besonderer Dank geht an Herrn Dr. S. Brons für die Organisation und Unterstützung bei den Bestrahlungen am HIT, aber auch an Herrn Dr. F. Bestvater und Frau M. Broms, die mir bei den vielen Fragen bezüglich der Mikroskopie immer sofort weiterhalfen.
Ich möchte mich bei Bernadette, Julia, Nora und Stefan für das tolle Klima unter uns Doktoranden bedanken. Es gab kein Konkurrenzdenken, die gegenseitige Unterstützung stand immer im Vordergrund.
Danke an all meine Freunde, besonders Neckarstaden 18, die immer ein offenes Ohr für mich hatten.

Ich möchte mich von ganzem Herzen bei Brigitta Rübel bedanken, die mich trotz ihrer Krebserkrankung unterstützte und interessiert meinen Forschungsverlauf verfolgte. Bedanken möchte ich mich sehr bei meinen Eltern für die unermüdliche Unterstützung. Sie ermöglichten mir nach meiner beruflichen IT-Ausbildung, das Abitur nachzuholen, zu studieren und somit diese Promotion überhaupt antreten zu können.
Danke, Klara - eigentlich für alles.

Bibliography

[1] M. Jermann. Particle Therapy Co-operative Group. Patient statistics per end of 2012. 2013, URL: http://ptcog.web.psi.ch.

[2] Particle Therapy Co operative Group. Particle therapy facilities in a planning stage or under construction. 2013, URL: http://ptcog.web.psi.ch/ptcentres.html.

[3] S.E. Combs, O. Jäkel, T. Haberer, and J. Debus. Particle therapy at the Heidelberg Ion Therapy Center (HIT) - integrated research-driven university-hospital-based radiation oncology service in Heidelberg, Germany. *Radiother. Oncol.*, 95(1):41–44, 2010.

[4] H. Bucker, G. Horneck, O.C. Allkofer, K.P. Bartholoma, R. Beaujean, P. Cuer, W. Enge, R. Facius, H. Francois, E.H. Graul, G. Henig, W. Heinrich, R. Kaiser, H. Kuhn, J.P. Massue, H. Planel, G. Portal, E. Reinholz, W. Ruther, W. Scheuermann, R. Schmitt, E. Schopper, J.U. Schott, J.P. Soleilhavoup, and H. Wollenhaupt. The Biostack experiment on Apollo 16. *Life Sci. Space Res.*, 11:295–305, 1973.

[5] H. Bucker. The Biostack Experiments I and II aboard Apollo 16 and 17. *Life Sci. Space Res.*, 12:43–50, 1974.

[6] M.S. Akselrod and G.J. Sykora. Fluorescent nuclear track detector technology - A new way to do passive solid state dosimetry. *Radiat. Meas.*, 46(12):1671–1679, 2011.

[7] J.-M. Osinga, M.S. Akselrod, R. Herrmann, V. Hable, G. Dollinger, O. Jäkel, and S. Greilich. High-accuracy fluence determination in ion beams using fluorescent nuclear track detectors. *Radiat. Meas.*, 56(0):294–298, 2013.

[8] M. Niklas, C. Melzig, A. Abdollahi, J. Bartz, M.S. Akselrod, J. Debus, O. Jäkel, and S. Greilich. Spatial correlation between traversal and cellular response in ion radiotherapy - Towards single track spectroscopy. *Radiat. Meas.*, 56(0):285–289, 2013.

[9] M. Niklas, S. Greilich, C. Melzig, M.S. Akselrod, J. Debus, O. Jäkel, and A. Abdollahi. Engineering cell-fluorescent ion track hybrid detectors. *Radiat. Oncol.*, 8:141, 2013, DOI: 10.1186/1748-717X-8-141.

[10] M. Niklas, J.A. Bartz, M.S. Akselrod, A. Abdollahi, O. Jäkel, and S. Greilich. Ion track reconstruction in 3D using alumina-based fluorescent nuclear track detectors. *Phys. Med. Biol.*, 58(18):N251–266, 2013.

[11] M. Niklas, A. Abdollahi, M.S. Akselrod, J. Debus, O. Jäkel, and S. Greilich. Subcellular Spatial Correlation of Particle Traversal and Biological Response in Clinical Ion Beams. *Int. J. Radiat. Oncol.*, 87(5):1141–1147, 2013.

[12] O. Jäkel. State of the Art in Hadron Therapy. *Aip. Conf. Proc.*, 958:70–77, 2007.

[13] D. Schardt and T. Elsässer. Heavy-ion tumor therapy: Physical and radiobiological benefits. *Rev. Mod. Phys.*, 82:383–425, 2010.

[14] H. Paganetti, A. Niemierko, M. Ancukiewicz, L.E. Gerweck, M. Goitein, J.S. Loeffler, and H.D. Suit. Relative biological effectiveness (RBE) values for proton beam therapy. *Int. J. Radiat. Oncol.*, 53(2):407–421, 2002.

[15] J. Telsemeyer. *Investigation of an Amorphous Silicon Flat-Panel Detector for Ion Radiography.* PhD thesis, University of Heidelberg, 2012.

[16] M. Belli, F. Cera, R. Cherubini, M. Dalla Vecchia, A.M. Haque, F. Ianzini, G. Moschini, O. Sapora, G. Simone, M.A. Tabocchini, and P. Tiveron. RBE-LET relationships for cell inactivation and mutation induced by low energy protons in V79 cells: further results at the LNL facility. *Int. J. Radiat. Biol.*, 74(4):501–509, 1998.

[17] Y. Furusawa, K. Fukutsu, M. Aoki, H. Itsukaichi, K. Eguchi-Kasai, H. Ohara, F. Yatagai, T. Kanai, and K. Ando. Inactivation of aerobic and hypoxic cells from three different cell lines by accelerated (3)He-, (12)C- and (20)Ne-ion beams. *Radiat. Res.*, 154(5):485–496, 2000.

[18] M. Scholz. Effects on ion radiation on cells and tissues. *Adv. Polym. Sci.*, 62:96–155, 2003.

[19] W.R. Leo. *Techniques for Nuclear and Particle Physics Experiments, A How-to Approach*, chapter Energy Loss of Heavy Charged Particles by Atomic Collisions, pages 21–34. Springer, 1994.

[20] T. Elsässer, A. Gemmel, M. Scholz, D. Schardt, and M. Krämer. The relevance of very low energy ions for heavy-ion therapy. *Phys. Med. Biol.*, 54(7):N101–106, 2009.

[21] H. Bethe. Zur Theorie des Durchgangs schneller Korpuskularstrahlen durch Materie. *Ann. Phys.*, 397:325–400, 1930.

[22] F. Bloch. Zur Bremsung rasch bewegter Teilchen beim Durchgang durch die Materie. *Ann. Phys.*, 16:285–320, 1933.

[23] International Commission on Radiation Units and Measurements. Fundamental Quantities and Units for Ionizing Radiation. *ICRU report 60*, 1998.

[24] S. Greilich, L. Grzanka, N. Bassler, C.E. Andersen, and O. Jäkel. Amorphous track models: A numerical comparison study. *Radiat. Meas.*, 45(10):1406–1409, 2010.

[25] International Commission on Radiation Units and Measurements. Linear Energy Transfer. *ICRU report 16*, 1970.

[26] M. Krämer. Calculation of heavy-ion track structure. *Nucl. Instrum. Meth. B*, 105(1-4):14–20, 1995.

[27] J.J. Butts and R. Katz. Theory of RBE for heavy ion bombardment of dry enzymes and viruses. *Radiat. Res.*, 30(4):855–871, 1967.

[28] M. Scholz and G. Kraft. Track structure and the calculation of biological effects of heavy charged particles. *Adv. Space Res.*, 18(1-2):5–14, 1996.

[29] M. Krämer and M. Durante. Ion beam transport calculations and treatment plans in particle therapy. *Eur. Phys. J. D*, 60(1):195–202, 2010.

[30] S. Inoue. *Handbook Of Biological Confocal Microscopy*, chapter Foundations of Confocal Scanned Imaging in Light Microscopy, pages 1–19. Springer, 2006.

[31] S. Hell, G. Reiner, C. Cremer, and E.H.K. Stelzer. Aberrations in confocal fluorescence microscopy induced by mismatches in refractive index. *J. Microsc.*, 169(3):391–405, 1993.

[32] H. Jacobsen and S.W. Hell. Effect of the specimen refractive index on the imaging of a confocal fluorescence microscope employing high aperture oil immersion lenses. *Bioimaging*, 3:39–47, 1995.

[33] E. Abbe. Beiträge zur Theorie des Mikroskops und der mikroskopischen Wahrnehmung. *Arch. Mikr. Anat.*, 9:413–468, 1873.

[34] S.W. Hell. Far-Field Optical Nanoscopy. *Science*, 316(5828):1153–1158, 2007.

[35] A. Diaspro, P. Bianchini, G. Vicidomini, M. Faretta, P. Ramoino, and C. Usai. Multi-photon excitation microscopy. *Biomed. Eng. Online*, 5(1):36, 2006.

[36] S.W. Hell. Microscopy and its focal switch. *Nat. Meth.*, 6(1):24–32, 2009.

[37] K.I. Willig, S.O. Rizzoli, V. Westphal, R. Jahn, and S.W. Hell. Sted microscopy reveals that synaptotagmin remains clustered after synaptic vesicle exocytosis. *Nature*, 440(7086):935–939, 2006.

[38] G.J. Sykora, M.S. Akselrod, and N. Benton, E.R.and Yasuda. Spectroscopic properties of novel fluorescent nuclear track detectors for high and low LET charged particles. *Radiat. Meas.*, 43(2-6):422–426, 2008.

[39] S. Greilich, J.-M. Osinga, M. Niklas, F.M. Lauer, G. Klimpki, F. Bestvater, J.A. Bartz, M.S. Akselrod, and O. Jäkel. Fluorescent nuclear track detectors as a tool for ion-beam therapy research. *Radiat. Meas.*, 56(0):267 – 272, 2013.

[40] S. Sanyal and M.S. Akselrod. Anisotropy of optical absorption and fluorescence in Al2O3:C,Mg crystals. *J. Appl. Phys.*, 98(3):033518–1–033518–12, 2005.

[41] M.S. Akselrod, A.E. Akselrod, S.S. Orlov, S. Sanyal, and T.H. Underwood. Fluorescent Aluminum Oxide Crystals for Volumetric Optical Data Storage and Imaging Applications. *J. Fluoresc.*, 13(6):503–511, 2003.

[42] J.-M. Osinga. Fluorescent nuclear track detectors: High-accuracy fluence determination in ion beams. Master's thesis, Martin Luther University of Halle-Wittenberg, 2012.

[43] Carl Zeiss MicroImaging GmBH. Zen 2009 LSM 710 and ConfoCor 3: Operating Manual. 2009.

[44] M. Reuss, J. Engelhardt, and S.W. Hell. Birefringent device converts a standard scanning microscope into a sted microscope that also maps molecular orientation. *Opt. Express*, 18(2):1049–1058, 2010.

[45] M. Henrich. *The Potential of Semiconductor Lasers in STED Nanoscopy*. PhD thesis, University of Heidelberg, Germany, 2014.

[46] J. Cardinale. Histogram-based background subtractor for ImageJ. Technical report, MOSAIC Group, ETH Zuerich, Switzerland, 2010.

[47] I.F. Sbalzarini and P. Koumoutsakos. Feature point tracking and trajectory analysis for video imaging in cell biology. *J. Struct. Biol.*, 151(2):182–195, 2005.

[48] J.A. Helmuth, C.J. Burckhardt, U.F. Greber, and I.F. Sbalzarini. Shape reconstruction of subcellular structures from live cell fluorescence microscopy images. *J. Struct. Biol.*, 167(1):1–10, 2009.

[49] W.S. Rasband. Imagej. *U.S. National Institutes of Health, Bethesda, Maryland, U.S.A.*, URL: http://rsbweb.nih.gov/ij/.

[50] M.D. Abramoff, P.J. Magelhaes, and S.J. Ram. Image processing with imagej. *Biophotonics international*, 11(7):36–42, 2004.

[51] R. Martel. Werkzeuge zur Untersuchung des Hintergrundes von fluoreszierenden Kernspurdetektoren. Bachelor's thesis, University of Heidelberg, 2012.

[52] Molecular Probes. Product Manual, Acetoxymethyl (AM) and Acetate Ester derivatives of fluorescent indicators and chelators. 2010.

[53] Molecular Probes. Product Manual, DiI Derivatives for Long-Term Cellular Labeling. 2005.

[54] Molecular Probes. Product Manual, Hoechst Stains. 2005.

[55] Abcam. Product Datasheet, Anti-Glucose Transporter GLUT1 antibody ab652.

[56] E.P. Rogakou, D.R. Pilch, A.H. Orr, V.S. Ivanova, and W.M. Bonner. DNA double-stranded breaks induce histone H2AX phosphorylation on serine 139. *J. Biol. Chem.*, 273:5858–5868, 1998.

[57] H. Cen, F. Mao, I. Aronchik, R.J. Fuentes, and G.L. Firestone. DEVD-NucView488: a novel class of enzyme substrates for real-time detection of caspase-3 activity in live cells. *FASEB J.*, 22 (7):2243–2252, 2008.

[58] D.C. Montgomery, E.A. Peck, and G.G. Vining. *Introduction to linear regression analysis.*, chapter Simple linear regression, pages 12–34. John Wiley & Sons, Inc., 2006.

[59] H.J. van Elburg, L.C. Kuypers, W.F. Decraemer, and J.J.J. Dirckx. Improved correction of axial geometrical distortion in index-mismatched fluorescent confocal microscopic images using high-aperture objective lenses. *J. Microsc.*, 228(Pt 1):45–54, 2007.

[60] O. Jäkel, C. Jacob, D. Schardt, C.P. Karger, and G.H. Hartmann. Relation between carbon ion ranges and x-ray CT numbers. *Med. Phys.*, 28(4):701–703, 2001.

[61] G.M. Akselrod, M.S. Akselrod, E.R. Benton, and N. Yasuda. A novel Al2O3 fluorescent nuclear track detector for heavy charged particles and neutrons. *Nucl. Instrum. Meth. B*, 247(2):295–306, 2006.

[62] B. Jakob, M. Scholz, and G. Taucher-Scholz. Biological imaging of heavy charged-particle tracks. *Radiat. Res.*, 159(5):676–684, 2003.

[63] I.M. Ward and J. Chen. Histone H2AX is phosphorylated in an ATR-dependent manner in response to replicational stress. *J. Biol. Chem.*, 276(51):47759–47762, 2001.

[64] S. Hanasoge and M. Ljungman. H2AX phosphorylation after UV irradiation is triggered by DNA repair intermediates and is mediated by the ATR kinase. *Carcinogenesis*, 28(11):2298–2304, 2007.

[65] K. Carlsson. The influence of specimen refractive index, detector signal integration, and non-uniform scan speed on the imaging properties in confocal microscopy. *J. Microsc.*, 163(2):167–178, 1991.

[66] J. Beuthan, O. Minet, J. Helfmann, M. Herrig, and G. Müller. The spatial variation of the refractive index in biological cells. *Phys. Med. Biol.*, 41(3):369–382, 1996.

[67] T. Staudt, M.C. Lang, R. Medda, J. Engelhardt, and S.W. Hell. 2,2'-Thiodiethanol: A new water soluble mounting medium for high resolution optical microscopy. *Microsc. Res. Tech.*, 70(1):1–9, 2007.

[68] J.A. Aten, J. Stap, P.M. Krawczyk, C.H. van Oven, R.A. Hoebe, J. Essers, and R. Kanaar. Dynamics of DNA Double-Strand Breaks Revealed by Clustering of Damaged Chromosome Domains. *Science*, 303(5654):92–95, 2004.

[69] T. Neumaier, J. Swenson, C. Pham, A. Polyzos, A.T. Lo, P. Yang, J. Dyball, A. Asaithamby, D.J. Chen, M.J. Bissell, S. Thalhammer, and S.V. Costes. Evidence for formation of DNA repair centers and dose-response nonlinearity in human cells. *Proc. Natl. Acad. Sci. USA*, 109(2):443–448, 2011.

[70] T.C. Karagiannis, K.N. Harikrishnan, and A. El-Osta. Disparity of histone deacetylase inhibition on repair of radiation-induced DNA damage on euchromatin and constitutive heterochromatin compartments. *Oncogene*, 26(27):3963–3971, 2007.

[71] I.G. Cowell, N.J. Sunter, P.B. Singh, C.A. Austin, B.W. Durkacz, and M.J. Tilby. Gamma-H2AX Foci Form Preferentially in Euchromatin after Ionising-Radiation. *PLoS One*, 2(10):e1057, 2007.

[72] L. Hlatky. Double-strand break motions shift radiation risk notions? *Proc. Natl. Acad. Sci. USA*, 109(2):351–352, 2012.

[73] M. Niklas. Imaging and quantifying the migration and cellular divisions in the developing lateral line of the zebrafish. Master's thesis, University of Heidelberg, 2010.

[74] R.M. Martin, H. Leonhardt, and M.C. Cardoso. DNA labeling in living cells. *Cytom. Part A*, 67(1):45–52, 2005.

List of Figures

List of Tables

Appendices

A

Materials for cell biology

Table A1: Important consumables for engineering Cell-Fit-HD. Standard consumables for cell culture are not listed.

Consumables	**Company and Cat. No.**
Parafilm M®, all-purpose laboratory film, 4In. x 125Ft.	Pechiney Plastic Packaging Inc., USA, Cat. No. PM996
24 well cell culture multiwell plate, CELLSTAR®	Greiner Bio-One GmbH, Germany, Cat. No. 662102

Table A2: Important chemicals for engineering Cell-Fit-HD.

Chemicals	**Company and Cat. No.**
Albumin Fraktion V, (BSA)	Carl ROTH, Germany, Cat. No. 8076.2
Bovine fibronectin, without bovine serum albumin	R&D Systems, USA, Cat. No. 1030-FN-01M
Dulbecco's phosphate buffered salt solution (DPBS)	PAN Biotech GmbH, Germany, Cat. No. P04-36500
Fetal Bovine Serum (FBS)	Biochrom AG, Germany, Cat. No. S 0615
Penicillin-Streptomycin	Life Technologies, USA, Cat. No. 15140-122
Triton X-100	Roche Diagnostics, Cat. No. 11332481001
Trypan blue solution	Sigma-Aldrich Co. LLC, USA, Cat. No. T8154
Trypsin-EDTA solution	PAN Biotech GmbH, Germany, Cat. No. P10-023100
UltraPure ™ Agarose	Life Technologies, USA, Cat. No. 16500500

Table A3: Commercial staining kits used for the biological compartment.

Chemicals	**Company and Cat. No.**
Albumin Fraktion V, (BSA)	Carl ROTH, Germany, Cat. No. 8076.2
Bovine fibronectin, without bovine serum albumin	R&D Systems, USA, Cat. No. 1030-FN-01M
Dulbecco's phosphate buffered salt solution (DPBS)	PAN Biotech GmbH, Germany, Cat. No. P04-36500
Fetal Bovine Serum (FBS)	Biochrom AG, Germany, Cat. No. S 0615
Penicillin-Streptomycin	Life Technologies, USA, Cat. No. 15140-122
Triton X-100	Roche Diagnostics, Cat. No. 11332481001
Trypan blue solution	Sigma-Aldrich Co. LLC, USA, Cat. No. T8154
Trypsin-EDTA solution	PAN Biotech GmbH, Germany, Cat. No. P10-023100
UltraPure ™ Agarose	Life Technologies, USA, Cat. No. 16500500

Table A4: Antibodies used for immunofluorescence staining.

Antibodies	**Company and Cat. No.**
Glucose transporter Glut1 primary antibody	Abcam®, UK, Cat. No. ab652
Phospho-histone-specific primary antibody 100X	Cell Biolabs, USA, Part No. 232101
Secondary antibody Alexa Fluor 488 goat anti-mouse IgG conjugate	Molecular Probes®, Life Technologies, USA, Cat. No. A-11029
Secondary antibody Alexa Fluor 555 goat anti-mouse IgG conjugate	Molecular Probes®, Life Technologies, USA, Cat. No. A-21422

Table A5: Cell culture media. All culture media were supplemented with 10% FBS and 1% penicillin-streptomycin. All media were stored at 4°C until use.

Culture media	**Company and Cat. No.**
DMEM/Ham's F-12 liquid medium	Biochrom AG, Germany, Cat. No. FG 4815
Dulbecco's modified Eagle medium (DMEM)	Biochrom AG, Germany, Cat. No. FG 0415
Roswell Park Memorial Institute (RPMI) 1640 medium	Biochrom AG, Germany, Cat. No. FG 1215

Table A6: Human and murine cell lines used for the cell coating of the FNTD. PC3, A549 and A431 cells were obtained from Deutsche Sammlung von Mikroorganismen und Zellkulturen (DSMZ, Germany), U87 cells were obtained from American Type Culture Collection (ATCC, USA) and SMA-560 cells were kindly donated by Dr. Wolfgang Wick, Clinical Cooperation Unit Neurooncology, German Cancer Research Center, Heidelberg, Germany.

Human and murine cell lines
Human epidermoid carcinoma (A431) cells
Human glioblastoma (U87) cells
Human lung adenocarcinoma epithelial (A549) cells
Human prostate cancer (PC3) cells
Murine astrocytoma (SMA-560) cells

Photon-dose response correction

Photon-dose response correction was applied for the FNTD read-out signal only for doses greater than 50 Gy. Below this threshold the read-out signal was assumed to be linearly rising with increasing dose. The saturation dose was 83.3 Gy [39]. The response correction was computed with libamtrack [24].

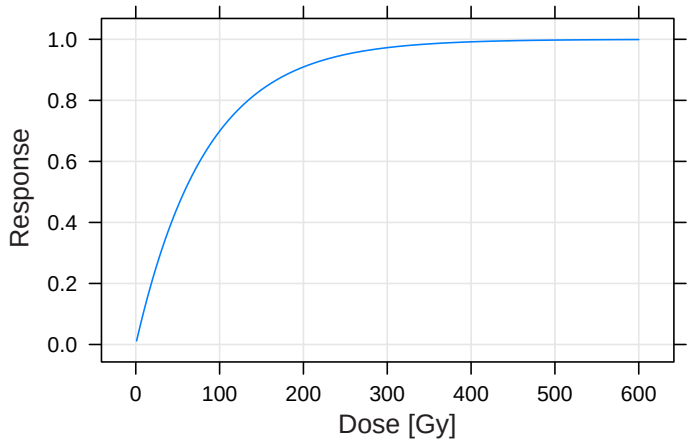

Figure A1: Photon-dose response curve of the FNTD.

Survival distribution

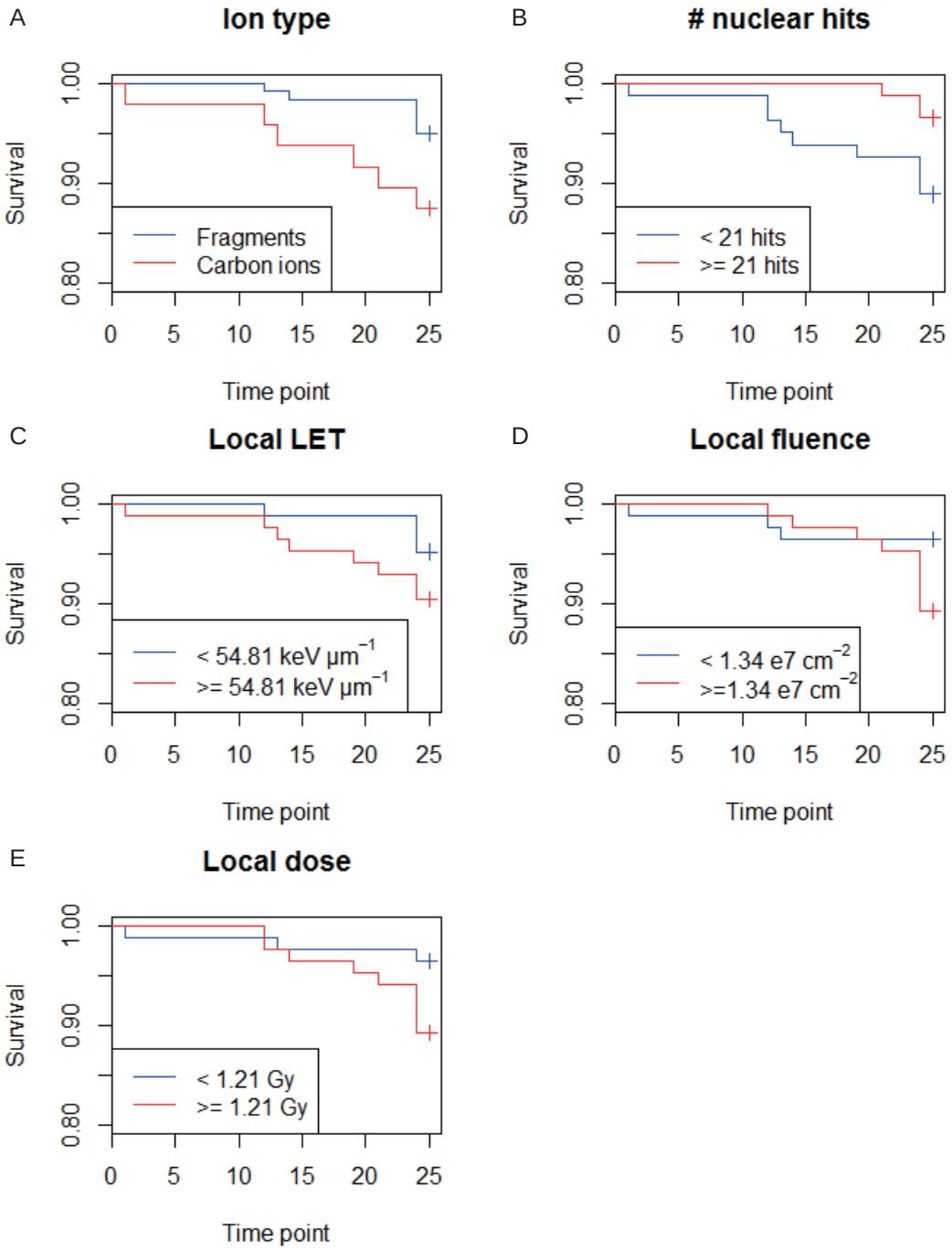

Figure A2: Survival curves. Survival was defined as (1- apoptotic index). The cells were grouped according to the median of the microscopic beam parameters assessed in the nucleus. Survival was calculated for each sub-group. (A) Cells were also categorized whether their nucleus was primarily traversed by carbon ions or lighter fragments. Time point 0 refers to the actual irradiation. Imaging started 1 h after irradiation (time point 1). The time interval between two consecutive time points was approximately 45 min. The total imaging time was approximately 19 h. Cells which were still alive in the last imaging time point were censored (indicated by the crosses).

B

Radiation Measurements 56 (2013) 285–289

Contents lists available at SciVerse ScienceDirect

Radiation Measurements

journal homepage: www.elsevier.com/locate/radmeas

Spatial correlation between traversal and cellular response in ion radiotherapy – Towards single track spectroscopy

M. Niklas [a,*], C. Melzig [b], A. Abdollahi [b,c], J. Bartz [d,e], M.S. Akselrod [e], J. Debus [f,g], O. Jäkel [a,f,g], S. Greilich [a]

[a] German Cancer Research Center (DKFZ), Division of Medical Physics in Radiation Oncology, Im Neuenheimer Feld 280, 69120 Heidelberg, Germany
[b] Molecular & Translational Radiation Oncology, Heidelberg Ion Therapy Center (HIT), University of Heidelberg Medical School and National Center for Tumor Diseases (NCT), German Cancer Research Center (DKFZ), Im Neuenheimer Feld, 69120 Heidelberg, Germany
[c] Center of Cancer Systems Biology, Nasa Specialized Center of Research (NSCOR), St. Elizabeth's Medical Center, Tufts University School of Medicine, Boston, MA, USA
[d] Oklahoma State University, Physics Department, Stillwater, OK 74078-3072, USA
[e] Landauer Inc., Stillwater Crystal Growth Division, Stillwater, OK 74074, USA
[f] Heidelberg University Hospital, Department of Radiation Oncology, Im Neuenheimer Feld 400, 69120 Heidelberg, Germany
[g] Heidelberg Ion-Beam Therapy Center (HIT), Im Neuenheimer Feld 450, 69120 Heidelberg, Germany

HIGHLIGHTS

- We parameterized the intensity profile of a single ion gained by the FNTD read-out.
- Maximum intensity signal of acquired FNTD images seems to be a surrogate for LET.
- FWHM of intensity profile is a limited measure for the maximum sec. electron range.
- FNTD were read out by STED microscopy with a resolution beyond diffraction limit.

ARTICLE INFO

Article history:
Received 15 October 2012
Received in revised form
16 January 2013
Accepted 25 January 2013

Keywords:
Fluorescent nuclear track detector
Particle irradiation
Radiation imaging
Single track spectroscopy
Track structure

ABSTRACT

Knowledge about the mechanisms linking physical energy deposition and biological response in ion cancer beam therapy and space research is still limited. We sought to develop a novel detector system based on fluorescent nuclear track detector (FNTD) covered with a viable cell-layer to gain spatial correlation between ion traversal and cellular damage on a μm scale. We investigated the possibility to gain, in addition to track location, information on ion type and energy from a single particle track by the FNTD read-out. To access both parameters we aimed to find surrogates for the local energy transfer (LET) of the incident ion and the maximum secondary electron range in the detector material as those quantities are related to the ion type and energy. We parametrized the intensity profile of the fluorescent signal of a single ion by the maximum intensity signal and full width half maximum (FWHM). The first seems to be a suitable surrogate for the LET of the incident particle whereas the latter is only a limited measure for the maximum secondary electron range in detector material.

1. Introduction

To understand the fundamental molecular mechanisms of ion radiotherapy, colocalisation studies of energy deposition and cellular response are of essential importance. A lack of sensitive biocompatible detectors providing sufficient information on physical beam parameters and biological damage hampers these studies. We are therefore developing a novel cell/fluoresecent-crystal hybrid-detector. It is based on a biocompatible, fluorescent nuclear track detector (FNTD, Fig. 1A) (Akselrod and Sykora, 2011) and a cell layer on the inert detector surface. It enables a co-detection of the tracks of traversing ions and the subsequent biological damage in the cell layer after particle irradiation on a μm scale (Fig. 1B, unpublished results). The detector and the cell layer in situ are read-out by the very same commercial confocal laser scanning microscope (CLSM).

Here we present a first investigation on the feasibility to extract, in addition to track location and direction, information on ion type and energy from a single particle track. To obtain this information, simultaneous measurements of local energy transfer (LET) and the maximum range of the secondary electrons in the detector material

* Corresponding author. Tel.: +49 6221 422633.
E-mail address: m.niklas@dkfz.de (M. Niklas).

1350-4487/$ – see front matter © 2013 Elsevier Ltd. All rights reserved.
http://dx.doi.org/10.1016/j.radmeas.2013.01.060

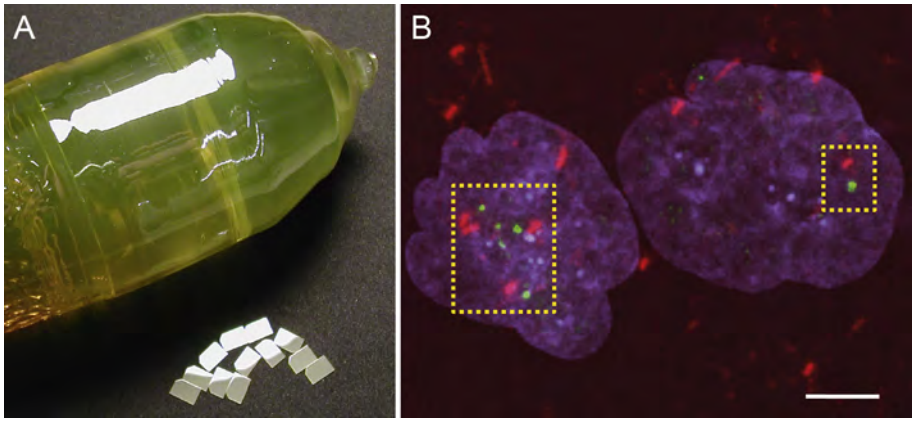

Fig. 1. Photo of the Al_2O_3:C,Mg crystal and FNTD detectors cut from it (A) and fluorescent image (B) illustrating spatial correlation (dashed rectangle) between single ion traversal and cell damage. FNTD was coated with confluent lung caner (A549) cell layer. Spatial correlation (maximum intensity z projection) between single carbon ion traversals (red spots) and subsequent DNA double strand breaks (γ-H2AX, immunofluorescent staining, green spots). Cell nuclei are labeled in blue (HOECHST staining). Scale bar, 5 μm. (For interpretation of the references to colour in this figure legend, the reader is referred to the web version of this article.)

seem to be most reasonable, as those quantities are related to the ion type and energy via the shape of the radial dose distribution.

In order to assess both LET and maximum range from acquired FNTD images we investigated in this paper the suitability of the following parameters: maximum intensity signal, full width half maximum (FWHM) and background of the intensity profile of the fluorescence signal in an ion track by a) direct measurement and b) by fitting a two-dimensional Gauss-curve to the track intensity data and extracting its parameters.

2. Materials and methods

2.1. Al_2O_3:C,Mg based FNTDs

FNTD alumina crystal lattice is doped with magnesium and carbon ions creating fluorescent color centers F_2^{2+}(2Mg) (Akselrod and Sykora, 2011). By exposing the detector to ionizing radiation these aggregate defects undergo radiochromic transformation. The altered color centers absorb light in the band centered at 620 nm, prompting fast 750 nm fluorescence. F_2^{2+}(2Mg) color centers can be excited at 435 nm optical absorption band and emit fluorescent light at 515 nm. FNTDs are sensitive for ions with LET > 0.5 keV/μm (Osinga et al., 2013). They have very high detection efficiency close to 100% for entire spectrum of primary particles and fragments at energies found in ion-beam cancer therapy (Osinga et al., 2013).

2.2. Irradiation of FNTDs

For a reference data set, FNTDs were irradiated with monoenergetic beams of particles from a wide range of ion types and energies (Table 1). The detector surfaces were thereby always aligned perpendicularly towards the incident beam. Irradiations were performed with the therapy beam of the Heidelberg Ion Beam Therapy Center (HIT) at Heidelberg University Hospital, Germany, at RADiation Effects Facility RADEF at the University of Jyvaeskylae, Finland, at SNAKE, Maier-Leibnitz-Laboratorium, Munich, Germany, and at the Max Planck Institute for Nuclear Physics in Heidelberg, Germany. For high energy irradiation we placed the detector in the entrance channel of the ion beam. Low energy irradiations were performed in vacuum.

2.3. Confocal read-out of FNTD

For the detector read-out we used the CLSM 710, Confocor 3 (Zeiss) equipped with a z-piezo stage, 63x/1.45 NA (numerical aperture) Oil DIC M27 objective, APD/PMT/T-PMT detection. We used the protocol as described in (Greilich et al., in this issue). The excitation laser power was adjusted to avoid saturation of the APD ($p = 86\%$, 633 nm Helium–Neon laser). Pixel dwell time τ was set to 89,6 μs and the line-scanning repetition R was limited to 4. A single imaging field comprised 1152x1152 pixel with a pixel size of 0.117 μm to meet the Nyquist criterion. The microscope detector pinhole aperture was set to 1 Airy disk unit (AU). The read-out depth was adjusted to approx. 30 μm measured from the detector surface. For Mg-24, S-32, Fe-56, Kr-84 and Xe-131 ions the read-out depth was limited to 10 μm as the traversing ions stopped in the FNTD after approximately 30 μm. For imaging, the FNTD was placed in uncoated glass bottom dish (MatTek Corp.). Zeiss Immersol™518 F was used as an immersion fluid. Due to saturation effects of the APD the detected count-rate $\eta_{detected}$ (fluorescence signal N is converted into count-rate η by $\eta = N/(R\cdot\tau)$) was converted into the actual rate η_{actual} by $\eta_{actual} = -\eta_0 \cdot \ln(1-\eta_{detected}/\eta_0)$ with an average saturation rate η_0 of 18 MHz.

2.4. Image processing

We extracted and subtracted the inhomogeneous background of all acquired images using the histogram-based Mosaic background

Table 1
Particle spectrum for FNTD irradiation. Ions with energies labeled with * were irradiated in vacuum. LET and e− range values in alumina were calculated using libamtrack (Greilich et al., 2010).

Particle type	Energy [MeV/u]	LET in Al2O3 [keV/μm]	Max. sec. e^- range in Al2O3 [μm]
H-1	3.00*, 6.00*, 12.00*, 21.00*, 49.37	34.64, 20.79, 12.27, 7.90, 4.00	0.08, 0.26, 0.86, 2.23, 9.53
C-12	4.00*, 91.14, 114.60, 152.05, 224.81, 428.77	951.80, 90.23, 76.92, 62.68, 48.59, 34.42	0.13, 27.02, 39.88, 64.50, 125.39, 375.80
Mg-24	4.00*	3203.60	0.13
S-32	3.13*	5 524,17	0.09
Fe-56	5.19*, 9.30*	9457.75, 7517.21	0.21, 0.56
Kr-84	9.30*	12 337.28	0.56
Xe-131	5.50*, 9.30*	24 246.50, 21 687.85	0.23, 0.56

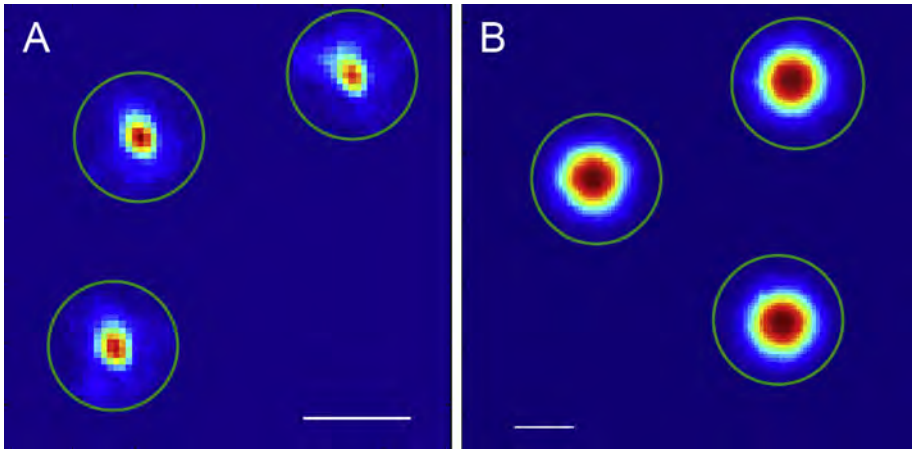

Fig. 2. FNTD read out signal of (A) C-12 91.14 Mev/u and (B) Xe-131 9.30 MeV/u irradiation. The track core is encoded by dark red. The track spots were masked with a disk of radius 10 (A) and 20 (B) pixel. Pixels outside the disk are set to zero. Scale bar, 2 μm. (For interpretation of the references to colour in this figure legend, the reader is referred to the web version of this article.)

Table 2
Parameters extracted from the intensity profile of a track-spot by direct measurements and by a 2D Gaussian fit.

Direct measurements	
$\widehat{\eta}$	Absolute max. count rate
FWHM	Full width half maximum of a track spot
2D Gaussian fit	
$\widehat{A}$	Gaussian peak amplitude
σ	Gaussian peak width
B	Small-scale background

subtractor (Cardinale, 2010) with a sliding window of length 15. The track spots were identified using the Mosaic particle tracker (Helmuth et al., 2009) with following parameters: radius (cut-off): 3 pixel (0.3), the percentile varied between 0.01 and 0.3. For Xe-131 radius was set to 6 pixel. To define a region of interest (ROI) all identified track spot centers (x_0,y_0) were masked by a disk of radius r_d with $5 \le r_d \le 20$ pixel (Fig. 2). To exclude incomplete or overlapping track spots the area of the ROI had to be in the interval $[0.95\cdot r_d^2\pi; 1.3\cdot r_d^2\pi]$. For the analysis of the intensity profile of a track spot (Table 2) all pixels within the ROI were considered. For each selected track spot the maximum count-rate $\widehat{\eta}$ was extracted and the FWHM of the count-rate distribution was computed by

$$\mathrm{FWHM} = \sqrt{4A_{\mathrm{FW}}/\pi}. \tag{1}$$

It is the diameter of a circle with the area A_{FW} of all pixels with $\eta \ge 0.5\cdot\widehat{\eta}$. The selected track spots were also fitted by a 2D symmetrical Gauss function

$$\eta(x,y,A,\sigma,B) = A/\left(2\pi\sigma^2\right)\cdot\exp\Big(-0.5/\sigma^2\Big((x-x_0)^2 + (y-y_0)^2\Big)\Big) + B \tag{2}$$

with the peak value $\widehat{A} = A/(2\pi\sigma^2)$ and a constant term B accounting for small-scale background not subtracted by the initial

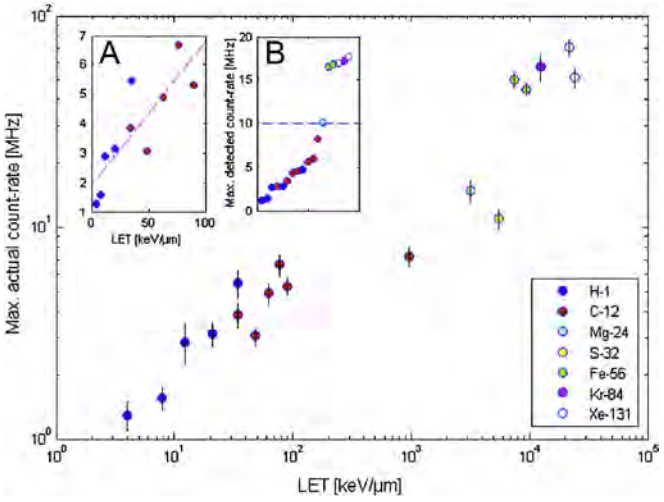

Fig. 3. Correlation between the mean maximum actual count rate $\widehat{\eta}_{\mathrm{actual}}$ of a track spot and LET of the incident particle. The error bars show the standard deviation. The disk radius for the track-spot masking is 15 pixel for all particle types and energies. Inserts: (A) fitting of H-1 and C-12 count-rates (except C-12 4 MeV/u) by a straight line. (B) Mean maximum detected count rates $\widehat{\eta}_{\mathrm{detected}}$ sorted in ascending order. Above 10 MHz saturation effects occur.

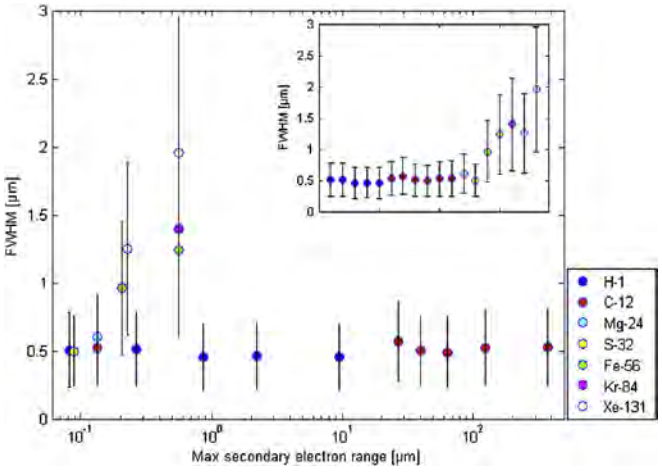

Fig. 4. Correlation between the mean FWHM of a track spot (η_{detected}) and the maximum secondary electron range as a measure for the energy of the incident particles. The error bars show the standard deviation. The disk radius for the track-spot masking is 15 pixel for all particle types and energies. There seems to be a linear relationship for track spots with a FWHM >0.5 μm. Insert: mean FWHM sorted in ascending order.

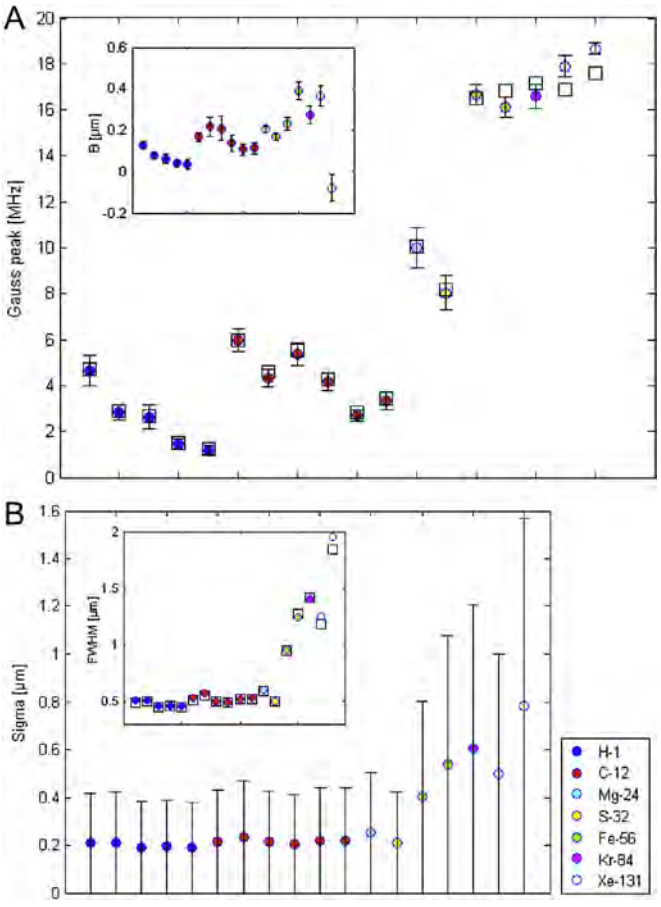

Fig. 5. Fit results gained by 2dim Gauss fitting of the track spots ($\eta_{detected}$). Values of the mean Gaussian peak amplitude $\widehat{A}$ and mean σ are sorted in ascending order with respect to the atomic number and energy of the incident particle. (A) The value of $\widehat{A}$ is declining with increasing energy within a particle type. Insert: the background B is rising with increasing atomic number. (B) Mean σ is nearly constant for ions lighter than Fe-56. Insert: The corresponding mean FWHM gained by the fit nearly coincides (except Xe-131) with the mean FWHM gained by track spot characterisation.

background correction. FWHM and σ are related by FWHM $= 2\sqrt{2\ln 2}\cdot\sigma$.

For each particle irradiation approximately 100–200 track spots were analyzed.

3. Results

3.1. Direct measurement: $\widehat{\eta}$ and FWHM

In Fig. 3 the mean maximum count-rate $\widehat{\eta}_{actual}$ is correlated to the LET of the incident ion. In general the count-rate is increasing with rising LET – it follows an approximately exponential function (Sykora et al., 2008). Insert B shows the mean $\widehat{\eta}_{detected}$, sorted in ascending order. Above 10 MHz significant saturation effects occur (Greilich et al., in this issue), leading to great discrepancy between $\eta_{detected}$ and η_{actual}. The detected and actual rates for Fe-56, Kr-84 and Xe-131 ions have therefore to be considered with some reservation. In the LET interval [0; 100 keV/µm] a linear relationship can be assumed to a first approximation, applying simple linear regression analysis (insert A). In this interval, a mean variation of the actual count-rate of 10% (mean standard deviation of $\widehat{\eta}_{actual}$ for H-1 and C-12) translates into a LET uncertainty of about 14%.

In Fig. 4 the mean FWHM of the track spots is plotted against the maximum secondary electron range in alumina. There seems to be a linear trend for track spots with a FWHM greater than 0.5 µm. For the lighter ions (H-1 and C-12) there is no tendency for the FWHM to increase with increasing particle energy. Concerning Fe-56 and Xe-131 the FWHM is increasing with increasing energy of the incident particle.

3.2. 2D Gaussian fit

We fitted the distribution of $\eta_{detected}$ of a track spot by a 2dim Gaussian function to get an estimation of the net count-rate. Following disk mask radii seemed to be most suitable: 10 pixel (H-1 and C-12), 15 pixel (Mg-24 and S-32) and 20 pixel (Fe-56, Kr-84 and Xe-131). These radii ensure a suitable trade-off between sufficient background signal (characterized by the constant background term B) in the ROI and not to exclude too many track spots by overlapping ROIs. Fig. 5 shows the mean Gaussian peak amplitude $\widehat{A}$ and corresponding mean σ of the fitted track-spots. Within a single particle type the count rates are sorted in ascending order with respect to the energy of the incident ion (Fig. 5A). It is obvious

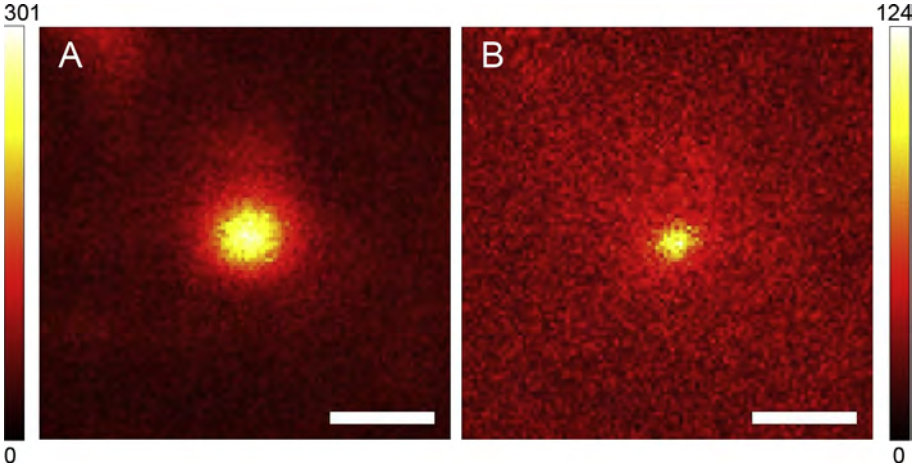

Fig. 6. Fluorescent images of a carbon ion track using confocal (A) and STED (B) microscopy after irradiation perpendicular to the detector surface. The pixel intensities of both image planes were scaled to the corresponding maximum. The diameter of a track spot could be reduced by a factor of two by the STED read-out. Scale bar, 572 nm. Courtesy of M. Henrich and J. Engelhardt, Division of Optical Nanoscopy, DKFZ, Heidelberg.

(except Xe-131) that within a particle type $\widehat{A}$ is declining with rising particle energy (and hence declining LET). Except Mg-24 and S-32 $\widehat{A}$ is also rising with increasing atomic number of the incident ion. The solid rectangles show the corresponding mean $\widehat{\eta}_{\text{detected}}$ gained by track spot geometry analysis. Except for Xe-131 the values obtained by the Gaussian fit and the ones obtained by track spot analysis coincide. There is also a tendency that with rising atomic number (and rising disk mask radius) background pedestal (B) is increasing (insert, Fig. 5A).

For H-1 – S-32 ions σ hardly varies (Fig. 5B) but there is a significant increase of σ and corresponding FWHM (insert, Fig. 5B) for particles heavier than S-32. Again, except for Xe-131 the FWHM values coincide with the FWHM values (solid rectangles) obtained from track spot geometry analysis.

4. Discussion

Both maximum count-rate $\widehat{\eta}$ and Gaussian peak amplitude $\widehat{A}$ are rising with increasing LET of the incident particle (Figs. 3 and 5A). Due to a different read-out depth of 10 μm and 30 μm the actual $\widehat{\eta}$ (and $\widehat{A}$)-LET dependency could differ slightly especially for the low energy particles. Within this depth the incident particles are interacting with the alumina and therefore loosing kinetic energy. Also, color center concentration inhomogeneity between FNTD crystals can cause small variations in $\widehat{\eta}$ and $\widehat{A}$ interfering the comparability (and reproducibility) and hence the actual LET dependency.

A broadening of the track spot by the point spread function (PSF) of the imaging system masks the actual FWHM-secondary electron range dependency (Fig. 4). For particles with a track spot diameter $\leq$0.5 μm the diameter of the PSF seems to dominate (insert, Fig. 4).

The mismatch between detected and fitted maximum count rates ($\widehat{\eta}$ and $\widehat{A}$) and the calculated and fitted FHWM for heavier ions (Fig. 5) could mainly be caused by the increasing track-spot penumbra and detection saturation effects.

5. Conclusion

We characterized the single ion's signature by its maximum fluorescence intensity (characterized by the APD count rate) and the track size (characterized by FWHM of the Gaussian fit of the track intensity distribution) to obtain a quantitative dependence for measuring ion's LET as well as maximum secondary electron range and hence retrieve information on ion type and energy. The maximum count-rate, whether detected or obtained by Gaussian fit seems to be a suitable parameter to measure the LET of the incident particle. Concerning the clinically relevant LET range [0; 100 keV/μm] we are already able to translate the detected read-out signal into a LET value with an uncertainty of approximately 14% and hence retrieve information on the energy of the incident ion. The FWHM (obtained by direct measurement or Gaussian fit) however seems to correlate with the maximum secondary electron range only for ions heavier than C-12. Nanoscopic analysis beyond diffraction limit by Stimulated Emission Depletion Microscopy (STED) (Hell, 2007) (Fig. 6) could help to increase resolution by decreasing the diameter of the PSF and hence make important progress in the track structure characterisation.

Acknowledgments

The author would like to thank S. Brons for generously providing support and technical irradiation assistance at the Ion-Beam Therapy Center of Heidelberg University Hospital. We would also like to thank F. Bestvater and M. Brom of the DKFZ's light microscopy core facility for their enthusiasm and unflagging support and acknowledge B. Hartmann for her involvement in scientific discussions. We would like to thank M. Heinrich and J. Engelhardt for the read-out by STED microscopy. M.N. is funded by the fellowship from the Helmholtz International Graduate School for Cancer Research at the German Cancer Research Center. C.M. is supported by the University of Heidelberg. S.G. and A.A. are supported by the German Cancer Research Center. J.D. and O.J. are supported by the University Hospital Heidelberg. M.A. is supported by Landauer R&D money. J.B. is supported by Oklahoma State University. This work was supported by the Helmholtz Association (Translating hadron therapy from basic research to clinical application, VH-VI-303, S.G.), German Research Council (DFG, KFO214), National Aeronautics and Space Administration under NSCOR grant no. NNJ06HA28G, the German Krebshilfe (Deutsche Krebshilfe, Max-Eder 108876), intramural Grants of the National Center for Tumor diseases (NCT, Heidelberg, Germany) and the German Federal Ministry of Research and Technology (Bundesministerium für Bildung und Forschung – BMBF 03NUK004C). The authors declare that they have no competing financial interests.

References

Akselrod, M., Sykora, G., 2011. Fluorescent nuclear track detector technology – a new way to do passive solid state dosimetry. Radiat. Meas. 46, 1671–1679.

Cardinale, J., 2010. Histogram-based Background Subtractor for ImageJ. Technical Report. MOSAIC Group, ETH Zuerich, Switzerland.

Greilich, S., Grzanka, L., Bassler, N., Andersen, C.E., Jäkel, O., 2010. Amorphous track models: a numerical comparison study. Radiat. Meas 45, 1406–1409.

Greilich, S., Osinga, J.M., Niklas, M., Lauer, F., Klimpki, G., Bestvater, F., Bartz, J., Akselrod, M., Jäkel, O., 2013. Fluorescent nuclear track detectors as a tool for ion-beam therapy research. Radiat. Meas. 56, 267–272.

Hell, S.W., 2007. Far-field optical nanoscopy. Science 316, 1153–1158.

Helmuth, J.A., Burckhardt, C.J., Greber, U.F., Sbalzarini, I.F., 2009. Shape reconstruction of subcellular structures from live cell fluorescence microscopy images. J. Struct. Biol. 167, 1–10.

Osinga, J.M., Akselrod, M., Herrmann, R., Hable, V., Dollinger, G., Jäkel, O., Greilich, S., 2013. High-accuracy fluence determination in ion beams using fluorescent nuclear track detectors. Radiat. Meas. 56, 294–298.

Sykora, G., Akselrod, M., Benton, E., Yasuda, N., 2008. Spectroscopic properties of novel fluorescent nuclear track detectors for high and low let charged particles. Radiat. Meas. 43, 422–426.

C

RADIATION ONCOLOGY

METHODOLOGY Open Access

Engineering cell-fluorescent ion track hybrid detectors

Martin Niklas[1,2*], Steffen Greilich[1,2], Claudius Melzig[2,3,4,5], Mark S Akselrod[6], Jürgen Debus[2,3,4,5], Oliver Jäkel[1,2,4,5] and Amir Abdollahi[2,3,4,5,7]

Abstract

Background: The lack of sensitive biocompatible particle track detectors has so far limited parallel detection of physical energy deposition and biological response. Fluorescent nuclear track detectors (FNTDs) based on Al_2O_3:C,Mg single crystals combined with confocal laser scanning microscopy (CLSM) provide 3D information on ion tracks with a resolution limited by light diffraction. Here we report the development of next generation cell-fluorescent ion track hybrid detectors (Cell-Fit-HD).

Methods: The biocompatibility of FNTDs was tested using six different cell lines, i.e. human non-small cell lung carcinoma (A549), glioblastoma (U87), androgen independent prostate cancer (PC3), epidermoid cancer (A431) and murine (VmDk) glioma SMA-560. To evaluate cell adherence, viability and conformal coverage of the crystals different seeding densities and alternative coating with extracellular matrix (fibronectin) was tested. Carbon irradiation was performed in Bragg peak (initial 270.55 MeV u^{-1}). A series of cell compartment specific fluorescence stains including nuclear (HOECHST), membrane (Glut-1), cytoplasm (Calcein AM, CM-DiI) were tested on Cell-Fit-HDs and a single CLSM was employed to co-detect the physical (crystal) as well as the biological (cell layer) information.

Results: The FNTD provides a biocompatible surface. Among the cells tested, A549 cells formed the most uniform, viable, tightly packed epithelial like monolayer. The ion track information was not compromised in Cell-Fit-HD as compared to the FNTD alone. Neither cell coating and culturing, nor additional staining procedures affected the properties of the FNTD surface to detect ion tracks. Standard immunofluorescence and live staining procedures could be employed to co-register cell biology and ion track information.

Conclusions: The Cell-Fit-Hybrid Detector system is a promising platform for a multitude of studies linking biological response to energy deposition at high level of optical microscopy resolution.

Background

To better understand the molecular mechanisms governing the radiobiological effects of particle therapy or space radiation simultaneous detection of cellular response and physical energy deposition is desired. Moreover, the growing field of particle therapy using protons and heavier ions (e.g. carbon) urgently needs novel means of biological dosimetry to accurately account for difference in relative biological effectiveness (RBE) [1], as a function of a plethora of particle variables such as location of ion traversal, ion type, energy and linear energy transfer (LET).

Earlier approaches to correlate physical radiation parameters with biological endpoints like cell survival (e.g. BIOSTACK experiment [2,3] and cell-coated CR39 detectors [4]) were hindered by a limited set of physical parameters that could be obtained. In addition, inability to autoclave the detector before cell deposition hindered the sterile cell cover.

Here we devise a novel strategy to establish a cell-fluorescent ion track hybrid detector (Cell-Fit-HD) based on fluorescent nuclear track detectors (FNTDs, Figure 1a). FNTDs based on Al_2O_3:C,Mg single crystals provide almost 100% detection efficiency of ion tracks imaged by confocal laser scanning microscope (CLSM) [5,6].

*Correspondence: m.niklas@dkfz-heidelberg.de
[1]Division of Medical Physics in Radiation Oncology, German Cancer Research Center, INF 280, 69120 Heidelberg, Germany
[2]German Cancer Consortium (DKTK), National Center for Radiation Research in Oncology, Heidelberg Institute of Radiation Oncology, INF450/400, Heidelberg, Germany
Full list of author information is available at the end of the article

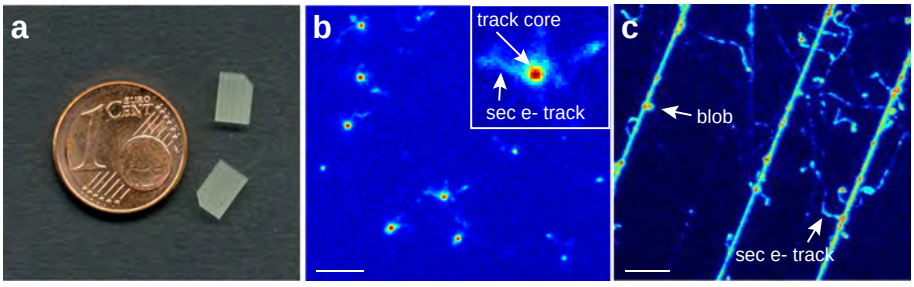

Figure 1 Fluorescent nuclear track detector (FNTD). (a) Two FNTDs ($8 \times 4 \times 0.5$ mm^3). Courtesy of M.S. Akselrod, Landauer Crystal Growth Division. **(b)** Fluorescent image of the 270.55 MeV u^{-1} carbon-ion tracks propagating perpendicular to the FNTD crystal surface. The brightest spots (physical energy deposition events) are attributed to carbon ions with a full width half maximum (FWHM) of approximately 500 nm [9]. The smaller, less intense spots to less densely ionizing particles like protons. The small structures around the carbon ion tracks arise from secondary electrons (sec e-) [10]. Insert: magnification of a single track spot. The track core is encoded by dark red. Scale bar, 5 μm. **(c)** FNTD image after carbon irradiation (initial 270.5 MeV u^{-1}) parallel to the polished crystal surface. Secondary electron structures (small trajectories branching from the ion track) are visible. Instead of homogeneous energy deposition discrete blobs (bright spots) occur along the particle tracks. This is an illustration of stochastic nature of energy deposition along the heavy charged particle track. Courtesy of F. Lauer. Scale bar, 5 μm.

3D information on energy deposition of ion tracks was obtained with diffraction-limited resolution and a multitude of physical parameters derived, such as location, direction, and possibly particle type and LET [6-9].

To develop the Cell-Fit-HD, the Al_2O_3:C,Mg crystal was autoclaved and coated with different human and murine cell lines to form a cell-crystal hybrid sample. We report here the successful development of protocols to grow human and murine cells on FNTDs to create a viable cell layer. To evaluate potential spectrum of applications for Cell-Fit-HD, we successfully tested different staining and fixation protocols for co-detection of different biological compartments and radiation particles parameters. Here, we demonstrate the feasibility of sequential read-out of the physical and biological information using CLSM without removing the cell layer from the Al_2O_3:C,Mg single crystal. The Cell-Fit-HD technology may provide a novel tool for of spatial correlation between biological readouts and single ion traversals.

Methods

Al_2O_3:C,Mg based FNTDs

The FNTDs are made of aluminum oxide single crystals doped with magnesium and carbon ions (α-Al_2O_3:C,Mg). The fluorescent color centers in these crystals are F_2^{2+}(2Mg)-centers. They are the aggregate defects formed by two oxygen vacancies and two Mg-ion impurities [6]. Pristine F_2^{2+}(2Mg) color centers can be excited at 435 nm optical absorption band and emit fluorescent light at 520 nm. By exposing the detector to ionizing radiation, secondary electrons are generated, captured by the defects and transform them into F_2^{+}(2Mg) color centers. The radiation-transformed color centers have different optical properties: they absorb light in a band centered at 620 nm light, prompting fast 750 nm fluorescence. The intensity of this radiation-induced 750 nm fluorescence depends on local energy deposition of ionizing radiation. Accordingly, FNTDs allow for high spatial resolution particle track visualization by confocal microscopy [6] (Figure 1b,c) and subsequent 3D particle track reconstruction [7,11]. The system is sensitive for ions with LET $>$ 0.5 keV μm^{-1} [5,8]. FNTD offers a detection efficiency close to 100% for the entire spectrum of primary particles and fragments at energies found in ion beam cancer therapy [5]. The current limit of maximum accessible track fluence is in the range of $5 \cdot 10^7$ cm^{-2} [5], relevant to fluences providing clinical doses.

Cell cultures and characterization

All cells and Cell-Fit-HD were cultured in humidified atmosphere under standard culture conditions (37°C, 5% CO_2). Human lung adenocarcinoma epithelial (A549) and human glioblastoma (U87) cells were cultured in Dulbecco's modified Eagle medium (DMEM, Biochrom AG, Berlin, Germany, Cat. No. FG 0415). Human epidermoid carcinoma (A431) and human prostate cancer (PC3) cells were cultured in Roswell Park Memorial Institute (RPMI) 1640 medium (Biochrom AG, Cat. No. FG 1215). Murine astrocytoma (SMA-560) cells were cultured in DMEM/Ham's F-12 liquid medium (Biochrom AG, Cat. No. FG 4815). All culture media were supplemented with 10% Fetal Bovine Serum (FBS, Biochrom AG, Cat. No. S 0615) and 1% penicillin- streptomycin.

PC3, A549 and A431 cells were obtained from Deutsche Sammlung von Mikroorganismen und Zellkulturen (DSMZ, Braunschweig, Germany), U87 cells were obtained from American Type Culture Collection (ATCC) and SMA-560 was kindly donated by Dr. Wolfgang Wick, Clinical Cooperation Unit Neurooncology, German Cancer Research Center, Heidelberg, Germany.

Cell-coating of FNTDs

FNTDs were autoclaved and washed in Dulbecco's Phosphate-Buffered Saline (DPBS). For direct coating each FNTD was placed in a well of a multi-well plate (24 Well Cell Culture Multiwell Plate, CELLSTAR®, Greiner Bio-One) and the polished surface was covered with cells at different plating densities, from $20 \cdot 10^3$, $100 \cdot 10^3$, $300 \cdot 10^3$ to $400 \cdot 10^3$ ml^{-1}, 0.5 ml per well. The Cell-Fit-HDs were kept in humidified atmosphere until a confluent monolayer had developed. The medium was changed the first time after 24 h and then in 48 h intervals and the cell layer was tightly monitored using a wide-field microscope equipped with phase contrast filter (Axiovert 40C, Zeiss). To test the feasibility of FNTD surface coating with extracellular matrix components, FNTDs were placed in a multiwell plate filled with fibronectin (Bovine Fibronectin, without Bovine Serum Albumin, R&D Systems, Minneapolis, USA) at different concentrations (1, 2.5, 5, 10 or 20 ng l^{-1}, diluted with DPBS) and incubated for 50 min at humidified atmosphere. After incubation FNTDs were gently washed twice with DPBS and covered with cells. Pre-coated FNTDs were sonicated for 15 min and washed with DPBS to remove any solid leftovers before autoclaving them for reuse.

Cell labeling and immunofluorescence staining

To test whether the FNTD, as a substrate, interferes with standard fixation and staining procedures, the cell layer of the hybrid detector was labeled with a series of dyes.

Cells were labeled with a fluorescent dye often used in life cell imaging, Cell-tracker CM-DiI Molecular Probe®, Cat. No. C700) at a concentration of 1.5 $\mu g\ l^{-1}$ in DPBS (1 ml) for 8 min at humidified atmosphere first and then for additional 15 min at room temperature (RT). After labeling, cells were gently washed twice with DPBS. Finally, the Cell-Fit-HD was placed in fresh cell culture medium. For imaging of CM-DiI Leica DM IL LED inverted widefield-microscope equipped with a mercury lamp, CY3 green filter cube and a CCD camera (Leica DFC420 C) were used.

To test viability, A549 cells were stained with 10^{-3} mol m^{-3} calcein acetoxymethly ester (Calcein AM, Molecular Probes®, Cat. No. C1430). Prior to staining the cell layer was washed with DPBS. After incubation (RT) for 30 min, cells were gently washed with DPBS. For Calcein AM imaging the inverted CLSM 710, Confocor 3 (Zeiss) was equipped with 488 nm Argon laser line, EC Plan-Neofluar 40x/1.30 oil objective, main beam splitter (MBS) 488 nm and PMT detection (detection window: 493- 617 nm). As Calcein was the single dye detected, there was no potential spectral overlap within this window. In case of multiple dyes the window could be narrowed around the emission peak at 513 nm.

For membrane and nuclear dual staining, glucose transporter (Glut1) specific antibody and a standard immunofluorescence (IF) protocol were employed. A549 cells were fixed with 4% paraformaldehyde (PFA) in PBS for 10 min (RT). Cells were washed with PBS. After fixation, cells were permeabilized with 0.1% Triton X-100 in PBS (10 min, RT), washed with PBS, blocked in PBS containing 2% bovine serum albumin (BSA) (30 min, RT), and washed with PBS again. Glut1 specific primary antibody (Abcam®, Cat. No. ab652) was used in a dilution of 1:200 in 1% BSA in PBS with 1 h incubation at RT. After the washing step with PBS containing 1% BSA secondary antibody Alexa Fluor 555 goat anti-mouse IgG conjugate (Molecular Probes®, Cat. No. A-21422) was used in dilution of 1:1000 in 1% BSA/ PBS by incubating for 1 h at RT. Cells were washed with PBS containing 1% BSA. For nuclear counter staining, cells were incubated for 5 min (at RT) in HOECHST 33342 (Molecular Probes®, Cat. No. H1399)/ PBS solution with a final concentration of 2 $\mu g\ ml^{-1}$ and washed with PBS. The CLSM 710 Confocor 3 equipped with an EC Plan-Neofluar 40x/1.30 oil objective was used for imaging of the Glut1/HOECHST dual staining. We used the 405 nm diode laser line for HOECHST 33342 and 561 nm Argon laser line for Alexa Fluor 555. The MBS 458/561 nm and MBS 405 nm were used for detection of Alexa Fluor 555 and HOECHST 33342 respectively. The detection window for emitted fluorescent light of Alexa Fluor 555 and HOECHST 33342 were 566-697 nm and 410-550 nm respectively.

For nuclear staining after irradiation of the Cell-Fit-HD, the cells were fixed and stained with HOECHST 33342, 15 min post irradiation. For the fixation and IF procedure the same protocol as for the Glut1/HOECHST dual staining was used.

For imaging with CLSM 710, Confocor 3, the Cell-Fit-HD was placed in uncoated glass bottom culture dishes (MatTek Corp., Ashland, USA, Cat. No. P35G-1.5-10-C). Zeiss Immersol™518 F was used as an immersion medium. Fluoromount-G™ (SouthernBiotech, Birmingham, USA) was used as a mounting medium for all IF staining except HOECHST 33342 single stain. For HOECHST 33342 single stain PBS was used. For live imaging (Calcein AM, CM-DiI) cell culture medium was used as mounting medium.

Irradiation setup for cell-coated FNTD

Carbon ion irradiations of Cell-Fit-HD were performed with the therapy beam of the Heidelberg Ion Beam Therapy Center (HIT) at Heidelberg University Hospital. The ion beam fluence was adjusted to $1.5 \cdot 10^6$ cm^{-2} using controls of the treatment system, resulting in an average of 1.3 hits per nucleus (assuming all nuclei to be of equivalent size with an area of 10 x 10 μm^2). In total, a 12 x 12 cm^2 field was irradiated homogeneously using raster scanning

with a pencil beam of 10.1 mm in diameter (full width at half maximum) and a distance of 2 mm between two raster spots. Approximately 60,000 particles were delivered in each spot. The Bragg peak was extended by using a 3 mm Ripple filter. The cell layer was placed in the rising flank of the Bragg peak (initial carbon ion energy of 270.55 MeV u^{-1}, corresponding equivalent range in water r_{H_2O}= 13.70 cm). As stopping material 11.7 cm of PMMA with r_{H_2O}= 13.57 cm was placed in front of a multiwall plate (24 Well Cell Culture Multiwell Plate, CELLSTAR®, Greiner Bio-One) containing the cell-coated FNTDs (see Additional file 1: Figure S1). The multiwell plate was placed perpendicular to the incident beam. Irradiation setup in experimental room at HIT with horizontal beam propagation requires vertical positioning of samples. The FNTD crystals are 0.5 mm thick with equivalent range in water r_{H_2O}= 1.65 mm. The back side of the FNTDs without cell coating were facing the incident beam and were attached to the bottom (polystyrene with r_{H_2O}= 1.2 mm) of the multiwell plate by small agarose droplets. The air gap between the culture well and the PMMA was not considered in the total r_{H_2O}. Culture wells were filled with cell culture medium to keep the cell coating viable during irradiation. The total amount of materials in front of the iso center (vacuum exit window, beam application monitoring system, air) corresponds to a r_{H_2O} of 2.89 mm.

Microscopy settings for sequential read-out of cell-coated FNTD

For the sequential read-out of the FNTD component and the cell layer of the Cell-Fit-HD, we used the CLSM 710, Confocor 3 equipped a 63x/1.45 NA oil objective, APD/PMT/T-PMT detection.

For the FNTD read-out we used the protocol as described in [10]. The FNTD crystals were scanned by the 633 nm Helium Neon laser line (100% transmission). A main dichroic beam splitter (MBS) 488/561/633 nm was used to separate the emission signal from the excitation light. A 655 nm long-pass filter was used in fluorescent emission path and the Avalanche Photo Diode (APD) for emission detection was used in photon counting mode. The microscope detector pinhole aperture was set to 1 Airy disk diameter unit (AU). The cell layer was imaged with 405 nm diode laser line (30 mW, 4.0% transmission) for HOECHST 33342. For the photomultiplier (PMT) detection of HOECHST 33342, a MBS 405 nm was used (detection window 410 nm - 495 nm). For the FNTD and cell layer acquisition, we limited the line-scanning repetition to 4 and a pixel dwell time to 2.80 μs. In both cases, the size of the imaging field was 134.784 x 134.784 μm^2 with a total number of 1152 x 1152 pixels and a pixel size of 0.117 x 0.117 μm^2 (estimated according to Rayleigh criterion). This results in a frame-acquisition time of 14.9 s. The acquired FNTD image stack was adjusted to cover an axial range of about 120 μm (measured from the detector surface) with a z-interval (Δz) of 3 μm. This allows for accurate single ion track reconstruction as described in [11]. The acquired cell layer stack covered a range of about 10 μm (Δz= 0.3 μm).

Results

FNTD crystals are biocompatible

To develop Cell-Fit Hybrid Detectors, first the adherence, viability and growth of different human (A549, A541, U87, PC3) and murine (SMA-560) cell lines on the FNTD surface were tested. We were able to produce a viable and stable cell layer on the polished crystal surface. Cells were seeded directly or after coating with fibronectin as an intermediate layer to enhance cell adhesion on the crystal surface (Table 1). We varied the plating density and fibronectin concentration to optimize the coating and to quantify cell proliferation kinetics. SMA-560 (with fibronectin), PC3 (without fibronectin), A431 (with/without fibronectin) and A549 (with/without fibronectin) cells were able to form a uniform coating after 24 h using high seeding density ($\geq$ 300,000 ml^{-1}). In comparison, the proliferation rate of U87 cells (300,000 ml^{-1}, with/without fibronectin) was found to be lower. After 120 h these cells still formed a loosely packed network. For A549 cell line, a uniform cell coating were also be achieved after longer incubation time (after 48 h) using lower plating density (100,000 ml^{-1}).

At low seeding concentration (20,000 ml^{-1}) the proliferation rate of SMA-560 (with fibronectin) and U87 cells (with fibronectin) was decreased as compared to cells growing on the cell culture treated surface, e.g. on the bottom of the wellplates in which the Cell-Fit-HDs were incubated. SMA-560 (with fibronectin) developed a network of overlapping cells on the FNTD's surface after 120 h. Lower concentrations of fibronectin (2.5, 5 ng ml^{-1}) seemed to be favorable for both cell lines using low seeding concentrations.

Concerning the morphology, all cells were spread and flat. They exhibited the same shape as grown on standard cell culture treated surfaces under controlled conditions (incubator, humid atmosphere). In general, the epithelial tumor cell lines, A549, A431 and PC3 formed a tightly packed monolayer in comparison with gliomas SMA-560 and U87 developing networks of overlapping cells. Figure 2a,b shows a section of a monolayer of A549 cells without additional fibronectin coating. Those cells exhibited a cubic morphology.

Cell labeling and immunofluorescence staining of Cell-Fit-HD

To evaluate the feasibility of co-detection of biological information using fluorescence based cell stains on

Table 1 Cell-coating experiments

Cell line	Seeding density [1/well]	Fibronectin [ng/ml]	Cell-coating		
			> 24 h	**> 48 h**	**> 120 h**
SMA-560	10 000	2.5, 5, 10, 20	Single cells, no network	Single cells, no network (*)	Network of overlapping cells
	150 000	2.5, 5, 10, 20	network of overlapping cells		
	150 000	-	-	-	-
U87	10 000	2.5, 5, 10, 20	single cells, no network	single cells, no network (*)	single cells, no network
	150 000	2.5, 5, 10, 20	loosely packed network		
	150 000	-	loosely packed network		
PC3	200 000	2.5	-	-	-
	200 000	-	tightly packed monolayer		
A431	200 000	2.5	tightly packed monolayer		
	200 000	-	tightly packed monolayer		
A549	50 000	-	-	tightly packed monolayer	
	150 000	1, 2.5, 5	tightly packed monolayer		
	150 000	-	tightly packed monolayer		

The table shows the results of cell coating on the surface of FNTD crystals using different cell lines with and without a fibronectin intermediate layer. Each well contained 500 μl. Cell culture medium was exchanged every 48 h. (*) Proliferation rate is lower compared to cells grown on the untreated bottom of a culture well.

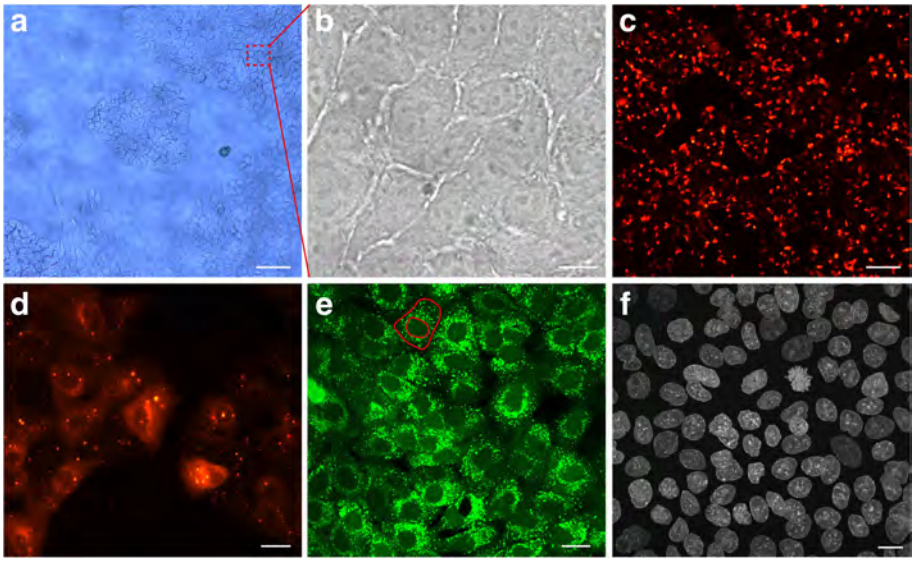

Figure 2 A549 cell coating. (a) A549 cells cultured on the FNTD crystal surface starting to form a confluent monolayer. A typical island formation with branching cells is clearly visible. Scale bar, approximately 200 μm **(b)** Magnified section of a confluent monolayer. The cells are tightly packed. It is difficult to contrast cells from the transparent crystal substrate with light microscopy. Scale bar, 10 μm. **(c)** CM-DiI labeled and proliferating cells forming a confluent monolayer. Scale bar, approximately 200 μm **(d)** Section of CM-DiI labeled monolayer reveals clear cytoplasmic coloring. Cytoplasmic granules (multilamellar bodies) exhibit a strong fluorescent signal. Scale bar, approximately 20 μm. **(e)** Cell layer is labeled with Calcein AM to test cell viability. The outer red line indicates the cell membrane. The cell nucleus is defined by the inner red line. A strong perinuclear fluorescent signal with many bright spots (cytoplasmic organelles) and round nuclei indicate good cell viability. Scale bar, 20 μm. **(f)** Immunofluorescent labeling of cell nuclei by HOECHST 33342 stain. A uniform monolayer of proliferating cells is visible. Scale bar, 10 μm. Images **(a)**, **(c)**, and **(d)** were obtained by wide field microscopy whereas images (b, e, and f) were obtained in confocal fluorescent mode. Images **(a)**-**(e)** show live cell stainings. In **(f)** cells are fixed with 4% PFA.

the surface of FNTDs, we applied various cell labeling and immunofluorescence protocols on Cell-Fit-HDs. We found that the FNTD crystal surface as a substrate is compatible with all staining protocols tested. Calcein AM labeling was used for live cell imaging and for determining the viability of A549 cells (Figure 2e). The high levels of fluorescence signal as well as the shape of the cell nuclei indicated good cell viability. The bright spots are organelles (multilamellar bodies) in the cytoplasm with high esterase activity correlating with active metabolism.

We used CM-DiI labeling as cell tracker dye to achieve a better contrast between cells and the crystal substrate (Figure 2c,d). This labeling is based on thiol-reactive chloromethyl moiety that allows the dye to covalently bind to cellular thiols. CM-DiI staining suggested exocytotic activity of cells as small bodies with fluorescent signal are present in intercellular space.

To estimate the cell density of tightly packed A549 coating we did immunohistochemical analysis and used HOECHST as nuclear stain (Figure 2f). The bulk had a cell density of approximately $6.3 \cdot 10^5$ cm^{-2}. We combined HOECHST with Glut-1 staining to visualize cell membranes and to detect cell-cell adhesion (Figure 3). There is strong accumulation of Glut1 at the membrane thus forming a sharply bounded network. Together, membrane labeling with Glut1 or CM DiI demonstrated that A549 cells maintained their tight epithelial cell-cell contact in Cell-Fit-HD.

Irradiation of Cell-Fit-HD and sequential read-out

Placing the A549 cell-coated FNTD in a well filled with culture medium allows for an easy handling and mounting for the irradiation (Additional file 1: Figure S1). The cells stayed alive during irradiation. The total irradiation time (adjusting the ion-beam fluence to an average of 1.3 hits per nucleus) was less than 10 s.

After conventional fixation (using 4% PFA) and staining procedure for HOECHST (cells remained on FNTD) the detector and the cell layer were imaged successfully in two consecutive steps using the same CLSM (Figure 4). No post-irradiation chemical processing of the FNTD or removal of the cell layer was necessary.

When imaging the cell layer prior to the FNTD, an increase in the detector background signal in the surface region (first few μm) occur. We adjusted the scan and detection parameters (see Methods) of the FNTD read-out to achieve relatively fast acquisition (frame-acquisition time of 14.9 s) without forfeiting much signal-to-noise ratio (SNR).

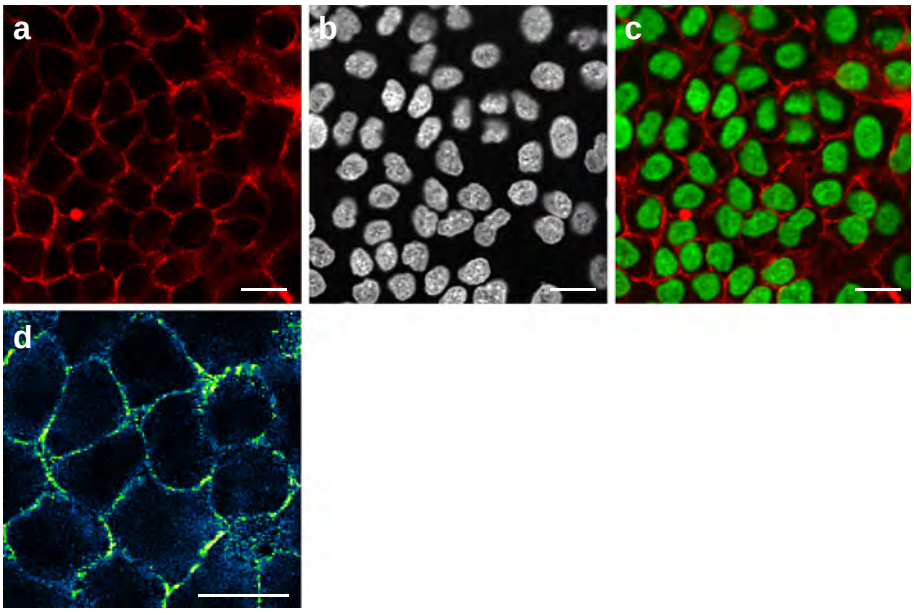

Figure 3 Membrane and nuclear staining of A549 Cell-Fit-HD. (a) Glucose transporter Glut1 staining visualizes the A549 cell membrane. Glut1 is mainly accumulated at the membrane. The diffuse cytoplasmic signal may arise from permeabilisation during immunofluorescent staining. **(b)** HOECHST staining as nuclear counterstain. **(c)** Merging of Glut1 and HOECHST images. A549 cells form a tightly packed monolayer with strong cell-cell adhesion. **(d)** A section of **(a)** with different color coding (blue-green-yellow) is shown. The distinct yellow bright spots indicate a discrete strong accumulation of Glut1 at the membrane. Scale bars, 20 μm. **(a)**-**(d)** were obtained by confocal fluorescent microscopy.

Figure 5 shows the spatial correlation between carbon ion tracks and A549 cell layer gained after the sequential read-out. Compared to cell nuclei (diameter $\approx$ 10 μm) single ion tracks visualized by track spots - the characteristic signature left in the FNTD crystal after irradiation - have a diameter of less than 1 μm.

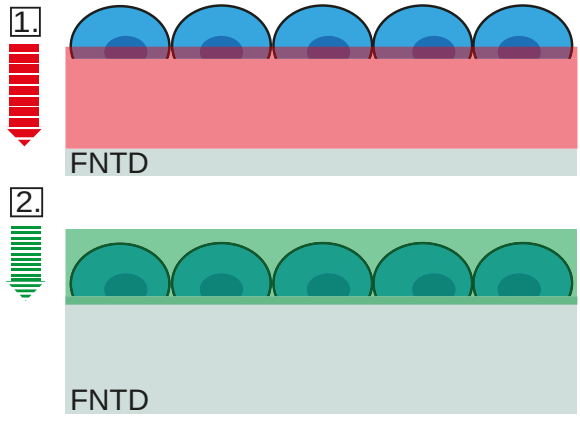

Figure 4 Sequential read-out of Cell-Fit-HD. To avoid photoionization of FNTD crystals the imaging is first performed with the red laser on FNTD crystal and only after that the scan continues with blue laser on stained cell layer. The total axial range for the acquired image stack is about 120 μm with depth increment (Δz) of 3 μm for FNTD crystal and Δz= 0.3 μm for the cell-layer. The axial range for the image stack of cells is about 10 μm. The difference in optical sectioning is indicated by the striped arrows.

Discussion

To our knowledge, we report here the first successful development of a hybrid detector technology, Cell–Fit–HD, allowing simultaneous acquisition and correlation of radiation track information with cellular and molecular parameters. It was recently shown that Al_2O_3:C,Mg single crystal based fluorescent nuclear track detectors (FNTDs) allow for visualization and characterization of single particle tracks by conventional fluorescence microscopy [7,11]. Given that confocal microscopy is a common method for detection of molecular- and cellular biology parameters, it was hypothesized that development of hybrid detectors will provide a hitherto unmatched correlation of physical with biological parameters at high resolution, only limited by light diffraction [7]. However, little is known about the properties of the polished and planar detector surface with regard to their biocompatibility. Based on the relatively inert chemical reactivity of Al_2O_3:C,Mg crystals and their high thermal resistance (up to 600°C) [12] we were able to successfully autoclave the crystals, as a prerequisite for sterile cell coverage. The ability of the FNTD technology to precisely measure energy deposition along carbon ion tracks was neither affected by autoclaving nor by prolonged exposure to high humidity under standard culture growth conditions. Next, we tested

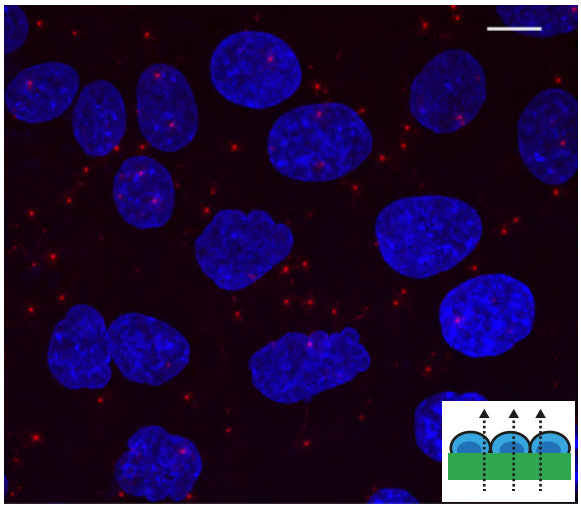

Figure 5 Correlation between carbon ion tracks and A549 cell layer. Superposition of cellular response data (maximum intensity z-projection) with an image of the acquired FNTD image stack. The red spots are the ion tracks (with FWHM of approximately 500 nm [9]). The small trajectories branching from the ion tracks are tracks of secondary electrons in the FNTD crystal. The cell nuclei (depicted in blue) are labeled with HOECHST. The surface of cell-coated FNTD was set perpendicular to the incident carbon ion beam (small insert). Initial carbon ion energy was 270.55 MeV u^{-1} and fluence - 10^6 cm^{-2}. Scale bar, 10 μm.

the adherence, the viability and conformal coverage of the crystals coated with a panel of human and murine cells.

We found that these crystals are biocompatible for all of the cell lines tested enabling the development of Cell-Fit-HD. The cells were spread and flat thus indicating good cell attachment. Cell adhesion could also benefit from the doping of Al_2O_3 with magnesium ions as several molecules involved in cell adhesion such as integrins, have binding sites for divalent ions [13]. In addition the use of different extracellular matrix (ECM) component to enhance cell adhesion, as performed in this study, treatment of the crystal surface with plasma or additional bombardment of the detector surface with Mg^{2+} ions [14] may further enhance cell adhesion. The crystal surface was suitable for most of the cell lines tested in order to gain a viable and uniform cell coating (Table 1). It was possible to achieve uniform cell coating (Table 1) either in short incubation time (after 24 h) using high plating density ($\geq$ 300,000 ml^{-1}) or longer incubation time using a lower plating density. For the two brain tumor cell lines, human U87 and murine SMA-560 at low seeding concentrations (20,000 ml^{-1}) the fibronectin concentration could further be optimized to improve cell coating or another extra cellular matrix component like collagen could be tested. The fibronectin layer has a height of several nm and does not interfere with the limited mechanical working distance of a microscope objective at high magnification.

As compared to standard treated surfaces for cell cultures all tested cell lines maintained their morphology when plated on the crystal surface. Based on the cell types the tested cell lines formed either glioma-like cell networks (SMA-560 and U87) or tightly packed epithelial monolayers (PC3, A431, A549). The evaluation using conventional phase contrast microscopy was hindered by the transparency of Al_2O_3:C,Mg (Figure 2a). Our data indicated that neither the physical properties of the crystal component nor the physiological properties of the cell lines were compromised.

We selected A549 cells for subsequent Cell-Fit-HD studies due to their superior performance in terms of cell adhesion, viability, proliferation, metabolism and formation of a tightly packed epithelial network on the crystal surface without the need of additional ECM coverage. Al_2O_3:C,Mg crystal proved to be compatible with standard fixing and staining procedures. The fluorescent dyes did not accumulate at the surface nor seemed to affect the surface properties, hence causing low background during image acquisition of the cell layer. Moreover, fixation (4% PFA) did not distort A549 cell morphology when seeded on the detector surface (Figure 2). The cells can be read-out in situ on the crystal surface by conventional confocal microscopy. When reading out the cell layer prior to the crystal with blue (405 nm) laser light, it is possible to photoionize pristine F_2^{2+} (2 Mg) color centers in the surface region by two-photon absorption processes resulting in increase in background 750 nm fluorescence used for track imaging. To avoid this increase in background signal, we imaged the crystal with red (633 nm) laser scanning prior to the cell layer scanning with the blue laser. The crystal read-out with the red laser in turn does not bleach fluorescent dyes in the cell layer nor seems to affect the cell layer in another manner (e.g., morphology). No post-irradiation chemical processing of the crystal or removal of the cell layer is necessary for the sequential read-out, thus eliminating a significant source of error. The high cell density (A549) with strong cell-cell adhesion (Figure 3) and fixation directly after irradiation limits cell migration and distortion of the actual spatial correlation or hit statistics.

To examine the capability of Cell-Fit-HD to detect biological processes governing radiation effects in different cell compartments with physical energy deposition along ion tracks, visualization of different key cellular compartments was evaluated. Our data indicate that Cell-Fit-HD is compatible with standard immunofluorescent techniques. Therefore Cell-Fit-HD may be used to detect radiation induced molecular events on cell membrane such as differential regulation of cell adhesion molecules/receptors

and their downstream signaling events as demonstrated by membrane staining using antibody (Glut1) or life dyes (CM DiI). Moreover, direct damaging effects of ionizing irradiation in different cellular compartment such as mitochondria or nucleus could be tested by specific staining of these compartments as demonstrated here for DNA-staining in nucleus (HOECHST) or candidate alternative dyes such as DAPI or ToPro. Together, application of standard fluorescent staining techniques on the cell layer and the sequential read-out of the Cell-Fit-HD enable spatial correlation between single ion traversal and cell biology (Figure 5). Currently, algorithms are developed to correlate the physical information achieved in crystal compartment with biological events detected in the cell layer.

Conclusions

Development of a next generation cell-fluorescent ion track hybrid detector (Cell-Fit-HD) is reported permitting co-detection and direct correlation of physical and biological information at high resolution using standard fluorescence microscopy. Detection of physical energy deposition along carbon ion-tracks is based on Al_2O_3:C,Mg crystals (FNTDs). We showed that these crystals are chemically inert, could be autoclaved and provide a biocompatible surface for prolonged culture of different cell lines. The crystals provided a substrate for a uniform cell coating. Cells maintained their morphology, metabolism, proliferated and remained viable for a long observation period in Cell-Fit-HD. Moreover, the quality of the FNTD readout was not compromised by different standard fixation procedures and labeling of different cell compartments using life fluorescent dyes or immunofluorescence. This offers the possibility of carrying out a multitude of live-imaging and fluorescent staining experiments directly linking the effect of physical energy deposition along ion tracks with subsequent cellular events on membrane, cytoplasm, organelles or nuclear compartment. The here reported method for development of Cell-Fit-HD will be instrumental for introduction of a novel generation of compact detectors facilitating research in radiobiology laboratories with limited access to more complex detector technologies and microbeam delivery systems. Cell-Fit-HD can be irradiated with different radiation qualities, i.e. protons and heavier ions.

Additional file

Additional file 1: Figure S1. Irradiation setup for Cell-Fit-HD. The Cell-Fit-HD was irradiated perpendicular to the incident carbon ion beam. Irradiation setup at Heidelberg Ion-Beam Therapy Center (HIT) requires a vertical positioning of the sample. Only a single well of a multiwell plate is shown.The FNTD is attached by agarose droplets to the polystyrene bottom of the multiwell plate. The well is filled with culture medium to keep the cells viable during irradiation. It is sealed with Parafilm® M (Pechiney Plastic Packaging). The air gap between PMMA block and the multiwell plate is neglected as the corresponding energy loss is very small. The range in water (r_{H_2O}) of all elements in the beam path (position and fluence monitors) between exit window of the beam line and isocenter of the incident ion beam is 2.89 mm.

Competing interests

The authors declare that they have no competing financial interests.

Authors' contributions

MN performed experiments, analyzed data and together with AA wrote the manuscript. CM participated in the cell-coating experiments. MA developed the crystal material and FNTD imaging technique. MN and SG developed the co-detection of physical- and biological parameters by confocal microscopy. SG initiated the project. MN, SG, JD, OJ and AA designed experiments and interpreted the data. All authors edited the paper. All authors read and approved the final manuscript.

Authors' information

Martin Niklas and Steffen Greilich shared first authorship.

Acknowledgements

We are grateful to S. Brons for generously providing support and technical irradiation assistance at the Heidelberg Ion-Beam Therapy Center (HIT). We should also like to thank F. Bestvater and M. Brom of the DKFZ's light microscopy facility for their enthusiasm and unflagging support. M.N. is funded by the fellowship from the Helmholtz International Graduate School for Cancer Research at the German Cancer Research Center. C.M. is supported by the University of Heidelberg. S.G and A.A. are supported by the German Cancer Research Center. J.D. and O.J. are supported by the University Hospital Heidelberg. M.A. is supported by Landauer R&D money. This work was supported German Research Council (DFG, KFO214), National Aeronautics and Space Administration under NSCOR grant no. NNJ06HA28G, the German Krebshilfe (Deutsche Krebshilfe, Max- Eder 108876), intramural Grants of the National Center for Tumor diseases (NCT, Heidelberg, Germany), the Helmholtz Association (Translating hadron therapy from basic research to clinical application, VH-VI-303, S.G.) and the German Federal Ministry of Research and Technology (Bundesministerium für Bildung und Forschung - BMBF 03NUK004C).

Author details

[1]Division of Medical Physics in Radiation Oncology, German Cancer Research Center, INF 280, 69120 Heidelberg, Germany. [2]German Cancer Consortium (DKTK), National Center for Radiation Research in Oncology, Heidelberg Institute of Radiation Oncology, INF450/400, Heidelberg, Germany. [3]Molecular & Translational Radiation Oncology, Heidelberg Ion-Beam Therapy Center (HIT), University of Heidelberg Medical School and National Center for Tumor Diseases (NCT), German Cancer Research Center (DKFZ), 69120 Heidelberg, Germany. [4]Department of Radiation Oncology and Radiation Therapy, University Hospital Heidelberg, INF 400, 69120 Heideberg, Germany. [5]Heidelberg Ion-Beam Therapy Center (HIT), Im Neuenheimer Feld 450, 69120 Heidelberg, Germany. [6]Stillwater Crystal Growth Division, Landauer Inc., 723 1/2 Eastgate, Stillwater Oklahoma 74074, USA. [7]Center of Cancer Systems Biology, Nasa Specialized Center Of Research (NSCOR), St. Elizabeth's Medical Center, Tufts University School of Medicine, Boston, MA, USA.

Received: 27 February 2013 Accepted: 30 May 2013
Published: 11 June 2013

References

1. Weyrather WK, Ritter S, Scholz M, Kraft G: **RBE for carbon track-segment irradiation in cell lines of differing repair capacity.** *Int J Radiat Biol* 1999, **75**(11):1357–1364.
2. Bucker H: **The Biostack Experiments I and II aboard Apollo 16 and 17.** *Life Sci Space Res* 1974, **12:**43–50.
3. Bucker H, Horneck G, Allkofer OC, Bartholoma KP, Beaujean R, Cuer P, Enge W, Facius R, Francois H, Graul EH, *et al*: **The Biostack experiment on Apollo 16.** *Life Sci Space Res* 1973, **11:**295–305.

4. Chan K, Yum E, Wan C, Fong W, Yu K: **Study of DNA integrity in alpha-particle radiobiological experiments using thin CR-39 detectors.** *Radiat Meas* 2008, **43, Suppl. 1:**S541–S545.
5. Osinga JM, Akselrod M, Herrmann R, Hable V, Dollinger G, Jäkel O, Greilich S: **High-accuracy fluence determination in ion beams using fluorescent nuclear track detectors.** *Radiat Meas* 2013, http://dx.doi.org/10.1016/j.radmeas.2013.01.035.
6. Akselrod M, Sykora G: **Fluorescent nuclear track detector technology - A new way to do passive solid state dosimetry.** *Radiat Meas* 2011, **46**(12):1671–1679.
7. Akselrod G, Akselrod M, Benton E, Yasuda N: **A novel Al2O3 fluorescent nuclear track detector for heavy charged particles and neutrons.** *Nucl Instrum Meth B* 2006, **247:**295–306.
8. Sykora G, Akselrod M, Benton E, Yasuda N: **Spectroscopic properties of novel fluorescent nuclear track detectors for high and low LET charged particles.** *Radiat Meas* 2008, **43**(2-6):422–426.
9. Niklas M, Melzig C, Abdollahi A, Bartz J, Akselrod M, Debus J, Jäkel O, Greilich S: **Spatial correlation between traversal and cellular response in ion radiotherapy - towards single track spectroscopy.** *Radiat Meas* 2013, http://dx.doi.org/10.1016/j.radmeas.2013.01.060.
10. Greilich S, Osinga JM, Niklas M, Lauer F, Klimpki G, Bestvater F, Bartz J, Akselrod M, Jäkel O: **Fluorescent nuclear track detectors as a tool for ion-beam therapy research.** *Radiat Meas* 2013, http://dx.doi.org/10.1016/j.radmeas.2013.01.033.
11. Niklas M, Bartz JA, Akselrod MS, Abollahi A, Jäkel O, Greilich S: **Ion track reconstruction in 3D using fluorescent nuclear track detector.** submitted to Phys Med Biol 2013, pre-print available at arXiv: 1306.2261 [physics.med-ph].
12. Akselrod MS, Akselrod AE, Orlov SS, Sanyal S, Underwood TH: **Fluorescent aluminum oxide crystals for volumetric optical data storage and imaging applications.** *J Fluoresc* 2003, **13:**503–511.
13. Zreiqat H, Howlett C, Zannettino A, Evans GPandSchulze-Tanzil, Knabe C, Shakibaei M: **Mechanisms of magnesium-stimulated adhesion of osteoblastic cells to commonly used orthopaedic implants.** *J Biomed Mater Res* 2002, **62:**175–184.
14. Yokoyama Y, Tsukamoto T, Kobayashi T, Iwaki M: **The changes of cell adhesion to collagen-coated Al2O3 by ion bombardment.** *Surf Coat Technol* 2005, **196:**298–302.

doi:10.1186/1748-717X-8-141
Cite this article as: Niklas *et al.*: Engineering cell-fluorescent ion track hybrid detectors. *Radiation Oncology* 2013 **8**:141.

D

Phys. Med. Biol. **58** (2013) N251–N266 doi:10.1088/0031-9155/58/18/N251

NOTE

Ion track reconstruction in 3D using alumina-based fluorescent nuclear track detectors

M Niklas[1,2], J A Bartz[3,4], M S Akselrod[4], A Abollahi[2,5,6,7,8], O Jäkel[1,2,6,7] and S Greilich[1,2]

[1] German Cancer Research Center (DKFZ), Division of Medical Physics in Radiation Oncology, INF 280, D-69120 Heidelberg, Germany
[2] German Cancer Consortium (DKTK), National Center for Radiation Research in Oncology, Heidelberg Institute of Radiation Oncology, INF450/400, D-69120 Heidelberg, Germany
[3] Physics Department, Oklahoma State University, Stillwater, OK 74078-3072, USA
[4] Landauer Inc., Stillwater Crystal Growth Division, 723 1/2 Eastgate, Stillwater, OK 74074, USA
[5] Molecular & Translational Radiation Oncology, Heidelberg Ion-Beam Therapy Center (HIT), University of Heidelberg Medical School and National Center for Tumor Diseases (NCT), German Cancer Research Center (DKFZ), D-69120 Heidelberg, Germany
[6] Department of Radiation Oncology and Radiation Therapy, University Hospital Heidelberg, INF 400, D-69120 Heideberg, Germany
[7] Heidelberg Ion-Beam Therapy Center (HIT), Im Neuenheimer Feld 450, D-69120 Heidelberg, Germany
[8] Center of Cancer Systems Biology, Nasa Specialized Center Of Research (NSCOR), St. Elizabeth's Medical Center, Tufts University School of Medicine, Boston, MA, USA

E-mail: m.niklas@Dkfz-Heidelberg.de

Received 2 April 2013, in final form 1 July 2013
Published 22 August 2013
Online at stacks.iop.org/PMB/58/N251

Abstract

Fluorescent nuclear track detectors (FNTDs) based on Al_2O_3:C,Mg single crystal combined with confocal microscopy provide 3D information on ion tracks with a resolution only limited by light diffraction. FNTDs are also ideal substrates to be coated with cells to engineer cell-fluorescent ion track hybrid detectors (Cell-Fit-HD). This radiobiological tool enables a novel platform linking cell responses to physical dose deposition on a sub-cellular level in proton and heavy ion therapies. To achieve spatial correlation between single ion hits in the cell coating and its biological response the ion traversals have to be reconstructed in 3D using the depth information gained by the FNTD read-out. FNTDs were coated with a confluent human lung adenocarcinoma epithelial (A549) cell layer. Carbon ion irradiation of the hybrid detector was performed perpendicular and angular to the detector surface. *In situ* imaging of the fluorescently labeled cell layer and the FNTD was performed in a sequential read-out. Making use of the trajectory information provided by the FNTD the accuracy of 3D track reconstruction of single particles traversing the hybrid detector was studied. The accuracy is strongly influenced by the irradiation angle and therefore by complexity of the FNTD signal. Perpendicular irradiation results in highest accuracy with error of smaller

than 0.10°. The ability of FNTD technology to provide accurate 3D ion track reconstruction makes it a powerful tool for radiobiological investigations in clinical ion beams, either being used as a substrate to be coated with living tissue or being implanted *in vivo*.

(Some figures may appear in colour only in the online journal)

1. Introduction

Al_2O_3:C,Mg-based fluorescent nuclear track detectors (FNTDs) (Akselrod and Sykora 2011) are ideal candidates for engineering cell-fluorescent ion track hybrid detectors (Niklas *et al* 2013a). In this hybrid the FNTD is used as a substrate to be coated with a viable cell layer thus allowing for standard cellular imaging after proton and heavy ion irradiation. In addition the FNTD is used for single track detection. This radiobiological tool enables a novel platform linking physical energy deposition and biological response with a resolution only limited by diffraction (figure 1). The major advantage of using FNTD as the central component is its capability of being read out by confocal laser scanning microscopy commonly used in life science (Akselrod and Sykora 2011, Greilich *et al* 2013). In particular this allows for *in situ* imaging of fluorescently labeled cell layer and the subjacent detector (Niklas *et al* 2013a). The FNTD comprises superior spatial resolution compared to available CR-39 plastic nuclear track detectors and does not require chemical treatment (Akselrod *et al* 2006, Osinga *et al* 2013). FNTDs exhibit high detection efficiency (close to 100%) (Osinga *et al* 2013), a wide range of LET sensitivity (Akselrod and Sykora 2011) and depth information (Akselrod *et al* 2006).

In order to acquire accurate spatial correlation in 3D between individual ion hits in the cell layer and its subsequent response, the ion tracks have to be reconstructed in 3D using the depth information gained by the FNTD read-out (Akselrod *et al* 2006, Bartz *et al* 2013).

In this paper we analyzed the FNTD signals after perpendicular and angular carbon ion irradiation of the hybrid detector. Making use of the trajectory information provided by the FNTD we studied the accuracy of 3D track reconstruction of particles traversing the hybrid detector. For this purpose single track spots—the ion's characteristic signature in the Al_2O_3:C,Mg—and their corresponding centers belonging to a single ion track were precisely located in the acquired FNTD image stack (a sequence of optical slices in z). Linear regression analysis (LRA) was then applied to fit the ion track. Each track was extrapolated above the detector surface into a cell layer grown on top of the FNTD. Due to a refractive index mismatch in the optical path of the imaging of the hybrid detector correction of spherical aberrations (Hell *et al* 1993, Jacobsen and Hell 1995) was applied.

2. Materials and methods

2.1. Al_2O_3:C,Mg-based FNTD

FNTDs are made of alumina single crystals (α-Al_2O_3) doped with magnesium and carbon ions and exhibit high concentrations of F_2^{2+}(2Mg) aggregate defects (excitation at 435 nm and emission of fluorescence at 515 nm) (Akselrod and Sykora 2011). F_2^{2+}(2Mg) undergo radiochromic transformation. The resulting stable, transformed color centers, F_2^{+}(2Mg), absorb light in the band centered at 620 nm, prompting fast 750 nm fluorescence. The fluorescent intensity depends on local energy deposition of the ionizing radiation (Niklas *et al* 2013b). Accordingly, FNTDs allow for particle track visualization by confocal microscopy and subsequent 3D particle track reconstruction (Akselrod *et al* 2006). FNTDs are sensitive to

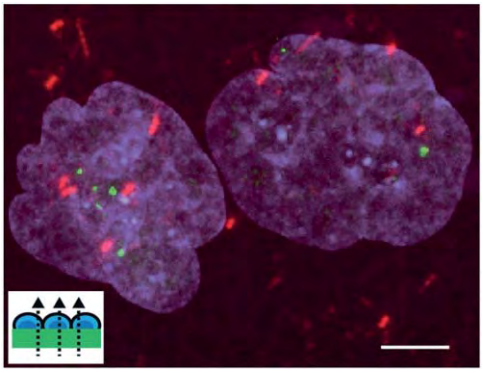

Figure 1. Spatial correlation between single carbon ion traversal and cell damage (Reproduced with permission from Niklas *et al* 2013b. Copyright Elsevier 2013). Fluorescent nuclear track detector (FNTD) was coated with A549 cells and irradiated perpendicularly to its surface (insert). Maximum intensity z projection between single carbon ion traversals (red spots) and subsequent DNA double strand breaks (γ-H2AX, immunofluorescent staining, green spots). Cell nuclei are labeled in blue (HOECHST 33342 staining). Scale bar, 5 μm.

ions with LET > 0.5 keV μm^{-1} (Akselrod and Sykora 2011). The current limit of maximum countable track fluence is in the range of 0.5×10^8 cm^{-2} (Osinga *et al* 2013) corresponding to clinical doses for carbon ion irradiation (i.e. 2.27 Gy in water for ^{12}C, 90 MeV u^{-1}). FNTDs have one 4 mm $\times$ 8 mm surface polished to optical quality for read-out. The optical c-axis of the crystal is aligned parallel to the longer side of the detector (figure 2(a)).

2.2. Cell coating and irradiation setup

The polished surface of sterilized FNTDs were coated with a confluent human lung adenocarcinoma epithelial (A549) cell layer with the protocol described in Niklas *et al* (2013a) (plating density: 100 000 ml^{-1}, culture medium: Dulbecco's modified Eagle medium, Biochrom AG, Cat. No. FG 0415). A549 cells were obtained from Deutsche Sammlung von Mikroorganismen und Zellkulturen (DSMZ, Braunschweig, Germany). Fifteen minutes after the irradiation the cells remaining on the FNTD crystal were fixed with 4% paraformaldehyde in phosphate buffered saline (PBS) for 10 min at room temperature. Cell nuclei were stained with HOECHST 33342 fluorescent dye (Molecular Probes ®, Cat. No. H1399, final concentration: 2 μg ml^{-1}) as described in Niklas *et al* (2013a).

Carbon ion irradiation of FNTD was performed using the therapy beam of the Heidelberg Ion-Beam Therapy Center (HIT) at Heidelberg University Hospital. Irradiations were performed under the polar angle θ (angle between the direction of propagation of the ions $\vec{s}$ and the k-axis of Al_2O_3:C,Mg) of $0^\circ \pm 5^\circ$ and $60^\circ \pm 5^\circ$ (figure 2(a)). The azimuth angle ϕ (angle between the optical c-axis and $\vec{e}_{x,y}$, the projection of the ion beam onto the exposed FNTD surface) only played a minor role for the setup. For perpendicular irradiation ($\theta = 0^\circ$) the ion beam fluence was adjusted to 1.5×10^6 cm^{-2}. For angular irradiation ($\theta = 60^\circ$) the fluence at the FNTD surface corresponded to 1.3×10^6 cm^{-2}. In both cases, a 12 $\times$ 12 cm^2 field was irradiated homogeneously using raster scanning with a pencil beam of 10.1 mm in diameter (full width at half maximum (FWHM)) and a distance of 2 mm between two raster spots. Approximately 60 000 particles were delivered in each spot. The Bragg peak was broadened in depth by using a 3 mm Ripple filter. The cell-coated FNTDs, mounted with agarose in a 24 multiwell plate filled with culture medium (Niklas *et al* 2013a), were placed in the rising flank of the Bragg peak (initial carbon ion energy of 270.5 MeV u^{-1}, corresponding equivalent range

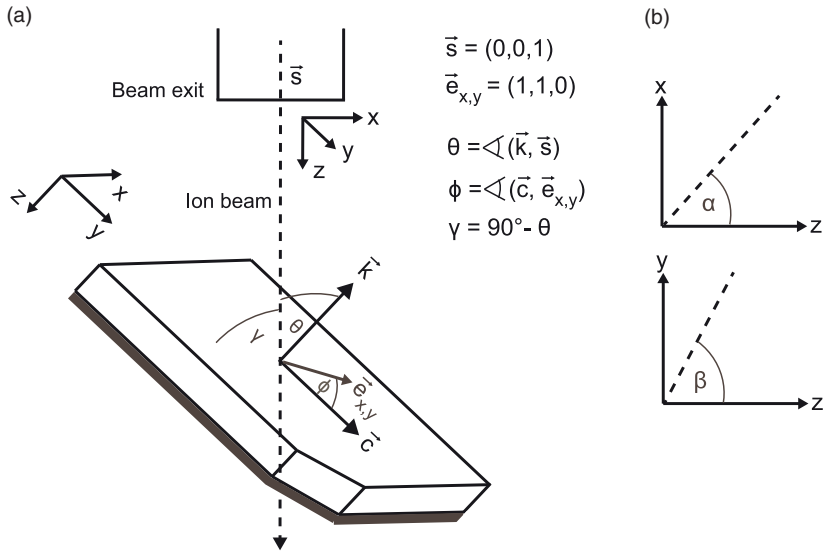

Figure 2. Irradiation setup and particle track reconstruction. (a) The ions are traversing the detector under the angle θ—the angle between direction of propagation of the ions $\vec{s}$ and k-axis of the FNTD (of dimension $4 \times 8 \times 0.5$ mm^3). $\vec{k}$, $\vec{c}$, $\vec{e}_{x,y}$ and all angles refer to the coordinate system of the FNTD. $\vec{s}$ refers to the beam coordinate system. The cell coating is indicated by the gray layer. (b) Splitting of fitting procedure into two separate linear regression analysis for the x- and y-coordinate of the track spot centers.

in water $r_{H_2O} = 13.70$ cm). For the irradiation under $\theta = 0^\circ$ ($\theta = 60^\circ$) 11.70 cm (11.05 cm) of PMMA absorber with a corresponding $r_{H_2O} = 13.63$ cm ($r_{H_2O} = 12.87$ cm) was placed in front of the multiwell plate. For angular irradiation at $\theta = 60^\circ$ the multiwell plate was placed at an angle of $\gamma = 30^\circ \pm 5^\circ$ ($\gamma = 90^\circ - \theta$, defined for practical purpose) toward the incident ion beam. The different PMMA thicknesses result from the different thicknesses of the bottom of the multiwell plates (polystyrene, $\theta = 0^\circ$: $r_{H_2O} = 1.2$ mm, $\theta = 60^\circ$: $r_{H_2O} = 2.5$ mm). The air gap between the culture well and the PMMA was not considered in the total r_{H_2O}. The amount of material in the beam from vacuum exit window to isocenter corresponds to a r_{H_2O} of 2.89 mm.

2.3. FNTD and cell layer read-out

For the sequential read-out of the cell-coated FNTD we used the Zeiss LSM 710 ConfoCor 3 confocal microscopy equipped with a z-piezo stage, 63×/1.45 numerical aperture (NA) Oil DIC M27 objective, photomultiplier tubes and avalanche photo diodes. We used the protocols as previously described in Greilich *et al* (2013) and Niklas *et al* (2013a). For the read-out of the angular (perpendicular) irradiated FNTDs the excitation laser power of the 633 nm Helium–Neon laser was adjusted to 100% (100%) transmission, pixel dwell time τ was set to 4.97 μs (2.80 μs) and the line-scanning repetition R was limited to 4 (4). For the cell layer acquisition (HOECHST 33342) we used a 405 nm diode laser line (30 mW, 4% transmission) with $\tau = 2.80$ μs and $R = 4$. The microscope detector pinhole aperture was set to 1 Airy disk unit. For angular (perpendicular) irradiated FNTDs a single imaging field comprised 1300 × 1300 pixel (1152 × 1152 pixel) with a pixel size of 0.104×0.104 μm^2 (0.117×0.117 μm^2). The acquired image stacks of the angular irradiated FNTDs covered an axial range of approximately 90 μm (measured from the detector surface). Concerning the perpendicular irradiated FNTD the image stacks covered an axial range of approximately 120 μm. In both

cases the z-interval $\widehat{\Delta z}$ between two consecutive image planes was adjusted to 3 μm. For imaging, the cell-coated FNTD was placed in uncoated glass bottom culture dish (MatTek Corp., Part No. P35G-1.5-20C) with the cell layer facing the glass bottom. The culture dish was filled with PBS. Anisotropic fluorescence properties of Al_2O_3:C,Mg crystals (Sanyal and Akselrod 2005, Greilich *et al* 2013) were neglected. Zeiss Immersol^{TM}518 F ($n = 1.51$ for $\lambda = 643.8$ nm at 23 °C) was used as an immersion medium. The images acquired were stored with a bit depth of 16-bit in the LSM format.

The position of the polished FNTD surface was identified by using the HOECHST 33342 fluorescence signal from the nuclear staining. It disappears at the transition into the FNTD crystal. In addition, excitation by 405 nm causes a photoionization of the pristine F_2^{2+}(2Mg) aggregate defects located in close vicinity to the detector surface hence increasing the background in the HOECHST 33342 channel.

2.4. Detection of the ion track centers

For image segmentation the acquired 16-bit integer FNTD images were converted into floating point data (with pixel values in the interval [0; 1]). A window limited to 30 × 30 pixels for perpendicular and 120 × 30 pixels for angular irradiation was used to define regions of interest (ROIs) within a plane of the FNTD image stack. Each ROI contained a single track spot. Thresholding in the ROIs was applied to identify all track spot centers in the acquired image stack belonging to a single particle trajectory. Due to secondary electron tracks sprouting from a track spot center each ROI can contain several local intensity maxima dividing it into several sub-areas. The largest area was isolated and considered to account for the ion track core (a halo of secondary electrons around the center of a track spot, figure 3(a)). The smaller areas mainly arise from dense energy depositions induced by strongly scattered secondary electrons having enough energy to leave the ion track core. We compared three different approaches to identify the center of a track spot.

(A) Detection of intensity-weighted centroids applying a global threshold (*iw centroid*): all pixels within the ROI with values greater than a manually defined global threshold of 0.4 were considered for the calculation of the intensity-weighted centroid.
(B) Detection of intensity-weighted centroids applying a dynamic threshold (*rel thres*): the threshold was set to 2/3 of the maximum pixel value within an ROI.
(C) Detection of the absolute intensity maximum (*abs max*): the pixel with the maximum value within the ROI was considered as the track spot center.

No background correction of the FNTD raw images was applied.

2.5. Fitting and extrapolation procedure

For reconstruction of the ion trajectory in 3D we assumed the ion to follow a straight line. A line was expected as due to the high energies of the ions, multi-Coulomb scattering of the projectile in the crystal lattice is very small. Due to statistical variation in energy deposition and inhomogeneities of the color-center density, only uncertainties in the horizontal coordinates (x,y) of the ion track centers were taken into account. Uncertainty in z by the high-precision z-piezo stage (in the nm range) were neglected. The fitting procedure was split up into two separate LRA (using least-square estimation (Montgomery *et al* 2006)) for the x- and y-coordinates respectively (figure 2(b)):

$$x(z) = a_x + b_x \cdot z \tag{1}$$

$$y(z) = a_y + b_y \cdot z. \tag{2}$$

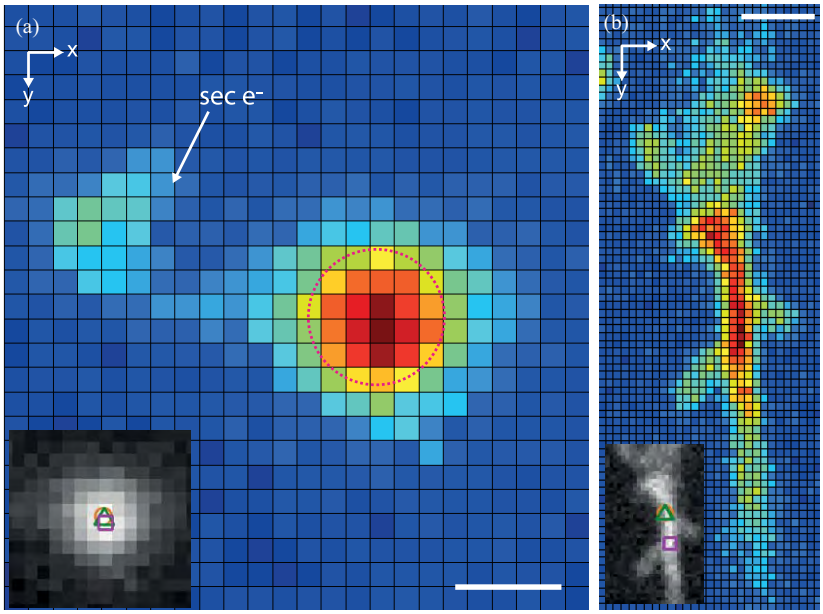

Figure 3. Intensity profile of FNTD read-out signal after (a) perpendicular ($\theta = 0^\circ$) and (b) angular irradiation ($\theta = 60^\circ$). The track core (masked by the point spread function of the imaging system (Niklas *et al* 2013b)) is indicated by the red dashed circle. In both cases secondary electron trajectories are sprouting from the symmetrical and ellipsoidal track spot. Inserts: the track spot centers detected by identifying the intensity-weighted centroid applying a manually defined threshold (ocher circle), the absolute maximum (magenta rectangle) and by identifying the intensity-weighted centroid applying dynamic thresholding (green triangle) do not coincide. Scale bars, (a) 0.5 μm and (b) 1 μm.

The flight direction of the incident ions was parameterized by θ and ϕ. θ (figure 2(a)) was calculated by

$$\theta = 90^\circ - \gamma, \tag{3}$$

$$\gamma = \arctan[(\tan^{-2}\alpha + \tan^{-2}\beta)^{-0.5}] \tag{4}$$

with $\tan\alpha = b_x$ and $\tan\beta = b_y$. ϕ was calculated by

$$\phi = \arctan[\tan(\alpha)/\tan(\beta)]. \tag{5}$$

Fitting of the particle tracks was carried out in a total range in z of 60 μm partly starting at different depths in the FNTD. This is the range allowing to track a traversing ion within a single imaging field (135 × 135 μm^2) under angular irradiation (for greater ranges the imaging field has to be moved, i.e. tile scans have to be performed).

The ion trajectories obtained by fitting were extrapolated into the A549 cell layer of 10 μm thickness (nominal thickness without correction for distortion, see section 2.6 below) grown on top of the FNTD. The 95% prediction intervals $\mathrm{PI}_{x,y}$ on future observation (x_0, y_0) with $\mathrm{PI}_{x,y} = [x_0 - a_x - b_x \cdot z_0, y_0 - a_y - b_y \cdot z_0]$ were calculated by

$$\mathrm{PI}_x = s \cdot t_{n-2,97.5} \cdot \sqrt{1 + \frac{1}{n} + \frac{1}{\hat{s}}(z_0 - \bar{z})^2} \tag{6}$$

$$s = \sqrt{\frac{\sum_{i=1}^{n}(a_x + b_x \cdot z_i - x_i)^2}{n-2}} \tag{7}$$

$$\hat{s} = \sum_{i=1}^{n} (z_i - \bar{z})^2 \tag{8}$$

$$\bar{z} = \frac{1}{n} \cdot \sum_{i=1}^{n} z_i \tag{9}$$

and analogue for PI_y using y_i, a_y and b_y in (7). Parameter n is the number of track spot centers (with coordinates x_i, y_i, z_i) considered for the fit, and $t_{n-2,97.5}$ is the 97.5% quantile of the t-distribution with $n-2$ degrees of freedom. We assumed that all extrapolations start at the same depth, 3 μm below the FNTD crystal surface.

Accuracy of ion track reconstruction in 3D was expressed by $\Delta\theta$, $\Delta\phi$ (95% confidence intervals gained by the LRA) and $PI_{x,y}$. To study the impact of the parameter n on accuracy we varied the distance in z between two consecutive track spots Δz (nominal distance without correction for distortion, see section 2.6 below). We further compared three different approaches for the identification of the track spot center coordinates (*iw centroid, rel thres, abs max*, see section 2.4):

(i) $\Delta z = 3$ μm, $n = 21$ track spots
(ii) $\Delta z = 6$ μm, $n = 11$ track spots
(iii) $\Delta z = 15$ μm, $n = 5$ track spots

We analyzed 20 tracks each for angular and perpendicular irradiated FNTDs.

2.6. Correction for axial geometrical distortion

In the optical path of the confocal imaging a mismatch in index of refraction occurs at the interface between the immersion oil and cell layer and at the interface between cell layer and FNTD. The refractive index of the glass bottom dish and the immersion oil was assumed to equal. The mismatch causes axial distortion of the nominal focal position (position in z without spherical aberration) from the actual one (presence of spherical aberrations) (Jacobsen and Hell 1995, Van Elburg *et al* 2007). For correction of the negative mismatch ($n_{oil} = 1.51 > n_{cell} = 1.47$ (Hell *et al* 1993)) occurring at the oil–cell layer boundary we used an improved linear correction method for high NA lenses as previously described in Van Elburg *et al* (2007). The axial scaling factor (ASF) to recalculate the nominal focal position z_1 in the cell layer was determined by:

$$ASF_1 = c_1 \Delta n / n_{oil} + c_2 \arctan(c_3 \Delta n / n_{oil}) \tag{10}$$

with $c_1 = 1.132$, $c_2 = 0.0065$, $c_3 = 100$ and $\Delta n = (n_{cell} - n_{oil})$. To account for the positive mismatch at the cell layer–FNTD boundary ($n_{Al_2O_3:C,Mg} = 1.76 > n_{cell}$) we used the paraxial approximation $ASF_2 = n_{Al_2O_3:C,Mg}/n_{cell}$. We used this approximation as $n_{Al_2O_3:C,Mg}$ exceeds the range of mismatch being considered for the improved linear correction method (Van Elburg *et al* 2007) and as it was previously approved to approximate experimental results well (Hell *et al* 1993). The position in z of the actual focal point z_{act} (origin is at the bottom of the culture dish) was then calculated by

$$z_{act}(z) = ASF_1 \cdot z_1 + ASF_2 \cdot z \tag{11}$$

with z_1 being the nominal thickness of the cell layer (distance between the dish bottom and the detector surface) and z being the nominal position in the FNTD (measured from the detector surface). The aqueous medium between dish bottom and cells was neglected in the correction for axial distortion.

Uncertainties in the position of the surface Δs translate into an error $\hat{x}$ of the location of the track in the horizontal:

$$z_{\mathrm{act}}(z, \Delta s) = z_{\mathrm{act}}(z) \pm (\mathrm{ASF}_1 - \mathrm{ASF}_2)\Delta s \tag{12}$$

$$\hat{x} = (\mathrm{ASF}_1 - \mathrm{ASF}_2)\Delta s / \tan(90^\circ - \theta) \tag{13}$$

starting from

$$z_{\mathrm{act}}(z) = \mathrm{ASF}_1(s - o_1) + \mathrm{ASF}_2[(\hat{n} - 1)\widehat{\Delta z} - (s - o_2)] \tag{14}$$

and defining $z := (\hat{n}-1)(\widehat{\Delta z})$ as a function of the actual plane number $\hat{n}$ of the acquired image stack and the interval between two consecutive image planes $\widehat{\Delta z}$. o_1 and o_2 are the respective positions of the first image plane of the cell and FNTD image stack.

3. Results

3.1. Intensity profile of a track spot

In figure 3 track spots—the ion's footprint left in the Al_2O_3:C,Mg crystal—resulting from irradiation perpendicular ($\theta = 0^\circ$) and angular ($\theta = 60^\circ$) toward the FNTD surface are shown. Under perpendicular irradiation the track spots have an almost radial symmetric intensity profile with a steep intensity gradient in the track core (halo around the track spot center) and branching trajectories from secondary electrons of higher energy. Their local intensity maxima are due to the track ends.

Under angular irradiation the track spots are deformed into ellipsoidal objects extended along beam direction (y) with tattered edges and with branching secondary electron trajectories. The electron trajectories exhibit a broad angular distribution causing a more complex geometry of the track spots. The track spots also exhibit an intensity rise with a global maximum most probably accounting for the angular track core. On average an elongated track spot has the size of approximately $7 \times 0.5\ \mu\mathrm{m}^2$—compared to the diameter of 0.9 μm of a symmetrical track spot.

The insets in figures 3(a) and (b) show the examples of the track spot centers for all three identification approaches (*iw centroid, rel thres, abs max*, see section 2.4 above). Under perpendicular and angular irradiations the positions of the intensity-weighted track spot centers detected by applying a global threshold and dynamic thresholding are nearly identical. Larger deviations from these positions occur for identifying the absolute intensity maximum. The spatial mismatch is much more pronounced under angular than under perpendicular irradiation.

3.2. Residuals of the fit

For all LRA (angular and perpendicular irradiation) the residual plots generally displayed a normal distribution (not shown). figure 4 presents the mean absolute residuals (in an initial step the absolute residuals corresponding to a single fit were averaged) including the standard error of the mean (SEM).

In the case of angular irradiation the residuals in x (perpendicular to beam direction) and in y (along beam direction) resulting from identification approach (A) and (B) (*iw centroid, rel thres*) fluctuate around 0.10 μm and 0.58 μm respectively for all Δz (figure 4(a)). The

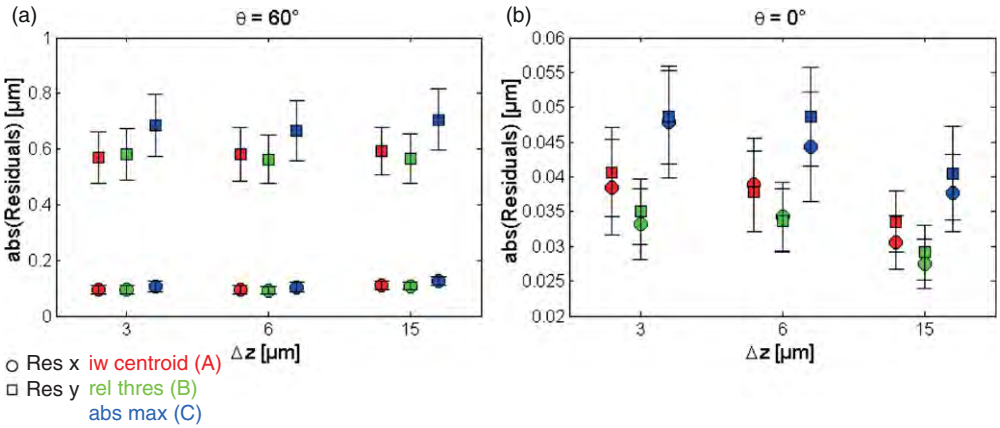

Figure 4. Mean absolute residuals in x (circles) and y (solids) resulting from different fitting procedures. The distance Δz between two consecutive track spots was varied and different approaches to detect the track spot centers were used (red: intensity-weighted centroid, green: dynamic thresholding, blue: absolute maximum). The error bars are the standard errors of the mean. (a) angular irradiation, $\theta = 60°$ (b) perpendicular irradiation, $\theta = 0°$.

residuals concerning identification of the absolute maximum (*abs max*, approach (C)) are larger (x: $\approx$ 0.12 μm, y: $\approx$ 0.68 μm). SEMs in x ($\leqslant$0.02 μm) and y ($\approx$0.10 μm) approximately equal for all Δz and all identification approaches; the largest values are obtained for approach (C).

For perpendicular irradiation the residuals in x and in y, resulting from identification approach (A) and (B) ($\Delta z = 3$ and 6 μm) fluctuate between 0.03 μm and 0.04 μm and decrease for $\Delta z = 15$ μm (figure 4(b)). Concerning identification approach (C) the residuals in x and in y lie between 0.04 μm and 0.05 μm. All SEMs are smaller than 0.01 μm.

3.3. Accuracy of ion track reconstruction in 3D

For angular irradiation the mean values $\theta = 59.03°$ and $\phi = 84.68°$ defining the direction of the traversing ions differ of maximum 0.07° and 0.01° respectively for all LRA (table 1). The error $\Delta\theta$, figure 5(a), is smallest (0.89°) for approach (A) at $\Delta z = 3$ μm and is increasing to 3.45° for approach (C) at $\Delta z = 15$ μm. Except for $\Delta z = 15$ μm, $\Delta\phi$ is smaller than 0.2° for all LRA (figure 5(b)). Concerning the mean PIs (figures 6(a), (b) and table 1) in the cell layer of 10 μm thickness on top of the FNTD the values in x are smaller than 0.4 μm ($\Delta z < 15$ μm, for all identification approaches) and are increasing to 0.77 μm for approach (C) at $\Delta z =$ 15 μm. PI_y is has its lowest value (1.72 μm) for approach (A) at $\Delta z = 3$ μm and is increasing to 4.58 μm for approach (C) at $\Delta z = 15$ μm.

Concerning perpendicular irradiation, $\theta \approx 1.22°$ differs less than 0.02° for all LRA (table 2). Azimuthal angle ϕ lies between 45° and 46°. For $\Delta z < 15$ μm and all identification approaches $\Delta\theta$ is smaller than 0.15° and is increasing to 0.26° for $\Delta z = 15$ μm (approach (C), figure 5(c)). $\Delta\phi$ covers a broad range—between 1.53° and 4.77° (figure 5(d)). The mean PIs in x and in y are generally much smaller than 0.3 μm (figures 6(c), (d) and table 2).

Both, the distributions of $\Delta\theta$ and $\Delta\phi$ (perpendicular and angular irradiation) indicated by their standard deviation (s.d.) and mean values show a steep rise between $\Delta z = 6$ μm and $\Delta z = 15$ μm. This is independent of the identification approach used (figure 5). The effect is especially pronounced under angular irradiation. The mean PIs behave similarly (figure 6).

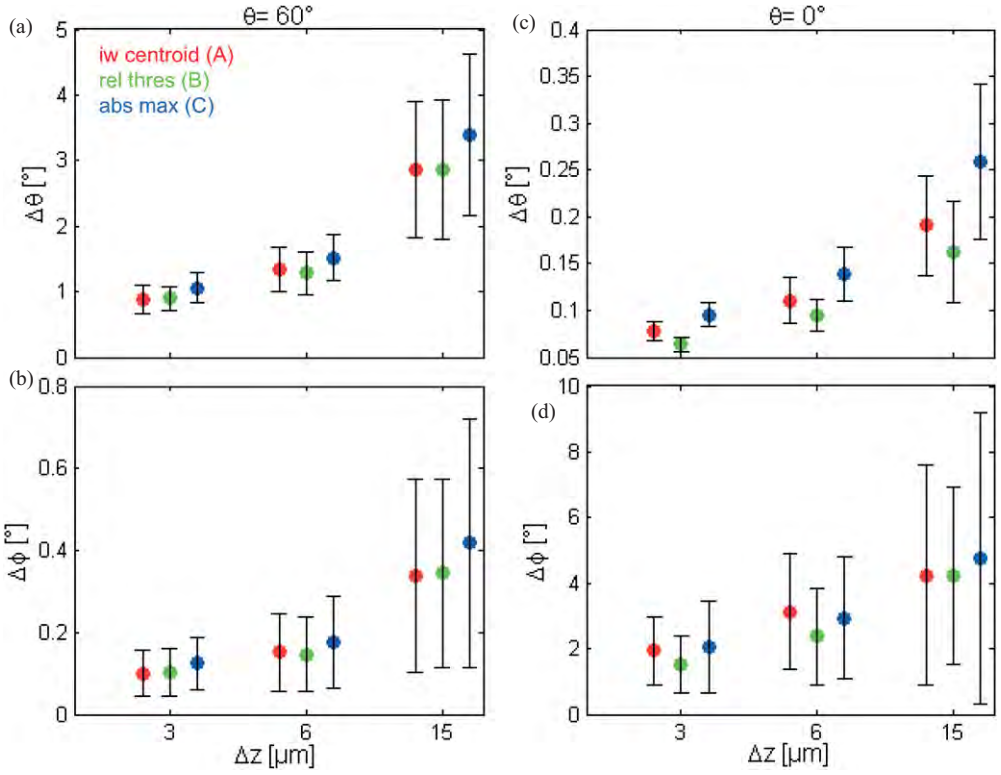

Figure 5. Errors $\Delta\theta$ and $\Delta\phi$ of the different fitting procedures (red: intensity-weighted centroid, green: dynamic thresholding, blue: absolute maximum). Δz is the distance in z between two track spots. (a)–(b) Angular irradiation, $\theta = 60°$, (c)–(d) perpendicular irradiation, $\theta = 0°$. The error bars are the standard deviations (s.d.).

Table 1. Angular irradiation, $\theta = 60°$. Accuracy of ion track reconstruction using different fitting procedures. Δz: distance in z between two track spots. The errors are the standard deviations (s.d.). Total range in z: 60 μm.

	θ (°)	$\Delta\theta$ (°)	ϕ (°)	$\Delta\phi$ (°)	PI_x (μm)	PI_y (μm)
$n = 21$ track spots,	$\Delta z = 3\,\mu$m					
iw centroid (A)	58.97	0.89 ± 0.22	84.69	0.10 ± 0.06	0.28 ± 0.12	1.72 ± 0.43
rel thres (B)	58.98	0.90 ± 0.19	84.69	0.10 ± 0.06	0.28 ± 0.10	1.74 ± 0.37
abs max (C)	58.98	1.06 ± 0.23	84.69	0.13 ± 0.06	0.32 ± 0.11	2.07 ± 0.44
$n = 11$ track spots,	$\Delta z = 6\,\mu$m					
iw centroid (A)	59.00	1.36 ± 0.34	84.68	0.16 ± 0.09	0.35 ± 0.17	2.14 ± 0.54
rel thres (B)	59.01	1.23 ± 0.33	84.68	0.15 ± 0.09	0.33 ± 0.13	2.01 ± 0.53
abs max (C)	59.03	1.54 ± 0.37	84.68	0.18 ± 0.11	0.38 ± 0.17	2.42 ± 0.58
$n = 5$ track spots,	$\Delta z = 15\,\mu$m					
iw centroid (A)	59.08	2.84 ± 1.03	84.67	0.34 ± 0.23	0.68 ± 0.45	3.76 ± 1.37
rel thres (B)	59.09	2.79 ± 1.08	84.68	0.33 ± 0.24	0.66 ± 0.33	3.69 ± 1.45
abs max (C)	59.09	3.45 ± 1.21	84.68	0.43 ± 0.29	0.77 ± 0.47	4.58 ± 1.62

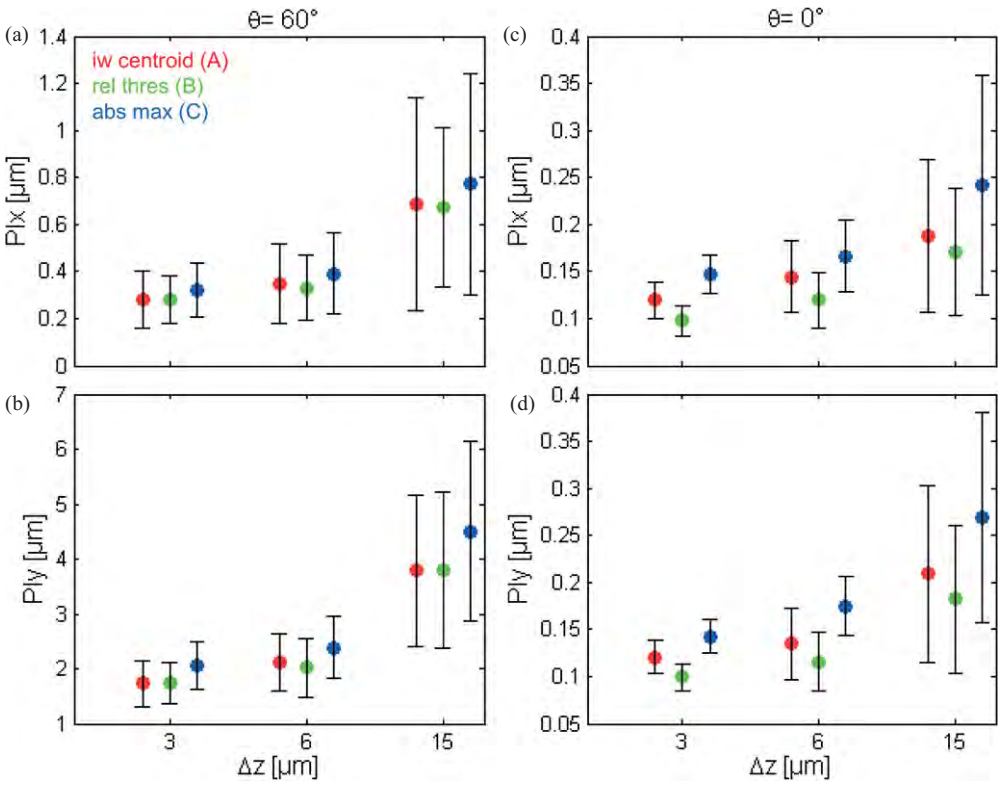

Figure 6. Mean prediction intervals for x and y resulting from the extrapolation of the particle track into a cell layer of 10 μm thickness for different fitting procedures (red: intensity-weighted centroid, green: dynamic thresholding, blue: absolute maximum). Δz is the distance in z between two track spots. (a)–(b) Angular irradiation, $\theta = 60°$, (c)–(d) perpendicular irradiation, $\theta = 0°$. The error bars are the s.d.

Table 2. Perpendicular irradiation, $\theta = 0°$. Accuracy of ion track reconstruction using different fitting procedures. Δz: distance in z between two track spots. The errors are the s.d. Total range in z: 60 μm.

	θ (°)	$\Delta\theta$ (°)	ϕ (°)	$\Delta\phi$ (°)	PI_x (μm)	PI_y (μm)
$n = 21$ track spots,	$\Delta z = 3\,\mu$m					
iw centroid (A)	1.20	0.08 ± 0.01	45.16	1.95 ± 1.04	0.12 ± 0.02	0.12 ± 0.02
rel thres (B)	1.21	0.06 ± 0.01	44.99	1.53 ± 0.87	0.10 ± 0.02	0.10 ± 0.01
abs max (C)	1.22	0.10 ± 0.01	45.30	2.05 ± 1.42	0.15 ± 0.02	0.14 ± 0.02
$n = 11$ track spots,	$\Delta z = 6\,\mu$m					
iw centroid (A)	1.21	0.11 ± 0.02	44.95	3.14 ± 1.78	0.14 ± 0.04	0.13 ± 0.04
rel thres (B)	1.22	0.09 ± 0.02	44.92	2.38 ± 1.47	0.12 ± 0.03	0.12 ± 0.03
abs max (C)	1.24	0.14 ± 0.03	45.94	2.94 ± 1.86	0.17 ± 0.04	0.17 ± 0.03
$n = 5$ track spots,	$\Delta z = 15\,\mu$m					
iw centroid (A)	1.21	0.19 ± 0.05	45.21	4.23 ± 3.36	0.19 ± 0.08	0.21 ± 0.09
rel thres (B)	1.22	0.16 ± 0.05	45.39	4.21 ± 2.71	0.17 ± 0.07	0.18 ± 0.08
abs max (C)	1.24	0.26 ± 0.08	45.70	4.77 ± 4.45	0.24 ± 0.12	0.27 ± 0.11

4. Discussion

Accuracy of ion track reconstruction in 3D using the FNTD depth information is strongly influenced by the irradiation angle θ and therefore by complexity of the intensity profile of a track spot as well as by the approach for identification of its center.

4.1. Intensity profile of a track spot

The size and shape of a track spot depends on the energy of the incident ions (Akselrod and Sykora 2011, Niklas *et al* 2013b) and θ governing the geometrical cross section of the traversing particles with the detector material. High-energy carbon ion irradiation produces a high density of secondary electrons of low energies responsible for the generally symmetrical as well as ellipsoidal intensity profile of the track spots (figure 3). The sprouting electron trajectories with a broad angular distribution are caused by δ electrons having enough energy to leave the track core. These trajectories, although less probable, and their random formation (due to frequent scattering of the δ electrons) distort the original symmetrical intensity profile.

The track spots under angular irradiation seem to comprise more sprouting electron trajectories than the symmetrical track spots. Due to a greater geometrical cross section the probability of producing fast δ electrons increases including the formation of tattered track spot edges. In addition, electron trajectories of neighboring ion traversals from above or below crossing as well as being scattered in the image plane are being detected. On the contrary, under perpendicular irradiation mainly the electron trajectories perpendicular to the flight direction of the incident ion are visible.

The track spot is masked by the point spread function (PSF) of the imaging system (figure 3) (Niklas *et al* 2013b). The PSF is distorted by the refractive index mismatch at the oil–cell layer and cell layer–Al_2O_3:C,Mg interface causing spherical aberrations (Carlsson 1991, Hell *et al* 1993, Jacobsen and Hell 1995). Besides a decrease of image brightness (a result of the confocal arrangement), the aberrations could also account for a blurred appearance of the track spots (including the tattered edges) by an increasing FWHM of the PSF and appearance of secondary maxima (Hell *et al* 1993). A deconvolution could increase resolution only to some extend as the PSF in the corresponding focal depth and the actual structure of a track spot have to be exactly known.

4.2. Ion track center assessment

The thresholds-based methods (A) and (B) (*iw centroid, rel thres*) using a value of 0.4 for identifying intensity-weighted centroids and 2/3 of the maximum pixel value within an ROI (dynamic thresholding) showed best suitability for carbon ion irradiation and minimize the probability to detect δ electron structures (including their Bragg peaks) as well as the tattered track spot edges. These structures would shift the actual position of the track center. As the gradient of the intensity profile is relatively steep, 2/3 of the maximum is not too high running the risk of approaching the global maximum which is likely not to coincide with the center of the track spot core. Statistical fluctuation of energy deposition and local fluctuation of the color-center density could be the main reason for this mismatch. Weighting by intensity seems to approach the actual track core best. This coincides well with smaller residuals (figure 4) and hence more accurate track reconstruction (figures 5 and 6) than the detection of the absolute intensity maximum (*abs max*, method (C)). In addition, dynamic thresholding has the advantage of responding to different intensity profiles (variation in the maximum intensity (Niklas *et al* 2013b)) by different particle types or energies within a FNTD image.

Table 3. Perpendicular irradiation, $\theta = 0°$. Accuracy of ion track reconstruction using different fitting procedures. Δz: distance in z between two track spots. The errors are the s.d. Total range in z: 114 μm.

	θ (°)	$\Delta\theta$ (°)	ϕ (°)	$\Delta\phi$ (°)	PI$_x$ (μm)	PI$_y$ (μm)
$n = 39$ track spots,	$\Delta z = 3$ μm					
iw centroid (A)	1.17	0.03 ± 0.005	45.63	0.74 ± 0.45	0.11 ± 0.02	0.11 ± 0.02
rel thres (B)	1.17	0.03 ± 0.005	45.53	0.63 ± 0.42	0.10 ± 0.02	0.10 ± 0.01
abs max (C)	1.18	0.04 ± 0.005	45.53	0.84 ± 0.61	0.14 ± 0.02	0.14 ± 0.02

Under angular irradiation it is more difficult to define the actual track spot core. A fitting of the intensity profile of a track spot by a 2D Gaussian function (Akselrod *et al* 2006, Niklas *et al* 2013b) (symmetrical for perpendicular irradiation, elliptical for angular irradiation) and the detection of its maximum could improve the subsequent LRA.

4.3. Accuracy on particle track reconstruction in 3D

Complexity of the track spot geometry and hence the irradiation angle θ have a major impact on accuracy expressed by $\Delta\theta$, $\Delta\phi$ and PI. The radial symmetrical intensity profile ($\theta = 0°$) is reflected in nearly identical residuals in x and in y (figure 4(b)) for all LRA. On the contrary the elongation (along beam direction) and much higher complexity of the track spots under angular irradiation ($\theta = 60°$) causes much greater discrepancy between the residuals in x and in y—by a factor of approximately 6—irrespective of the identification approach of the track spot center (figure 4(a)). This is directly reflected in the increased error $\Delta\theta$ by a factor of approximately 10 (comparing $\theta = 60°$ and $\theta = 0°$, figures 5(a) and (c)). This is also reflected in much greater PIs (figure 6), especially for PI$_y$ under angular irradiation being more than ten times larger than the symmetrical PIs under perpendicular irradiation.

The surprisingly great values of $\Delta\phi$ under perpendicular irradiation (figure 5(d)) arise from the narrow distribution of the projections of the track spots onto the yz plane. Small fluctuations have a great impact leading to large variations in the coefficient interval of b_y in the LRA (equation (2)). To gain more reliable values and to decrease $\Delta\phi$ below 1° we increased the number of track spots by extending the total range in z for the LRA for perpendicular irradiation to 114 μm with $\Delta z = 3$ μm (table 3).

To principally minimize the PIs and irrespective of the irradiation angle it is favorable to start the FNTD read-out near the detector surface. This assures a minimal extrapolation interval into the cell layer. This also reduces the PIs as the interval between the mean z-coordinate of identified track spots and z-coordinate of extrapolation gets minimized (equation (6)).

The strong decrease in accuracy (and larger s.d.) for $\Delta z = 15$ μm, all identification approaches (figures 5 and 6), could arise from the insufficient averaging and the statistical nature of energy deposition. Under perpendicular irradiation a reasonable trade-off between fast detector read-out and high accuracy is yet possible by increasing Δz to 15 μm (figure 5(c)). $\Delta\theta$ increases but is still less than 0.3°. $\Delta\phi$ has little significance. The PIs are however increasing as they depend on the inverse number of track spots considered for the LRA. The surprising decrease of the residuals ($\Delta z = 15$ μm, all three identification approaches, figure 4(b)) has no impact on the increase of $\Delta\theta$, $\Delta\phi$ and PIs.

4.4. Correction of axial geometrical distortion

The distortion induced by refractive index mismatch only affects the axial position of the focal point and hence θ—the trajectory of the particles. Introducing nonlinear correction (Van

Elburg *et al* 2007) could further improve reconstruction accuracy to some extent especially for larger angles. As the refractive index differs for individual organelles (Beuthan *et al* 1996) the actual correction term for the cell layer has a spatial dependence. To reduce the impact of refractive index mismatching on track reconstruction especially for angular irradiation, 2,2′-thiodiethanol (98%, $n = 1.518$) can be used as mounting medium for the cell layer during the confocal read-out (Staudt *et al* 2007). As its refractive index equals with the refractive index of the immersion oil only the oil–Al_2O_3:C,Mg boundary has to be considered for axial correction. To further reduce spherical aberrations, perpendicular irradiation should be employed in particular for live cell imaging. Despite the presence of the refractive index mismatch at the cell–Al_2O_3:C,Mg boundary the nominal can be approximated with the actual focal position.

Concerning uncertainty in the position of the FNTD surface Δs, the error term $(\mathrm{ASF}_1 - \mathrm{ASF}_2)\Delta s$ in (12), which affects the actual focal position z_{act} is independent of z and does not influence the LRA and thus trajectory of the incident ions (parameterized by θ and ϕ). The resulting error $\hat{x}$ (13) of the position of the ion track in the horizontal direction is governed by θ and the product $(\mathrm{ASF}_1 - \mathrm{ASF}_2)\Delta s$. $\Delta s = 1\ \mu$m at $\theta = 60^\circ$ yields $\hat{x} = 0.40\ \mu$m. For shallow irradiation angles, i.e. $\theta < 45^\circ$, $\hat{x}$ decreases steeply as long as $(\mathrm{ASF}_1 - \mathrm{ASF}_2) < 1$. $\hat{x}$ becomes yet more relevant if the ion traversal in the intracellular space has to be localized.

5. Conclusions

It is possible to perform accurate ion track reconstruction in 3D and extrapolate an ion's trajectory into a cell layer covering the FNTD by using depth information provided by detector read-out. The accuracy of the track reconstruction procedure strongly depends on the irradiation angle θ and by the approach used to identify individual track spot centers. The use of intensity-weighted centroids and dynamic thresholding yield the highest accuracy. Steep irradiation angles distort the otherwise symmetrical track spots, resulting in reduced accuracy of centroid prediction. To achieve the desired accuracy in determining the angle θ with an error smaller than 1° under angular irradiation at $\theta = 60^\circ$ the intensity-weighted centroid detection and a 21 image stack separated by $\widehat{\Delta z} = 3\ \mu$m was found as the best set of image acquisition and processing parameters. Increasing $\widehat{\Delta z}$ to 6 μm (i.e. half the number of track spots) deteriorates the accuracy, i.e. $\Delta\theta$ and PI, roughly by 30% and 20% respectively. Concerning angles of irradiation with θ close to 0° and using the same fit parameters, $\Delta\theta$ decreases by a factor of at least 10 with nearly symmetrical lateral error distribution.

The required increase in accuracy of track reconstruction also increases the total read-out time of the detector. To further improve accuracy if necessary one could extend the total axial range of the image stack, to increase the number of images and decrease the image depth increment between two consecutive image planes ($\widehat{\Delta z}$). This, however, is more time consuming. Naturally the total microscope time is directly affected by the acquisition time of a single image plane (mainly governed by laser power p, dwell time τ, number of rescans R and total number of spots per imaging field (Greilich *et al* 2013)) influencing the signal-to-noise ratio and thus the quality of the detection of the track spot center.

The ability of FNTD technology to be used as a substrate to be coated with living tissue and to provide accurate 3D ion track reconstruction makes it a powerful tool for radiobiological investigations in clinical ion beams (Niklas *et al* 2013a). The uncertainties in ion track reconstruction (PI_x and PI_y, tables 1–3) in the cell layer are smaller than the dimensions of a single cell and even of individual organelles, e.g. nucleus. This opens the possibility to isolate individual cellular organelles being traversed by ions and to correlate the corresponding local physical energy deposition to the subsequent cellular response. The FNTD could also be

implanted *in vivo* (e.g. in the tumor volume) to elucidate clinically relevant information on a plethora of particle variables in the Bragg peak.

Acknowledgments

We are grateful to S Brons for generously providing support and technical irradiation assistance at the Ion-Beam Therapy Center of Heidelberg University Hospital. We should also like to thank F Bestvater and M Brom of the DKFZ's light microscopy core facility for their enthusiasm and unflagging support. MN is funded by the fellowship from the Helmholtz International Graduate School for Cancer Research at the German Cancer Research Center. SG and AA are supported by the German Cancer Research Center. OJ is supported by the University Hospital Heidelberg. MA is supported by Landauer R&D money. JB is supported by Oklahoma State University. This work was supported by the Helmholtz Association (translating hadron therapy from basic research to clinical application, VH-VI-303, SG), German Research Council (DFG, KFO214), National Aeronautics and Space Administration under NSCOR grant no. NNJ06HA28G, the German Krebshilfe (Deutsche Krebshilfe, Max-Eder 108876), intramural Grants of the National Center for Tumor diseases (NCT, Heidelberg, Germany) and the German Federal Ministry of Research and Technology (Bundesministerium für Bildung und Forschung—BMBF 03NUK004C). The authors declare that they have no competing financial interests.

Authors' contributions

MN performed experiments, analyzed data and wrote the paper. JB participated in the axial geometrical correction. MA developed the crystal (FNTD) material and FNTD imaging technique. SG initiated the project, MN, AA, OJ and SG designed experiments and interpreted the data. All authors edited the paper. All authors read and approved the final paper.

References

Akselrod G M, Akselrod M S, Benton E R and Yasuda N 2006 A novel Al_2O_3 fluorescent nuclear track detector for heavy charged particles and neutrons *Nucl. Instrum. Methods Phys. Res.* B **247** 295–306

Akselrod M S and Sykora G J 2011 Fluorescent nuclear track detector technology—a new way to do passive solid state dosimetry *Radiat. Meas.* **46** 1671–9

Bartz J A, Zeissler C J, Fomenko V V and Akselrod M S 2013 An imaging spectrometer based on high resolution microscopy of fluorescent aluminum oxide crystal detectors *Radiat. Meas.* (http://dx.doi.org/10.1016/j.radmeas.2013.01.041)

Beuthan J, Minet O, Helfmann J, Herrig M and Müller G 1996 The spatial variation of the refractive index in biological cells *Phys. Med. Biol.* **41** 369–82

Carlsson K 1991 The influence of specimen refractive index, detector signal integration, and non-uniform scan speed on the imaging properties in confocal microscopy *J. Microsc.* **163** 167–78

Greilich S, Osinga J-M, Niklas M, Lauer F M, Klimpki G, Bestvater F, Bartz J A, Akselrod M S and Jäkel O 2013 Fluorescent nuclear track detectors as a tool for ion-beam therapy research *Radiat. Meas.* (http://dx.doi.org/10.1016/j.radmeas.2013.01.033)

Hell S, Reiner G, Cremer C and Stelzer E H K 1993 Aberrations in confocal fluorescence microscopy induced by mismatches in refractive index *J. Microsc.* **169** 391–405

Jacobsen H and Hell S W 1995 Effect of the specimen refractive index on the imaging of a confocal fluorescence microscope employing high aperture oil immersion lenses *Bioimaging* **3** 39–47

Montgomery D C, Peck E A and Vining G G 2006 Introduction to linear regression analysis *Simple Linear Regression* ed D J Balding *et al* (Hoboken: Wiley) pp 12–34

Niklas M, Greilich S, Melzig C, Akselrod M S, Debus J, Jäkel O and Abdollahi A 2013a Engineering cell fluorescent ion track hybrid detectors *Radiat. Oncol.* **8** 141

Niklas M, Melzig C, Abdollahi A, Bartz J, Akselrod M S, Debus J, Jäkel O and Greilich S 2013b Spatial correlation between traversal and cellular response in ion radiotherapy—towards single track spectroscopy *Radiat. Meas.* (http://dx.doi.org/10.1016/j.radmeas.2013.01.060)

Osinga J-M, Akselrod M S, Herrmann R, Hable V, Dollinger G, Jäkel O and Greilich S 2013 High-accuracy fluence determination in ion beams using fluorescent nuclear track detectors *Radiat. Meas.* (http://dx.doi.org/10.1016/j.radmeas.2013.01.035)

Sanyal S and Akselrod M S 2005 Anisotropy of optical absorption and fluorescence in Al_2O_3:C,Mg crystals *J. Appl. Phys.* **98** 033518

Staudt T, Lang M C, Medda R, Engelhardt J and Hell S W 2007 2,2′-Thiodiethanol: a new water soluble mounting medium for high resolution optical microscopy *Microsc. Res. Tech.* **70** 1–9

Van Elburg H J, Kuypers L C, Decraemer W F and Dirckx J J J 2007 Improved correction of axial geometrical distortion in index mismatched fluorescent confocal microscopic images using high-aperture objective lenses *J. Microsc.* **228** 45–54

E

International Journal of Radiation Oncology biology • physics

www.redjournal.org

Biology Contribution

Subcellular Spatial Correlation of Particle Traversal and Biological Response in Clinical Ion Beams

Martin Niklas,[*,†] Amir Abdollahi, MD,[†,‡,§,||] Mark S. Akselrod,[#] Jürgen Debus, MD,[†,‡,§,||] Oliver Jäkel,[*,†,§,||] and Steffen Greilich [*,†]

[*]Division of Medical Physics in Radiation Oncology, German Cancer Research Center, Heidelberg, Germany; [†]German Cancer Consortium, National Center for Radiation Research in Oncology, Heidelberg Institute of Radiation Oncology, Heidelberg, Germany; [‡]Molecular and Translational Radiation Oncology, Heidelberg Ion-Beam Therapy Center, University of Heidelberg Medical School and National Center for Tumor Diseases, German Cancer Research Center, Heidelberg, Germany; [§]Department of Radiation Oncology and Radiation Therapy, University Hospital Heidelberg, Heidelberg, Germany; [||]Heidelberg Ion-Beam Therapy Center, Heidelberg, Germany; and [#]Stillwater Crystal Growth Division, Landauer Inc, Stillwater, Oklahoma

Received Jun 21, 2013, and in revised form Aug 5, 2013. Accepted for publication Aug 27, 2013.

Summary

The lack of sensitive biocompatible particle track detectors has so far limited parallel detection of physical energy deposition and biological response in clinical ion beam. We have developed a hybrid detector (Cell-Fit-HD) for spatial correlation of DNA damage response to the corresponding particle traversal. Cell-Fit-HD is a platform for radiobiological experiments

Purpose: To report on the spatial correlation of physical track information (fluorescent nuclear track detectors, FNTDs) and cellular DNA damage response by using a novel hybrid detector (Cell-Fit-HD).
Methods and Materials: The FNTDs were coated with a monolayer of human non-small cell lung carcinoma (A549) cells and irradiated with carbon ions (270.55 MeV u^{-1}, rising flank of the Bragg peak). Phosphorylated histone variant H2AX accumulating at the irradiation-induced double-strand break site was labeled (RIF). The position and direction of ion tracks in the FNTD were registered with the location of the RIF sequence as an ion track surrogate in the cell layer.
Results: All RIF sequences could be related to their corresponding ion tracks, with mean deviations of 1.09 μm and −1.72 μm in position and of 2.38° in slope. The mean perpendicular between ion track and RIF sequence was 1.58 μm. The mean spacing of neighboring RIFs exhibited a regular rather than random spacing.
Conclusions: Cell-Fit-HD allows for unambiguous spatial correlation studies of cell damage with respect to the intracellular ion traversal under therapeutic beam conditions. © 2013 Elsevier Inc.

Reprint requests to: Martin Niklas, German Cancer Research Center, Division of Medical Physics in Radiation Oncology (E040), Im Neuenheimer Feld 280, 69120 Heidelberg, Germany. Tel: (49) (0) 6221-42-2633; E-mail: m.niklas@dkfz.de

This work was supported German Research Council (grant KFO214); the German Krebshilfe (Deutsche Krebshilfe, Max-Eder 108876); intramural grants of the National Center for Tumor Diseases (Heidelberg, Germany); the Helmholtz Association (translating hadron therapy from basic research to clinical application, grant VH-VI-303 to S.G.); and the German Federal Ministry of Research and Technology (Bundesministerium für Bildung und Forschung grant 03NUK004C). M.N. is funded by a fellowship from the Helmholtz International Graduate School for Cancer Research at the German Cancer Research Center. S.G. and A.A. are supported by the German Cancer Research Center. J.D. and O.J. are supported by the University Hospital Heidelberg. M.A. is supported by Landauer research and development funds.

Conflict of interest: none.

Supplementary material for this article can be found at www.redjournal.org.

Acknowledgments—The authors thank S. Brons for generously providing support and technical irradiation assistance at the Ion-Beam Therapy Center of Heidelberg University Hospital; and F. Bestvater and M. Brom of the light microscopy core facility at the German Cancer Research Center for their enthusiasm and unflagging support.

Int J Radiation Oncol Biol Phys, Vol. 87, No. 5, pp. 1141−1147, 2013
0360-3016/$ - see front matter
http://dx.doi.org/10.1016/j.ijrobp.2013.08.043

to gain a deeper understanding between particle hits and resulting biological effects on the subcellular scale beyond the statistical relations we know today.

Introduction

The molecular mechanisms of radiobiological response to particle therapy and space radiation are hardly understood yet. To foster this area of research, we have developed a cell-fluorescent ion track hybrid detector (Cell-Fit-HD) for simultaneous assessment of cellular response and physical energy deposition parameters (such as location of ion traversal, ion type, energy, and linear energy transfer [LET] [1-3]) with a high spatial resolution (4). The Cell-Fit-HD is based on a fluorescent nuclear track detector (FNTD; Fig. 1A) (5) used as a substrate to coat with cell layers. Corresponding protocols have been described previously (4). Both the FNTD and the immunofluorescence markers for cellular response can be read out in situ by the same confocal laser scanning microscope (CLSM). The FNTD component provides 3D information on energy deposition from protons and ions whose flight path (track) can thereby be extrapolated into the attached cell layer with subcellular accuracy (6).

In this article we report on the spatial correlation of physical track information (FNTD) and cellular DNA damage response (DDR) by using Cell-Fit-HD. Deoxyribonucleic acid double-strand break (DSB) markers were used as a surrogate for the ions' flight paths through the nucleus. The locations to the tracks extrapolated from the FNTD were compared with the DSB marker locations.

Methods and Materials

Al_2O_3:C,Mg-based FNTD

Fluorescent nuclear track detectors consist of a single Al_2O_3:C,Mg crystal with F_2^{2+}(2Mg) cluster defects in the crystal lattice.

Under ionizing radiation these defects can be transformed into stable F_2^{+}(2Mg) centers. The radiation-transformed color centers absorb light in the band centered at 620 nm light, prompting fast 750-nm fluorescence. This allows for single track visualization of all particle types and energies found in particle therapy (1, 2, 5, 7) and single ion track reconstruction (6, 8) using CLSM for the read-out. The intensity of the read-out signal can be correlated to the linear energy transfer (LET) of the traversing ions (1, 5). The confocal read-out has a detection efficiency >99.83% and allows resolving of ion beam fluence up to $5 \cdot 10^7$ cm^{-2} (ie, clinical dose for C-12) (2). The heat-resistant detector allows for autoclaving, enabling its polished surface to be coated with a sterile cell layer (4).

Cell culture and cell coating

Human lung adenocarcinoma epithelial (A549) cells (obtained from Deutsche Sammlung von Mikroorganismen und Zellkulturen, Braunschweig, Germany) were cultured in Dulbecco's modified Eagle medium (Biochrom, Berlin, Germany, catalog no. FG 0415), supplemented with 10% fetal bovine serum (Biochrom, catalog no. S 0615) and 1% penicillin–streptomycin in humidified atmosphere under standard culture conditions (37°C, 5% CO_2). Cell-Fit-HDs were generated as previously described (4). Briefly, a plating density of $50 \cdot 103$ mL^{-1}, 0.5 mL per well was used to cover the autoclaved FNTDs with an A549 cell layer. The Cell-Fit-HDs were kept in humidified atmosphere until a confluent monolayer had developed after 48 hours. The culture medium was changed after 24 hours.

Irradiation in therapeutic ion beam and immunofluorescence staining

Carbon ion irradiation (initial 270.5 MeV u^{-1}, rising flank of the Bragg peak, r_{H2O} = 13.70 cm) of the hybrid detector was performed using the therapy beam of the Heidelberg Ion-Beam Therapy Center (HIT) at Heidelberg University Hospital. (Supplementary Material, available online). Irradiations were performed under a polar angle $\theta_{ion} \approx 60°$ and azimuth $\varphi_{ion} \approx 90°$ towards the incident ion beam using the protocols and setup as described in (4) and (6).

The cellular compartment of Cell-Fit-HD was fixed 15 min after irradiation with 4% paraformaldehyde for 10 min at room temperature and stained for γ-H2AX and HOECHST 33342 (Supplementary Material).

Cell-Fit-HD read-out

For the sequential read-out by the CLSM LSM 710 Confocor3 (Carl Zeiss, Jena, Germany) equipped with a piezo stage, 63×/1.40 N.A. oil objective, and avalanche photo diodes (APDs) we used the protocols as described in references 4 and 7. The FNTD was read out by the 633-nm HeNe laser (100% transmission); pixel dwell time τ and line-scanning repetition R were limited to 4.97 μs and 4, respectively. A long-pass emission filter >655 nm was used for APD detection.

The cell layer was imaged with a 405-nm diode laser (30 mW nominal power, 5.5% transmission) for HOECHST 33342 and with a 488-nm Argon laser (25 mW nominal power, 1.5% transmission) for Alexa Fluor 488. For both channels τ and R were set to 2.48 μs and 4, respectively. For detection of HOECHST 33342 (Alexa Fluor 488) the photomultiplier channel was used with detection window 410-495 nm (493-630 nm). Transmission photomultiplier detection was used in parallel for a subsequent image registration.

To increase the imaging field, 2 × 2 adjacent images (tile scan) were taken. A single imaging field comprised 1300 × 1300 pixels (pixel size: 0.1038 × 0.1038 μm^2). The FNTD (cell layer) image stack comprised 33 (67) image planes with a z-spacing of 3 μm (0.3 μm).

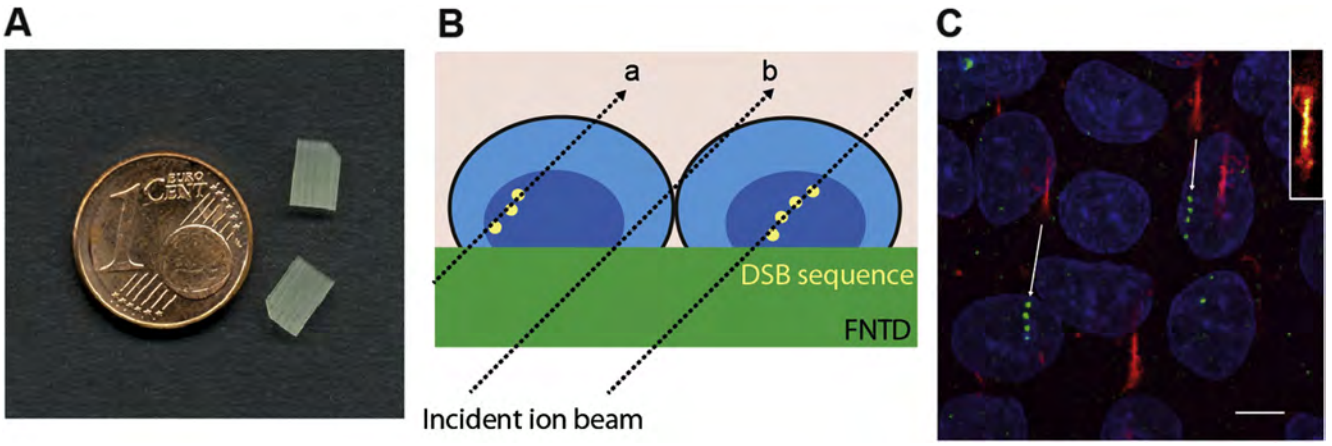

Fig. 1. Fluorescent nuclear track detector (FNTD) and cellular response to angular ion irradiation. (A) Two FNTDs ($8 \cdot 4 \cdot 0.5$ mm^3). Courtesy of M.S. Akselrod, Landauer Crystal Growth Division. (B) Double-strand breaks accumulating along the ions flight paths in the cell nucleus. False-positive (b) and false-negative (a) events are at equilibrium. (C) Example of superposition of cellular response data (maximum intensity z-projection) with an image of the acquired FNTD stack proximate to the detector surface. Track spots: red; cell nuclei (HOECHST): blue; γ-H2AX foci green. The arrows connect the radiation-induced γ-H2AX foci sequences with the recorded track spots of the corresponding ion tracks. It is only a section of the total imaging field. Inset: Track spot, masked. Scale bar = 5 μm.

Ion track reconstruction

In Figure 2 a reconstructed path for the carbon ions in the cell layer is shown. For assessment of the ion track centers, reconstruction of the particle tracks in the FNTD (\Delta z= 3 μm) , and extrapolation of the ion trajectories into the cell layer we used procedures described previously (6). Detection of intensity-weighted centroids was applied with a global threshold of 0.4 (with pixel values in the interval [0; 1]). For less intense track spots the threshold was adapted to 0.3 and 0.2. The uncertainty Δs in the position of the FNTD surface in z was assumed to be 1 μm. Small-scale scratches and digs in the polished detector surface were neglected, and the position of the surface in z was assumed to be constant. For correction of axial geometric distortion occurring during the read-out of the hybrid detector we assumed the thickness of the cell layer to be constant (6).

Ion hit statistics

In principle the number of hits per nucleus can be assessed by track extrapolation and intersection with the nucleus body. For the hit statistics (not for the correlation study) we chose a simpler approach and counted only hits where the track center at the FNTD−cell boundary falls into the maximum-intensity projection of the nucleus. We assumed all ion tracks to have the same orientation (θ_{ion}, φ_{ion}, see Results). Because the majority of tracks had the same orientation, false-positive and false-negative events were at equilibrium (Fig. 1B). The number of such hits was multiplied by A_c/A_n (with A_c, A_n: mean area of cell and of nucleus) to calculate the total number of cellular hits. All cells in the imaging field were taken into account.

To categorize the ion traversals by carbon ions and by lighter fragments, we applied the background subtractor from the Mosaic tool collection (9, 10) on the FNTD image stack (sliding window length: 80 pixels). In the image plane proximate to the detector surface (approximately 10 μm in depth) each track spot was masked with a rectangle of dimensions $\Delta x \cdot \Delta y = 20 \cdot 100$ pixel (inset, Fig. 1C). The intensity values within the rectangles were summed and converted into the count-rate (1).

Study of spatial correlation

We correlated the reconstructed ion tracks from the FNTD to radiation-induced γ-H2AX foci (RIF) sequences in the cellular compartment of the Cell-Fit-HD. We defined an RIF sequence to comprise at minimum 3 distinct γ-H2AX foci accumulating at the actual DSBs (11). Such signature allows for a robust study of high specificity and lowers the probability of coincidental correlation because not all foci necessarily account for irradiation-induced DSBs (12, 13). We also assessed the feet of the perpendicular (FOPs: intersection of the ion track with the perpendicular of the corresponding γ-H2AX foci) of an RIF sequence.

Results

Ion hit statistics

An example of the resulting superposition of cellular response data with an image of the acquired FNTD stack is shown in Figure 1C. The cells formed a tightly packed layer. We counted 515 cells over the total imaging field. The mean area per cell, Ac (nucleus, A_n) was thus 158 μm^2 (83 μm^2). The actual ion beam fluence was assessed to be $5.62 \cdot 10^5$ cm^{-2}. The mean flight direction of the traversing carbon ions was found to be $\theta_{ion} = 58.98°$ and $\varphi_{ion} = 84.69°$, respectively (6). By the intensity of the track spots, a LET surrogate (1), the ion traversals could be categorized into 2 main populations: primary carbon ions and lighter fragments, most probably protons. The fragments constitute approximately 67% of the actual fluence (Fig. 5A). Thirty percent of the fragments showed large angular scattering (ie, were deflected more than 10° away from mean φ_{ion}).

We estimated the nuclei hits to be 242 (on average 0.470 total hits per nucleus); 103 hits by carbon ions and 139 by fragments, with the following distribution: 315 nuclei not hit (322 according

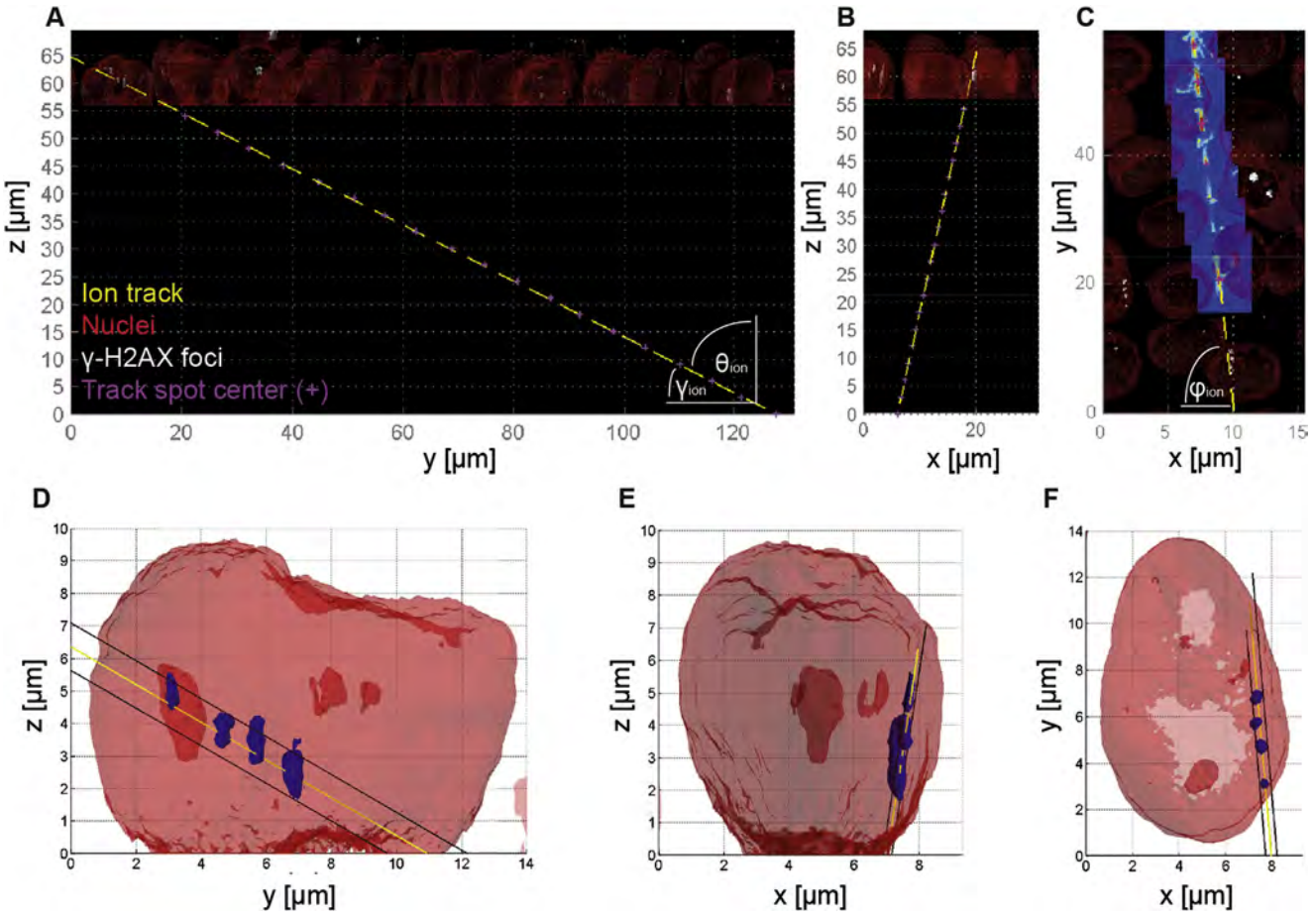

Fig. 2. Projections (yz, xz, xy) of an ion track reconstruction and extrapolation into the cell layer. (A-C) The yellow dashed line indicates the ion track (parameterized by θ_{ion}, γ_{ion}, and φ_{ion}). The magenta check marks indicate the detected track centers in the image planes of the fluorescent nuclear track detector image stack. Cell nuclei and γ-H2AX foci are depicted in red and white, respectively. (C) A section of the xy projection (including subvolumes of the detector image planes with the ellipsoidal track-spots). (D-F) Spatial correlation between ion track (yellow line), cell nucleus (red), and γ-H2AX foci (blue). The black lines indicate the 95% prediction intervals (only the upper right and the lower left boundaries are shown) (6).

to an ideal Poisson distribution), 159 nuclei once (151), 40 nuclei twice (36), and 1 nucleus 3 times (6).

In sum we identified 17 RIF sequences that could all be correlated to single ion tracks (Fig. 3) (ie, 4% of all cellular hits caused an RIF sequence). In 4 cases, 2 RIF sequences were located in the same nucleus. The probability (4 of 17) of having 2 sequences in a single nucleus coincides well with the probability (40 of 242) of 2 hits per nucleus.

Residuals and dynamics of RIF sequence

The mean residuals between the centroids of the scattered RIFs and the ion tracks in x and y were 1.09 µm ± 0.23 µm and −1.72 µm ± 0.82 µm (standard deviation [SD]; Fig. 4A). The mean slope of the reconstructed track $\gamma_{ion} = 90° - \theta_{ion} = 31.02° \pm 0.80°$ and the mean azimuth φ_{ion} (84.69° ± 1.13°) coincided with the mean slope $\gamma_{RIF} = 33.40° \pm 5.94°$ and the mean $\varphi_{RIF} = 86.46° \pm 3.71°$ of the RIF− sequences (Fig. 2D-F). Generally, we found a trend for the tracks to be located above (ie, in positive z) the RIF sequences (indicated by negative residuals in y). The mean perpendicular between the ion track and the γ-H2AX foci was 1.58 µm ± 0.69 µm (Fig. 4B).

Figure 5B shows the correlation between the intensities of detected track spots and the mean distance between two neighboring FOPs of an RIF sequence. The track-spot intensities are clustered in the interval (400; 800 MHz).

Discussion

Although we expected a high sensitivity for DSB detection (11), only 4% of the cellular hits were causing an RIF sequence (with at minimum 3 γ-H2AX foci). Possible reasons could be cell-cycle arrest with a slowed-down DNA repair dynamic (and hence lack of γ-H2AX) in the tightly packed cell layer, as well as DSBs already repaired within the time-frame before fixation.

Residuals

The mean residuals between the scattered RIFs and the ion tracks showed a systematic shift in x and y (Fig. 4). An orchestrated rotation of the cell layer in the horizontal could be excluded to cause this shift because the orientation of the RIF sequences and of the ion tracks correlates well over the entire imaging field.

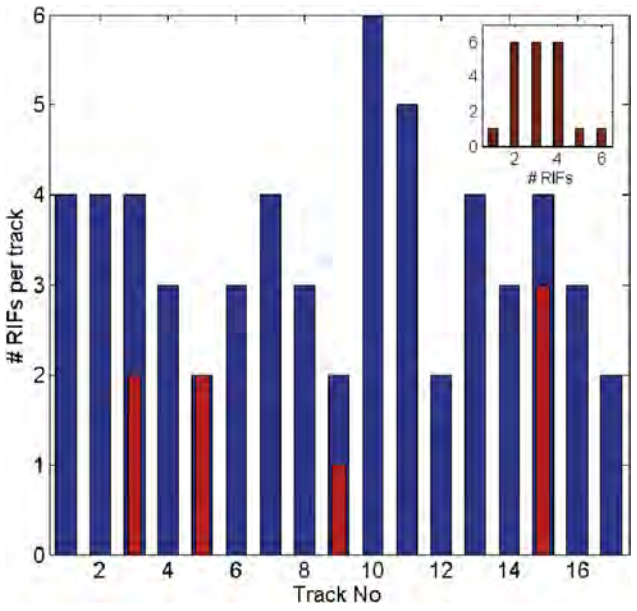

Fig. 3. Radiation-induced γ-H2AX foci (RIF) distribution. If an RIF sequence spreads over 2 cell nuclei the numbers of foci per nucleus were treated separately (combination of a red and blue bar). Inset: Number of RIFs per nucleus. In tracks 14-17 the number of foci might vary because the nuclei are partly located outside the imaging field. Partially, RIFs appeared to be fused, hampering detection of the actual number of RIFs per sequence. Although an RIF sequence comprises at least 3 γ-H2AX foci, we also took track 17 into account, where 2 foci were very close. In track 12 the RIF sequences has only 2 γ-H2AX foci. Tracks 11 and 12 are traversing the same cell nucleus. Here the total number of γ-H2AX foci were counted first (more than 3) and then assigned to the corresponding ion track.

The width of the angular distribution of the RIF sequences parameterized by the SD might be an indication for a slight rotation of individual nuclei. However, the accuracy in determining the orientation of the RIF sequences was limited by the small number of RIFs per sequence.

Migration of individual cells in the tightly packed epithelial network with strong cell−cell adhesion was very unlikely. Due to small residuals (eg, track 1; Fig. 4A) a collective translation of the entire cell cover could be excluded.

Rather, the residuals (especially in y) exhibited a spatial dependence: the largest values in the residual distribution can be explained by an apparent drift of the cell layer in the upper right quadrant (I) caused by inaccurate mechanical alignment of the microscope stage during the tile scan (Fig. 4A).

Another major contributor to the residuals most likely results from the uncertainty Δs of the exact position of the FNTD surface in z. An error $\Delta s = 1$ μm translates into a systematic error in the residuals in x and y of approximately 0.04 μm and 0.40 μm, respectively (steep θ_{ion} [6]). The systematic error in the residuals caused by limitation in the microscopy setup (eg, stage precision, lowering of the stage in z) was <1 μm.

Stress-induced rearrangements as well as DSB repair dynamics, whether by passive diffusion or directed migration of the DSBs (14, 15), could also contribute to the residual shift. In a broader context it is unclear whether the center of the γ-H2AX foci actually indicates the location of the DSB correctly and whether the vicinity of the DSB gets labeled isotropically (16).

Dynamics of RIF sequence

The narrow distributions of the mean perpendicular per ion track (Fig. 4B) emphasize a scattering of individual RIFs within a sequence on the submicrometer scale. The number of RIFs correlated to an ion track (Fig. 3) can only partly be explained by the total ion interaction path length in the nucleus. The regular rather than random spacing between neighboring FOPs and RIFs (accumulation at 1 μm and 3 μm; inset in Fig. 5B) could be attributed to chromatin organization (17-19) as well as RIF clustering (15, 20) or reflect unrevealed correlations between LET and recurring biological response patterns (Fig. 5B). According to the

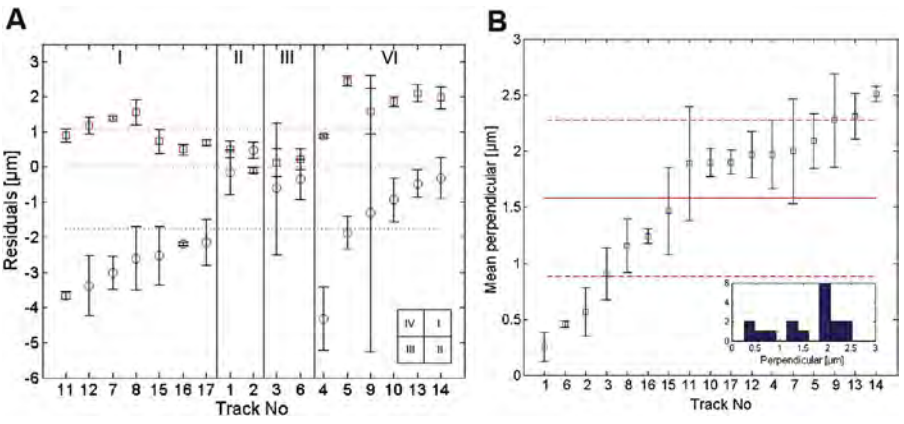

Fig. 4. Mean lateral residual and mean perpendicular between the radiation-induced γ-H2AX foci and the corresponding ion tracks. In an initial step the residuals and the perpendiculars corresponding to a single ion track were averaged. (A) The overall mean in x (solids) is 1.09 μm ± 0.23 μm (red dotted line) and in y (circles) is −1.72 μm ± 0.82 μm (blue dotted line). Inset: The residuals were sorted with respect to the quadrant of the tile scan. (B) The distribution of the mean perpendicular (blue solids) shows a sigmoidal trend. The errors show the standard deviation for each track. The overall mean is 1.58 μm (red solid line) with a standard deviation of 0.69 μm (red dashed line). Inset: Distribution of the mean perpendicular.

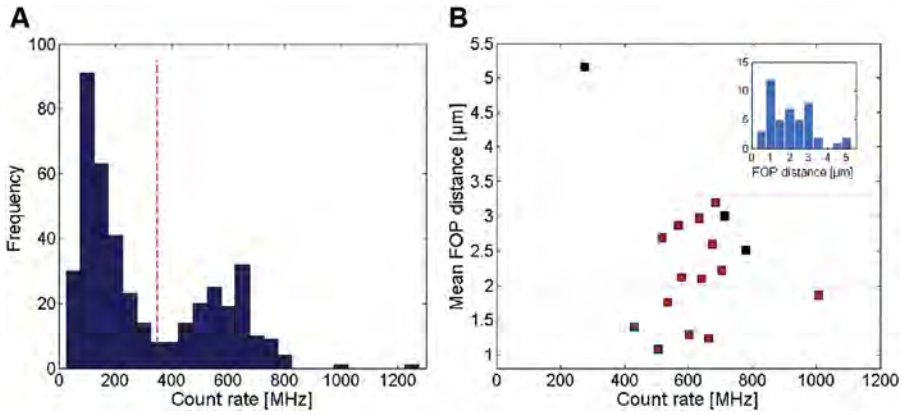

Fig. 5. Correlation between the intensities of the track spots and the mean distance between neighboring feet of the perpendicular (FOPs). (A) Distribution of the track spot intensities, a surrogate for the linear energy transfer (1). According to the histogram the threshold was set to 350 MHz (red dashed line) to distinguish between high linear energy transfer particles (mainly carbon ions) and lighter fragments. (B) The mean FOP distances corresponding to carbon ion tracks are clustered in the interval (2; 3.3 µm). The track-spot intensities represented by the black solids are in fact smaller. Two very close neighboring tracks partly intersecting hinder a clear separation by the track spot intensity analysis. The distances were calculated only between FOPs located in the same cell. Inset: The distribution of all FOP distances exhibits accumulation around 1 µm, 2 µm, and 3 µm.

distribution of the track spot intensities (Fig. 5A) the majority of RIF sequences seemed to be caused by high-LET carbon ions (Fig. 5B). The appearance of distinct RIFs emphasizes a stochastic energy deposition pattern by the traversing ion. This compares well with the appearance of blobs along single ion tracks (4), which characterizes the FNTD as a promising biological cell surrogate candidate to mimic biological response to ion irradiation.

Conclusions

The novel hybrid detector Cell-Fit-HD provides direct visualization and 3-dimensional spatial correlation of physical energy deposition (1, 2, 5, 7) and cellular response after proton and heavy ion irradiation with a diffraction-limited resolution. The nondestructive and sequential read-out by the very same CLSM without removal of the cellular compartment is a key feature of this radiobiological tool (4). The systematic shift in this spatial correlation study was shown to be smaller than the dimensions of a single cell and even of individual organelles (eg, nucleus). Perpendicular irradiation of the Cell-Fit-HD will even lower this shift and potential uncertainties (6). Cell-Fit-HD therefore allows for unambiguous spatial correlation studies of cell damage with respect to the intracellular ion traversal. The 3-dimsensional ion track reconstruction opens a novel way to consider a plethora of physical track parameters like LET and fluence in the hit−response relationship. Combined with live-cell imaging, one can reveal both temporal and spatial correlation and thus enhance our understanding of the cell-killing effect in the vicinity of particle hit and may identify other critical targets than the nucleus (21, 22). The possibility of resolving a clinical fluence and the short irradiation time for large numbers of cells (<10 seconds) enables experiments under therapeutic beam conditions. Making transition of cellular response from a microscopic to a macroscopic scale could help further adjust therapeutic ion beam parameters, elucidate its superiority for the treatment of certain tumors, and estimate the effect of normal tissue complication. These studies will be valuable in the search for a more appropriate parameter for the quantification of tumor response to ion radiation therapy than the dose absorbed.

References

1. Niklas M, Melzig C, Abdollahi A, et al. Spatial correlation between traversal and cellular response in ion radiotherapy - towards single track spectroscopy. *Radiat Meas* 2013;56:285-289.
2. Osinga JM, Akselrod MS, Herrmann R, et al. High-accuracy fluence determination in ion beams using fluorescent nuclear track detectors. *Radiat Meas* 2013;56:294-298.
3. Sykora GJ, Akselrod MS, Benton ER, et al. Spectroscopic properties of novel fluorescent nuclear track detectors for high and low let charged particles. *Radiat Meas* 2008;43:422-426.
4. Niklas M, Greilich S, Melzig C, et al. Engineering cell-fluorescent ion track hybrid detectors. *Radiat Oncol* 2013;8:141. http://dx.doi.org/10.1186/1748-717X-8-141.
5. Akselrod MS, Sykora GJ. Fluorescent nuclear track detector technology - a new way to do passive solid state dosimetry. *Radiat Meas* 2011;46:1671-1679.
6. Niklas M, Bartz JA, Akselrod MS, et al. Ion track reconstruction in 3d using fluorescent nuclear track detector. *Phys Med Biol* 2013;58:N251. http://dx.doi.org/10.1088/0031-9155/58/18/N251.
7. Greilich S, Osinga JM, Niklas M, et al. Fluorescent nuclear track detectors as a tool for ion-beam therapy research. *Radiat Meas* 2013;56:267-272.
8. Akselrod GM, Akselrod MS, Benton ER, et al. A novel Al2O3 fluorescent nuclear track detector for heavy charged particles and neutrons. *Nucl Instrum Meth B* 2006;247:295-306.
9. Helmuth JA, Burckhardt CJ, Greber UF, et al. Shape reconstruction of subcellular structures from live cell fluorescence microscopy images. *J Struct Biol* 2009;167:1-10.
10. Cardinale J. Histogram-based background subtractor for ImageJ. Technical report. Zurich: ETH Zurich MOSAIC Group; 2010.
11. Rogakou EP, Pilch DR, Orr AH, et al. DNA double-stranded breaks induce histone H2AX phosphorylation on serine 139. *J Biol Chem* 1998;273:5858-5868.
12. Ward IM, Chen J. Histone H2AX is phosphorylated in an ATR-dependent manner in response to replicational stress. *J Biol Chem* 2001;276:47759-47762.

13. Hanasoge S, Ljungman M. H2AX phosphorylation after UV irradiation is triggered by DNA repair intermediates and is mediated by the ATR kinase. *Carcinogenesis* 2007;28:2298-2304.
14. Aten JA, Stap J, Przemek M, et al. Dynamics of DNA double-strand breaks revealed by clustering of damaged chromosome domains. *Science* 2004;303:92-95.
15. Neumaier T, Swenson J, Pham C, et al. Evidence for formation of DNA repair centers and dose response nonlinearity in human cells. *Proc Natl Acad Sci U S A* 2011;109:443-448.
16. Bewersdorf J, Bennett BT, Knight KL. H2AX chromatin structures and their response to DNA damage revealed by 4Pi microscopy. *Proc Natl Acad Sci U S A* 2006;103:18137-18142.
17. Jakob B, Scholz M, Taucher-Scholz G. Biological imaging of heavy charged-particle tracks. *Radiat Res* 2003;159:676-684.
18. Karagiannis TC, Harikrishnan KN, El-Osta A. Disparity of histone deacetylase inhibition on repair of radiation-induced DNA damage on euchromatin and constitutive heterochromatin compartments. *Oncogene* 2007;26:3963-3971.
19. Cowell IG, Sunter NJ, Singh PB, et al. Gamma-h2ax foci form preferentially in euchromatin after ionising-radiation. *PLoS One* 2007;2:e1057. DOI:10.1371/journal.pone.0001057.
20. Hlatky L. Double-strand break motions shift radiation risk notions? *Proc Natl Acad Sci U S A* 2012;109:351-352.
21. Azzam EI, Jay-Gerin JP, Pain D. Ionizing radiation-induced metabolic oxidative stress and prolonged cell injury. *Cancer Lett* 2012;327:48-60.
22. Shao C, Folkard M, Michael BD, et al. Targeted cytoplasmic irradiation induces bystander responses. *Proc Natl Acad Sci U S A* 2004; 101:13495-13500.